Structures 60 (2024) 105848

Contents lists available at ScienceDirect

Structures

journal homepage: www.elsevier.com/locate/structures

# Effect of porosity on the modal response of doubly-curved laminated shell structures made of functionally graded materials employing higher order theories

Francesco Tornabene *, Matteo Viscoti, Rossana Dimitri

*Department of Innovation Engineering, School of Engineering, University of Salento, 73100 Lecce, Italy*

ARTICLE INFO

*Keywords:*
Anisotropic materials
Doubly-curved shells
Functionally graded materials
Generalized differential quadrature method
Modal analysis
Porosity

ABSTRACT

The manuscript investigates the modal response of laminated anisotropic doubly-curved shell structures of variable thickness made of Functionally Graded Materials (FGM), according to an efficient equivalent single layer strategy where the displacement field is described employing a condensed unified formulation, accounting for a higher order through-the-thickness expansion. A generalized power law distribution is adopted for the assessment of the FGM layers, whereas the presence of voids is considered starting from different homogenization assumptions. Unlike previous works which presented a variation of the homogenized material properties within the shell solid, in this paper the problem of material porosity is addressed, therefore a general distribution of the volume fraction of the constituent materials is considered, along with the presence of voids. To this end, both linear and trigonometric through-the-thickness distributions are here assumed. The fundamental governing equations are derived starting from a proper set of curvilinear principal coordinates, while a generalized set of blending functions accounts for arbitrarily shaped structures. Non-conventional boundary conditions are, here, modelled with a distribution of linear springs along the shell edges. The numerical implementation of the problem is performed with the generalized differential quadrature method. A systematic set of validating examples is presented, whose results are compared to predictions based on refined models, as well as some experimental evidence. After a validation step, an extensive parametric analysis points out the sensitivity of the porosity parameters on the modal response of structures with different curvatures and external constraints, with valid findings for engineering design purposes.

## 1. Introduction

Recent advances in most engineering applications account for the employment of smart innovative materials with optimized mechanical properties [1,2]. Furthermore, structures of complex geometry are very frequently required due to their enhanced mechanical properties and aesthetics. In this context, refined mechanical models are developed so that the structural response, both in a static and dynamic sense, can be well predicted in a simple but accurate way [3,4]. In particular, an efficient description of the geometry and material properties is a key aspect for structural problems.

The geometric assessment of structures with different curvatures in a unified way is essential for smart numerical implementations. Laminated doubly-curved shells are investigated starting from the geometric description of a reference surface located in the middle thickness of the structure [5,6]. In this way, the main geometric parameters are computed, and a parametrization in terms of curvilinear principal coordinates is employed, thus leading to the definition of a rectangular physical domain. Complex geometries can be described in a very efficient way in terms of NURBS curves, starting from a set of knots, weights and control points [7,8]. Then, the isogeometric approach [9] can be adopted for the distortion of the physical domain, such that a proper coordinate transformation comes out. In some applications, designers account for a smooth variation of the shell thickness, leading to structures of variable stiffnesses and optimized masses [10–12].

As it is well-known from literature, the three-dimensional elasticity theory for anisotropic elastic solids is one of the most refined approaches for the structural analysis of thick doubly-curved shells made of innovative materials [13–15]. On the other hand, in most applications, a significative computational effort is required, and it can be difficult to be

* Corresponding author.
*E-mail address:* francesco.tornabene@unisalento.it (F. Tornabene).

https://doi.org/10.1016/j.istruc.2023.105848
Received 25 October 2023; Received in revised form 21 December 2023; Accepted 31 December 2023

extensively applied. For this reason, two-dimensional simplified formulations have been developed in which the three-dimensional solid is reduced to an equivalent two-dimensional surface with homogenized mechanical properties [16–19]. In the case of very thick shells or structures with complex lamination schemes with softcore behaviour, the so-called Layer-Wise (LW) approach [20,21] is a valid alternative to classical Equivalent Single Layer (ESL) theories [22,23] since it accounts for the solution of the structural problem within each lamina of the stacking sequence. Generally speaking, the accuracy of two-dimensional approaches is based on the selection of the through-the-thickness kinematic assumptions. Accordingly, some formulations are present with power series expansion, whereas in other works trigonometric functions are employed. Furthermore, formulations involving generalized polynomials are employed in different works from literature [24–26]. Referring to the ESL approach, the interlaminar coupling is depicted from the employment of the zigzag functions [27,28], whereas in LW formulation this issue is directly embedded in the model by means of the interlaminar compatibility conditions [29–31]. In addition, a proper prediction of the structural response can be performed with the so-called refined zigzag theories, in which the thickness function set depends on the shear properties of the layers within structure [32–35]. A milestone in this research topic is the so-called unified formulation [36–38], in which the structural theory is developed in a general form for a specific field variable expansion order regardless the nature of the selected thickness function. Thus, a matrix assembly leads to the complete definition of the fundamental governing equations for the selected displacement field assumption. Starting from first pioneering works based on classical approaches like the Classical Plate Theory (CPT), the First Order Shear Deformation Theory (FSDT) and the Third Order Shear Deformation Theory (TSDT) [39–41], the unified formulation has been adopted for a series of structural problems employing composite materials [42], carbon nanotubes, pantographic layers [43] and honeycomb cells [44].

Furthermore, some interesting works on structures made of Functionally Graded Materials (FGMs) can be found [45]. As it is well known, FGMs belong to the class of granular composites since they are obtained from the coexistence within the same layer of two different constitutive materials, typically ceramic and metal phases [46]. In this way, an intermediate material with non-homogeneous mechanical behaviour is obtained. In most applications, plates and shell structures account for a though-the-thickness smooth variation of the mechanical properties of the constitutive materials, which is usually computed in terms of volume fractions, and the equivalent mechanical properties are derived from the Voigt's rule of mixture [47,48]. Different distributions can be found in literature with different number of governing parameters, accounting for symmetric and unsymmetric through-the-thickness dispersions. In addition, non-polynomial formulations can be also adopted. In Ref. [49] a five-parameters generalized expression has been proposed, involving a set of simplified FGM models. In any case, the governing parameters of the distribution should be selected so that the final expression has a physical significance; namely the volume fraction dispersion should always assume non-zero values and should be minor than the unit value, according to its definition. It has been demonstrated, also, that in some cases, the employment of FGM (which is an intermediate material between two isotropic constituents), can enhance the natural frequencies of the structure with respect to the isotropic conventional case.

The static and dynamic structural response of FGM structures with curvatures can be influenced by the variation of the material properties due to the presence of voids, coming from the sintering manufacturing process [50]. This manufacturing aspect leads to a reduction of the mechanical properties of the homogenized continuum medium. In Ref. [51], this aspect has been also shown from some experimental dynamic tests. As far as the computation of the equivalent elastic properties is concerned, in many structural applications the approach proposed in Refs. [52–55] is usually followed. Moving from the rule of mixture applied to dense materials, it accounts for a subtraction of a porosity parameter from the volume fractions of the constituents. On the other hand, a more general expression has been adopted in Refs. [56–60], in which the presence of porosity turns into a reduction of the material properties of the dense FGM material. In Ref. [61] a simple hierarchical model is proposed for an efficient description of complex through-the-thickness volume fractions distributions. The assumptions held on the selection of the methodology for the computation of the equivalent elastic properties of the porous material, influence the numerical results. For this reason, the most suitable approach should be accurately selected for each case, depending on the application. Referring to plates and shells, different porosity distributions have been proposed, accounting for linear and non-linear analytical expressions.

As far as the solution of the fundamental governing equations is concerned, a series of articles are provided in which the closed-form solution is adopted [62], whereas in Refs. [63] the well-known finite element method is employed. In the present contribution, the Generalized Differential Quadrature (GDQ) method and the Generalized Integral Quadrature (GIQ) are applied for the numerical implementation of the fundamental governing equations [64]. Belonging to the class of spectral collocation methods, such numerical techniques are based on an interpolation of the unknown function on a set of points lying on non-uniform grids [65,66]. In particular, the GDQ methodology accounts for the computation of the derivatives of arbitrary order as a weighted sum of the values of the function itself employing the iterative approach outlined in Ref. [67]. In this way, the differential equations of the structural problem can be numerically tackled directly in strong form, without any shape function requirement [68]. Furthermore, a reduced number of Degrees of Freedom (DOFs) is usually employed with respect to classical numerical methods. As a matter of fact, the accuracy of the method depends on the definition of the computational domain, as well as the computation of weighting coefficients. In particular, it has been shown that non-uniform symmetric grids provide the best results in terms of accuracy, computational stability and efficiency.

In the present contribution, the dynamic response of doubly-curved shell structures is investigated according to the ESL approach, employing higher order theories. A generalized distortion of the physical domain is considered, whereas an arbitrary thickness profile is modelled in the two principal directions. The present unified formulation, derived from the Hamiltonian principle employing higher order theories, can be seen as an extension of some previous papers, since for the first time here some shell structures are considered which are made of FGM isotropic layers embedded in a composite laminae with variable angle tow composites. Furthermore, in all the pervious works by the authors the effect of the material porosity in a FGM layer was not considered. Besides, the homogenized material properties of porous FGM layers are evaluated for the first time with an enhanced version of the classical Voigt's rule of mixture. In Ref. [69] we modelled a three-dimensional variation of the homogenized anisotropic material properties within the three-dimensional solid. In contrast, in this paper a general through-the-thickness variation of the volume fraction of isotropic FGM layers is considered in order to take into account the porosity of the structure. Then, various approaches are adopted to determine the homogenized material properties of the layer, leading to some considerations on the governing parameters in order to provide physically consistent results. In addition, this study considers doubly-curved shell structures made of FGM layers subjected to general boundary conditions, obtained from an arbitrary distribution of linear elastic springs distributed along the lateral surfaces of the solid, while in Ref. [49] only conventional external restraints are modelled.

The GDQ method is adopted for the numerical implementation of the problem, and the frequencies and mode shapes of structures with different curvatures and lamination schemes are derived from the present model. The results are successfully compared to those obtained from refined 3D FEM models. Furthermore, some experimental results of the mode frequencies and shapes of porous FGM 3D-printed plates have been predicted successfully with the present two-dimensional

formulation. The present higher order ESL model also matches the predictions of a previous LW formulation by the authors. Extensive parametric analyses are provided in the manuscript, showing the influence of the porosity parameters and distribution type on the dynamic response of shell structures. The proposed approach is, thus, revealed to be a very efficient formulation for a correct modelling of FGM porous doubly-curved structures, capable of providing very accurate results with a reduced computational cost. More specifically, the model can be adopted to model doubly-curved structural components that are obtained from sintering processes, as happens for instance in granular composite structures typical of mechanical engineering applications, where the manufacturing process can induce some voids with an arbitrary distribution along the thickness direction. The present model can also be applied in some civil engineering applications, including lightweight concrete structures and mortars with a variable distribution of grains within the cementitious matrix.

## 2. Theoretical formulation and fundamental equations

According to the ESL approach, the arbitrary position vector $\mathbf{R}(\alpha_1, \alpha_2, \zeta)$ of a three-dimensional doubly-curved solid should be described starting from the definition of a reference surface $\mathbf{r}(\alpha_1, \alpha_2)$ located in each point at the middle thickness of the structure. In this way, the following relation can be stated [22]:

$$\mathbf{R}(\alpha_1, \alpha_2, \zeta) = \mathbf{r}(\alpha_1, \alpha_2) + \frac{h(\alpha_1, \alpha_2)}{2} z \mathbf{n}(\alpha_1, \alpha_2) \tag{1}$$

where $z = 2\zeta/h$ denotes a dimensionless thickness coordinate orientated alongside the normal unit vector $\mathbf{n}(\alpha_1, \alpha_2)$ of the reference surface, calculated as $\mathbf{n} = (\mathbf{r}_{,1} \times \mathbf{r}_{,2})/|\mathbf{r}_{,1} \times \mathbf{r}_{,2}|$, setting $\mathbf{r}_{,i} = \partial \mathbf{r}/\partial \alpha_i$ for $i = 1, 2$. For the sake of completeness, the second order partial derivatives of the reference surface position vector are denoted by $\mathbf{r}_{,ij} = \partial^2 \mathbf{r}/(\partial \alpha_i \partial \alpha_j)$ with $i$, $j = 1, 2$. It should be stated that Eq. (1) is physically consistent when a variation interval is associated to both in-plane and out-of-plane shell coordinates, namely $\alpha_i \in [\alpha_i^0, \alpha_i^1]$ for $i = 1, 2$ and $z \in [-1, 1]$, setting $\alpha_i^0 < \alpha_i^1$ the extremes of the physical domain alongside $\alpha_i = \alpha_1, \alpha_2$. It is useful to introduce the in-plane normalized coordinates $\overline{\alpha}_i \in [0, 1]$ and $\widetilde{\alpha}_i = 1 - \overline{\alpha}_i$ for $i = 1, 2$, defined according to the following expression:

$$\overline{\alpha}_i = \frac{\alpha_i - \alpha_i^0}{\alpha_i^1 - \alpha_i^0} \tag{2}$$

The geometric main properties of the reference surface at issue can be effectively calculated from the main outcomes of differential geometry. In particular, the principal radii of curvature $R_i(\alpha_1, \alpha_2) = R_1, R_2$ and the Lamè parameters $A_i(\alpha_1, \alpha_2) = A_1, A_2$ related to the parametric lines alongside $\alpha_i = \alpha_1, \alpha_2$ are introduced in each point of the physical domain [22]:

$$\begin{aligned} R_i(\alpha_1, \alpha_2) &= -\frac{\mathbf{r}_{,i} \cdot \mathbf{r}_{,i}}{\mathbf{r}_{,ii} \cdot \mathbf{n}} \\ A_i(\alpha_1, \alpha_2) &= \sqrt{\mathbf{r}_{,i} \cdot \mathbf{r}_{,i}} \end{aligned} \tag{3}$$

for $i = 1, 2$. The effect of curvature is embedded in the model by means of the geometric scaling factors $H_i(\alpha_1, \alpha_2, \zeta) = H_1, H_2$, defined in each point of the three-dimensional solid as $H_i = 1 + \zeta/R_i$. In the present manuscript, the doubly-curved structures are intended to be obtained from the superimposition of $l$ different layers. In this perspective, the arbitrary point of the $k$-th layer, for $k = 1, ., l$, is located in the interval $[\zeta_k, \zeta_{k+1}]$, where $\zeta_k$ and $\zeta_{k+1}$ denote the intrados and extrados of the lamina, respectively. Furthermore, the corresponding width $h_k(\alpha_1, \alpha_2)$ is computed for each $(\alpha_1, \alpha_2)$ point as:

$$h(\alpha_1, \alpha_2) = \sum_{k=1}^{l} h_k(\alpha_1, \alpha_2) = \sum_{k=1}^{l} (\zeta_{k+1} - \zeta_k) \tag{4}$$

The previous relation provides an efficient implementation of the shell thickness profile. Referring to an arbitrary $k$-th layer of the stacking sequence characterized by a reference height denoted with $h_k^0$, it gives:

$$h_k(\alpha_1, \alpha_2) = h_k^0 \overline{h}(\alpha_1, \alpha_2) = h_k^0 \left( 1 + \sum_{i=1}^{4} \delta_i \phi_i(\alpha_1, \alpha_2) + \overline{\delta} \right) \tag{5}$$

The normalized thickness profile $\overline{h}(\alpha_1, \alpha_2)$ is obtained from the following analytical expressions $\phi_i(\alpha_1, \alpha_2)$, each of them combined in Eq. (5) through a scaling parameter $\delta_i$ and a uniform shift $\overline{\delta}$ [22]:

$$\begin{aligned} \phi_1(\alpha_1, \alpha_2) &= \{ \quad \overline{\alpha}_1^{p_1} \quad (\sin(\pi(n_1 \overline{\alpha}_1 + \alpha_{1m})))^{p_1}, \quad \phi_2(\alpha_1, \alpha_2) = \{ \quad \overline{\alpha}_2^{p_2} \quad (\sin(\pi(n_2 \overline{\alpha}_2 + \alpha_{2m})))^{p_2} \\ \phi_3(\alpha_1, \alpha_2) &= \{ \quad \widetilde{\alpha}_1^{p_3} \quad (\sin(\pi(n_3 \widetilde{\alpha}_1 + \alpha_{3m})))^{p_3}, \quad \phi_4(\alpha_1, \alpha_2) = \{ \quad \widetilde{\alpha}_2^{p_4} \quad (\sin(\pi(n_4 \widetilde{\alpha}_2 + \alpha_{4m})))^{p_4} \end{aligned} \tag{6}$$

The quantities $\alpha_{fm} \in [0, 1]$, $p_f \in \mathbb{R}$ and $n_f \in \mathbb{N}$ introduced in the previous relation can thus be conveniently selected according to the design needs.

Following the ESL methodology, the three-dimensional displacement field vector $\mathbf{U}^{(k)}(\alpha_1, \alpha_2, \zeta, t) = [U_1^{(k)} \; U_2^{(k)} \; U_3^{(k)}]^T$ of the $k$-th layer, expressed with respect to the principal coordinates $\alpha_1, \alpha_2, \zeta$, is now assessed by means of a higher order through-the-thickness expansion up to the $(N+1)$-th order, remembering that $\zeta \in [\zeta_k, \zeta_{k+1}]$ for $k = 1, ., l$. To this end, a generalized unified formulation is adopted, accounting for a pre-determined set of thickness functions $F^{(k\tau)\alpha_1}(\zeta) = F^{(k\tau)\alpha_1}, F^{(k\tau)\alpha_2}, F^{(k\tau)\alpha_3}$ referred to an arbitrary $\tau$-th kinematic expansion order. We recall that, for all layers, the curvilinear geometric reference system $\alpha_1, \alpha_2, \zeta$ is always located on the reference surface $\mathbf{r}(\alpha_1, \alpha_2)$. One gets:

$$\begin{aligned} \mathbf{U}^{(k)}(\alpha_1, \alpha_2, \zeta, t) = \sum_{\tau=0}^{N+1} \mathbf{F}^{(k\tau)}(\zeta) \mathbf{u}^{(\tau)}(\alpha_1, \alpha_2, t) \quad \Leftrightarrow \quad & \begin{bmatrix} U_1^{(k)} \\ U_2^{(k)} \\ U_3^{(k)} \end{bmatrix} \\ = \sum_{\tau=0}^{N+1} \begin{bmatrix} F^{(k\tau)\alpha_1} & 0 & 0 \\ 0 & F^{(k\tau)\alpha_2} & 0 \\ 0 & 0 & F^{(k\tau)\alpha_3} \end{bmatrix} & \begin{bmatrix} u_1^{(\tau)} \\ u_2^{(\tau)} \\ u_3^{(\tau)} \end{bmatrix} \end{aligned} \tag{7}$$

In the previous relation, a generalized displacement field vector $\mathbf{u}^{(\tau)}(\alpha_1, \alpha_2, t)$ has been introduced for each $\tau = 0, ., N+1$ lying on the reference surface. In this way, a comprehensive set of two-dimensional theories is embedded in the model, accounting for both polynomial and non-polynomial axiomatic assumptions. Furthermore, classical approaches like the CPT, the FSDT and TSDT theories represent some particular cases of Eq. (7). The thickness functions set is defined by means of higher order power functions. On the other hand, the well-known Murakami's function is modelled for the $(N+1)$-th kinematic expansion order in order to simulate the interlaminar zig-zag effects acting at each shell principal direction $\alpha_1, \alpha_2, \zeta$ [22]. Referring to the arbitrary $k$-th layer of the stacking sequence, one gets:

$$F^{(k\tau)\alpha_i}(\zeta)=\begin{cases}\zeta^{\tau} & \text{for } \tau=0,.,N\\ (-1)^k z_k=(-1)^k\left(\dfrac{2}{\zeta_{k+1}-\zeta_k}\zeta-\dfrac{\zeta_{k+1}+\zeta_k}{\zeta_{k+1}-\zeta_k}\right) & \text{for } \tau=N+1\end{cases} \tag{8}$$

When power functions are adopted in Eq. (7), the employed structural theory can be identified with the notation ED(Z) − *N*, where "E" stands for the ESL approach, "D" means that a displacement-based formulation is adopted, "Z" is introduced when the Murakami's zigzag function of Eq. (8) is employed at $N+1$, while $N$ is the maximum kinematic expansion order.

Let consider now the ESL-based kinematic relations for a doubly-curved shell, starting from those ones referred to the three-dimensional solid, being $\boldsymbol{\varepsilon}^{(k)}(\alpha_1,\alpha_2,\zeta,t)=[\varepsilon_1^{(k)}\ \varepsilon_2^{(k)}\ \gamma_{12}^{(k)}\ \gamma_{13}^{(k)}\ \gamma_{23}^{(k)}\ \varepsilon_3^{(k)}]^T$ the three-dimensional strain vector for the $k$-th layer. If we denote with $\mathbf{D}$ a global differential operator, it gives [22]:

$$\boldsymbol{\varepsilon}^{(k)}(\alpha_1,\alpha_2,\zeta,t)=\mathbf{D}\mathbf{U}^{(k)}=\mathbf{D}_{\zeta}\left(\sum_{i=1}^{3}\mathbf{D}_{\Omega}^{\alpha_i}\right)\mathbf{U}^{(k)} \tag{9}$$

Note that $\mathbf{D}$ has been split into $\mathbf{D}_{\Omega}^{\alpha_i}$ for $i=1,2,3$ and $\mathbf{D}_{\zeta}$ operators, accounting for the derivatives with respect to in-plane and out-of-plane coordinates $\alpha_1,\alpha_2,\zeta$ respectively:

$$\begin{aligned}\mathbf{D}_{\Omega}^{\alpha_1}&=[\overline{\mathbf{D}}_{\Omega}^{\alpha_1}\ \mathbf{0}\ \ \mathbf{0}]\\ \mathbf{D}_{\Omega}^{\alpha_2}&=[\mathbf{0}\ \ \overline{\mathbf{D}}_{\Omega}^{\alpha_2}\ \mathbf{0}]\\ \mathbf{D}_{\Omega}^{\alpha_3}&=[\mathbf{0}\ \ \mathbf{0}\ \ \overline{\mathbf{D}}_{\Omega}^{\alpha_3}]\end{aligned} \tag{10}$$

$$\mathbf{D}_{\zeta}=\begin{bmatrix}\frac{1}{H_1}&0&0&0&0&0&0&0&0\\ 0&\frac{1}{H_2}&0&0&0&0&0&0&0\\ 0&0&\frac{1}{H_1}&\frac{1}{H_2}&0&0&0&0&0\\ 0&0&0&0&\frac{1}{H_1}&0&\frac{\partial}{\partial\zeta}&0&0\\ 0&0&0&0&0&\frac{1}{H_2}&0&\frac{\partial}{\partial\zeta}&0\\ 0&0&0&0&0&0&0&0&\frac{\partial}{\partial\zeta}\end{bmatrix} \tag{11}$$

In the following, an extended version can be found of the sub-operators $\overline{\mathbf{D}}_{\Omega}^{\alpha_i}$ introduced in Eq. (10):

$$\begin{aligned}\overline{\mathbf{D}}_{\Omega}^{\alpha_1}&=\left[\frac{1}{A_1}\frac{\partial}{\partial\alpha_1}\ \ \frac{1}{A_1A_2}\frac{\partial A_2}{\partial\alpha_1}\ \ -\frac{1}{A_1A_2}\frac{\partial A_1}{\partial\alpha_2}\ \ \frac{1}{A_2}\frac{\partial}{\partial\alpha_2}\ \ -\frac{1}{R_1}\ \ 0\ \ 1\ \ 0\ \ 0\right]^T\\ \overline{\mathbf{D}}_{\Omega}^{\alpha_2}&=\left[-\frac{1}{A_1A_2}\frac{\partial A_1}{\partial\alpha_2}\ \ \frac{1}{A_2}\frac{\partial}{\partial\alpha_2}\ \ \frac{1}{A_1}\frac{\partial}{\partial\alpha_1}\ \ -\frac{1}{A_1A_2}\frac{\partial A_2}{\partial\alpha_1}\ \ 0\ \ -\frac{1}{R_2}\ \ 0\ \ 1\ \ 0\right]^T\\ \overline{\mathbf{D}}_{\Omega}^{\alpha_3}&=\left[\frac{1}{R_1}\ \ \frac{1}{R_2}\ \ 0\ \ 0\ \ \frac{1}{A_1}\frac{\partial}{\partial\alpha_1}\ \ \frac{1}{A_2}\frac{\partial}{\partial\alpha_2}\ \ 0\ \ 0\ \ 1\right]^T\end{aligned} \tag{12}$$

After some proper substitutions of Eq. (7) in the three-dimensional relation of Eq. (9), the ESL version of the kinematic relations for a doubly-curved shell structure is obtained [22]:

$$\begin{aligned}\boldsymbol{\varepsilon}^{(k)}&=\mathbf{D}_{\zeta}\left(\sum_{i=1}^{3}\mathbf{D}_{\Omega}^{\alpha_i}\right)\mathbf{U}^{(k)}=\sum_{\tau=0}^{N+1}\sum_{i=1}^{3}\mathbf{D}_{\zeta}\mathbf{D}_{\Omega}^{\alpha_i}\mathbf{F}^{(k\tau)}\mathbf{u}^{(\tau)}\\ &=\sum_{\tau=0}^{N+1}\sum_{i=1}^{3}\mathbf{Z}^{(k\tau)\alpha_i}\mathbf{D}_{\Omega}^{\alpha_i}\mathbf{u}^{(\tau)}=\sum_{\tau=0}^{N+1}\sum_{i=1}^{3}\mathbf{Z}^{(k\tau)\alpha_i}\boldsymbol{\varepsilon}^{(\tau)\alpha_i}\end{aligned} \tag{13}$$

where $\mathbf{Z}^{(k\tau)\alpha_i}=\mathbf{D}_{\zeta}F^{(k\tau)\alpha_i}$ denotes the higher order kinematic operator, while $\boldsymbol{\varepsilon}^{(\tau)\alpha_i}(\alpha_1,\alpha_2,t)=[\varepsilon_1^{(\tau)\alpha_i}\ \varepsilon_2^{(\tau)\alpha_i}\ \gamma_1^{(\tau)\alpha_i}\ \gamma_2^{(\tau)\alpha_i}\ \gamma_{13}^{(\tau)\alpha_i}\ \gamma_{23}^{(\tau)\alpha_i}\ \omega_{13}^{(\tau)\alpha_i}\ \omega_{23}^{(\tau)\alpha_i}\ \varepsilon_3^{(\tau)\alpha_i}]^T$ is the generalized strain vector referred to the $\tau$-th order of the kinematic expansion, with index $i=1,2,3$:

$$\boldsymbol{\varepsilon}^{(\tau)\ \alpha_i}=\mathbf{D}_{\Omega}^{\alpha_i}\mathbf{u}^{(\tau)} \tag{14}$$

The present formulation is developed for laminated structures made of generally anisotropic materials. Referring to a $k$-th layer of the laminate with $k=1,.,l$, the following constitutive relationship is considered, according to the conventions adopted in [22]:

$$\boldsymbol{\sigma}^{(k)}=\overline{\mathbf{E}}^{(k)}\boldsymbol{\varepsilon}^{(k)}=\mathbf{T}^{(k)}\mathbf{E}^{(k)}\left(\mathbf{T}^{(k)}\right)^T\boldsymbol{\varepsilon}^{(k)} \tag{15}$$

In the previous relation, $\boldsymbol{\varepsilon}^{(k)}$ denotes the strain vector already introduced in Eq. (9), whereas $\boldsymbol{\sigma}^{(k)}=[\sigma_1^{(k)}\ \sigma_2^{(k)}\ \tau_{12}^{(k)}\ \tau_{13}^{(k)}\ \tau_{23}^{(k)}\ \sigma_3^{(k)}]^T$ is the three-dimensional stress vector referred to the geometric reference system of the shell $O'\alpha_1\alpha_2\zeta$, according to Eq. (1). In this way, the three-dimensional linear elastic stiffness matrix $\overline{\mathbf{E}}^{(k)}$ is referred to $O'\alpha_1\alpha_2\zeta$, and its arbitrary component $\overline{E}_{ij}^{(k)}$ for $i,j=1,.,6$ relates the $i$-th element of $\boldsymbol{\sigma}^{(k)}$ to the $j$-th components of $\boldsymbol{\varepsilon}^{(k)}$. Accordingly, we account for a rotation with respect to the outward normal direction of the shell of an arbitrary angle $\vartheta^{(k)}$, embedded in the transformation matrix $\mathbf{T}^{(k)}=\mathbf{T}^{(k)}(\vartheta^{(k)})$. More details are reported in Ref. [22]. As a matter of fact, the input for the $k$-th layer consists in the three-dimensional elastic constitutive relationship written in the material reference system, whose elements $E_{ij}^{(k)}$ with $i,j=1,.,6$ can be taken equal to the three-dimensional elastic coefficients $C_{ij}^{(k)}$ or the reduced elastic coefficients $Q_{ij}^{(k)}$. Regarding the material orientation angle $\vartheta^{(k)}$ implicitly employed in Eq. (15), in common composite

**Table 1**
Through-the-thickness smooth distributions of the material porosity of FGM layers. Both algebraic and trigonometric functions can be arbitrarily selected depending on the desired application. Furthermore, both symmetric and unsymmetric profiles have been considered.

| **Through-the-thickness distribution of porosity** | | |
|---|---|---|
| Denomination | Symbol | Analytical Expression |
| Linear Distributions | | |
| Uniform | $U^{\beta_0}$ | $\beta^{(k)}(\xi_k)=\beta_0^{(k)}$ |
| Linear I | $L-I^{\beta_0}$ | $\beta^{(k)}(\xi_k)=\beta_0^{(k)}(1-2\lvert\xi_k\rvert)$ |
| Linear II | $L-II^{\beta_0}$ | $\beta^{(k)}(\xi_k)=2\beta_0^{(k)}\lvert\xi_k\rvert$ |
| Linear III | $L-III^{\beta_0}$ | $\beta^{(k)}(\xi_k)=\dfrac{\beta_0^{(k)}}{2}(1+2\xi_k)$ |
| Linear IV | $L-IV^{\beta_0}$ | $\beta^{(k)}(\xi_k)=\dfrac{\beta_0^{(k)}}{2}(1-2\xi_k)$ |
| Cosine Distributions | | |
| Symmetric Cosine I | $SC-I^{\beta_0}$ | $\beta^{(k)}(\xi_k)=\beta_0^{(k)}(1-\cos(\pi\xi_k))$ |
| Symmetric Cosine II | $SC-II^{\beta_0}$ | $\beta^{(k)}(\xi_k)=\beta_0^{(k)}\cos(\pi\xi_k)$ |
| Unsymmetric Cosine I | $UC-I^{\beta_0}$ | $\beta^{(k)}(\xi_k)=\beta_0^{(k)}\left(1-\cos\left(\frac{\pi}{2}\xi_k+\frac{\pi}{4}\right)\right)$ |
| Unsymmetric Cosine II | $UC-II^{\beta_0}$ | $\beta^{(k)}(\xi_k)=\beta_0^{(k)}\cos\left(\frac{\pi}{2}\xi_k+\frac{\pi}{4}\right)$ |
| Unsymmetric Cosine III | $UC-III^{\beta_0}$ | $\beta^{(k)}(\xi_k)=\beta_0^{(k)}\left(1-\cos\left(\frac{\pi}{2}\xi_k-\frac{\pi}{4}\right)\right)$ |
| Unsymmetric Cosine IV | $UC-IV^{\beta_0}$ | $\beta^{(k)}(\xi_k)=\beta_0^{(k)}\cos\left(\frac{\pi}{2}\xi_k-\frac{\pi}{4}\right)$ |
| Hyperbolic Sine Distributions | | |
| Hyperbolic Sine I | $HS-I^{\beta_0}$ | $\beta^{(k)}(\xi_k)=\beta_0^{(k)}\left(1-\left\lvert\frac{\sinh\xi_k}{\sinh\left(\frac{1}{2}\right)}\right\rvert^3\right)$ |
| Hyperbolic Sine II | $HS-II^{\beta_0}$ | $\beta^{(k)}(\xi_k)=\beta_0^{(k)}\left\lvert\frac{\sinh\xi_k}{\sinh\left(\frac{1}{2}\right)}\right\rvert^3$ |
| Hyperbolic Tangent Distributions | | |
| Hyperbolic Tangent I | $HT-I^{\beta_0}$ | $\beta^{(k)}(\xi_k)=\beta_0^{(k)}\left(1-\left\lvert\frac{\tanh\xi_k}{\tanh\left(\frac{1}{2}\right)}\right\rvert^3\right)$ |
| Hyperbolic Tangent II | $HT-II^{\beta_0}$ | $\beta^{(k)}(\xi_k)=\beta_0^{(k)}\left\lvert\frac{\tanh\xi_k}{\tanh\left(\frac{1}{2}\right)}\right\rvert^3$ |
| $\beta^{(k)}(\zeta)=\beta^{(k)}(\xi_k)$ | $\xi_k=\frac{z_k}{2}$ | $z_k=\frac{2}{\zeta_{k+1}-\zeta_k}\zeta-\frac{\zeta_{k+1}+\zeta_k}{\zeta_{k+1}-\zeta_k}$ |

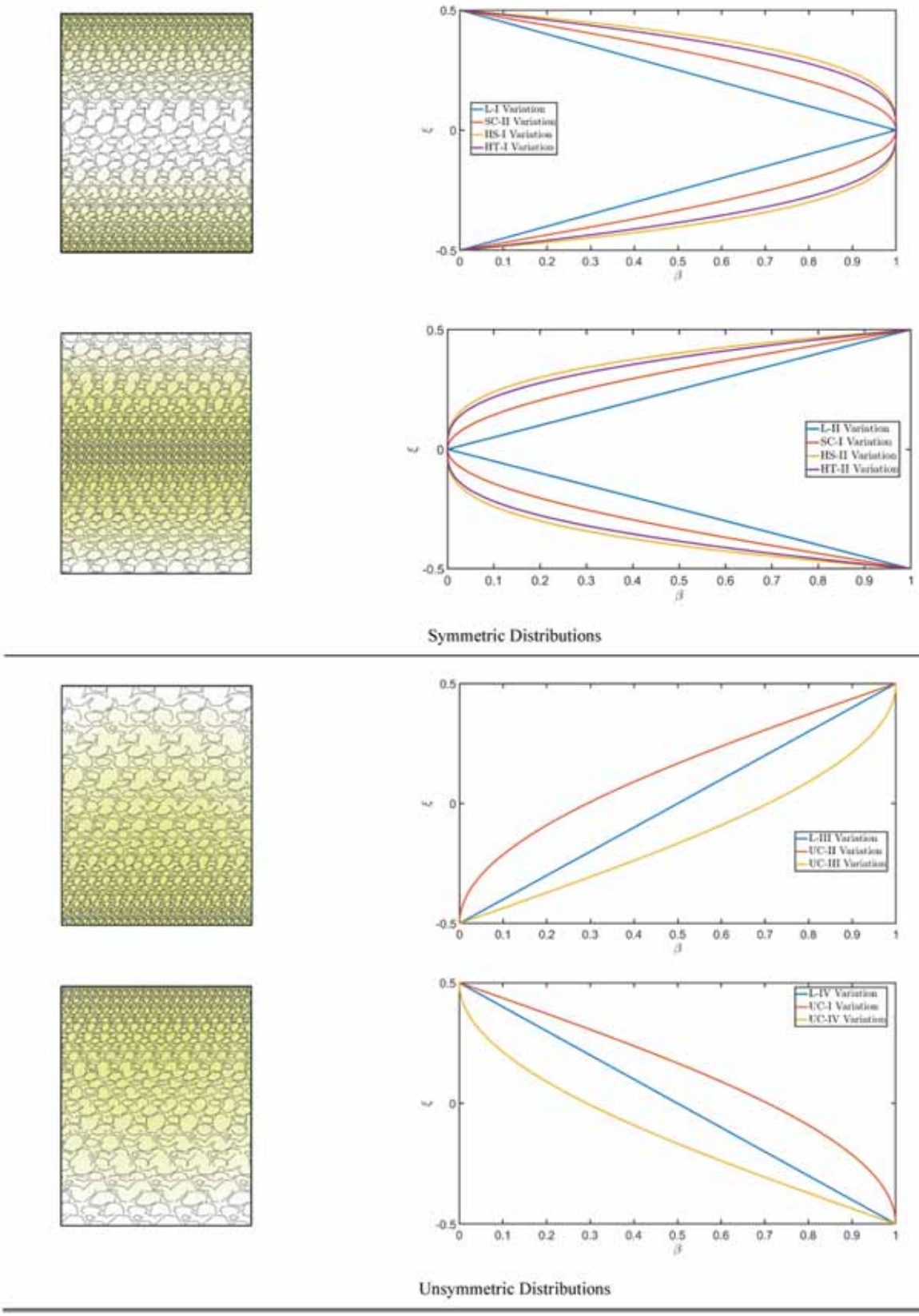


**Fig. 1.** Through-the-thickness distributions of porosity employed within each layer of doubly-curved laminated structures. Both linear and non-linear analytical expressions have been considered, accounting for the concentration of porosity in the central part of the lamina or in its intrados and extrados. Furthermore, symmetric and unsymmetric porosity dispersions have been modelled.

applications a uniform value is usually assigned to each $k$-th layer. On the other hand, a continuous variation of the material angle can be introduced, whose governing parameters are the power exponents $p_1^{(k)}$, $p_2^{(k)} \in \mathbb{R}$ and the coefficients $c_1^{(k)}, c_2^{(k)} = 0, 1$ which activate the dependence of the expression on the principal coordinates $\alpha_1$ and $\alpha_2$:

$$\begin{aligned}\vartheta^{(k)}(\alpha_1,\alpha_2) =& c_1^{(k)}\left(\left(\vartheta_1^{(k)\alpha_1}-\vartheta_0^{(k)\alpha_1}\right)|2\overline{\alpha}_1-1|^{p_1^{(k)}}+\vartheta_0^{(k)\alpha_1}\right)\\ &+c_2^{(k)}\left(\left(\vartheta_1^{(k)\alpha_2}-\vartheta_0^{(k)\alpha_2}\right)|2\overline{\alpha}_2-1|^{p_2^{(k)}}+\vartheta_0^{(k)\alpha_2}\right)+\overline{\vartheta}^{(k)}\end{aligned} \tag{16}$$

In the previous relation, the values $\vartheta_0^{(k)\alpha_1}, \vartheta_0^{(k)\alpha_2}$ are associated to the central point of the physical domain, while $\vartheta_1^{(k)\alpha_1}, \vartheta_1^{(k)\alpha_2}$ are related to the edges of the structure characterized by constant values of $\alpha_1$ and $\alpha_2$, respectively. In this context, the notation $\overline{\vartheta}^{(k)}\langle(\vartheta_0^{(k)\alpha_1}|\vartheta_1^{(k)\alpha_1})_{\alpha_1}^{p_1^{(k)}}, (\vartheta_0^{(k)\alpha_2}|\vartheta_1^{(k)\alpha_2})_{\alpha_2}^{p_2^{(k)}}\rangle$ is adopted if $c_1^{(k)} = c_2^{(k)} = 1$, whereas the condensed notation $\overline{\vartheta}^{(k)}\langle(\vartheta_0^{(k)\alpha_i}|\vartheta_1^{(k)\alpha_i})_{\alpha_i}^{p_i^{(k)}}\rangle$ for $i = 1, 2$ is adopted when $c_1^{(k)} = 0$ or $c_2^{(k)} = 0$.

An arbitrary $k$-th layer of the stacking sequence made of FGM material, which consists in a continuous smooth variation of the material properties along the thickness direction $\zeta$, is here obtained from a Ceramic (C) and a Metal (M) phase coexisting in the same lamina. Such heterogeneity can be modelled in terms of their volume fractions, denoted by $V_C^{(k)}$ and $V_M^{(k)}$, respectively. Furthermore, the quantity $\beta^{(k)}$ is introduced which accounts for the FGM porosity. These quantities are related to each other as follows:

$$V_C^{(k)}(\zeta) + V_M^{(k)}(\zeta) + \beta^{(k)}(\zeta) = 1 \tag{17}$$

As a particular case, the relation $V_C^{(k)}(\zeta) + V_M^{(k)}(\zeta) = 1$ is considered in the case of dense layers. In this way, the notation $\mathrm{FGM}_{bottom\ (a^{(k)}/b^{(k)}/c^{(k)}/d^{(k)}/p^{(k)})}^{top\ (\mathrm{A}\ /\ \mathrm{D}\ /\ \beta_0^{(k)})}$ is adopted for the identification of FGM layers, setting $a^{(k)}, b^{(k)}, c^{(k)}, d^{(k)}, p^{(k)}$ the governing parameters of the through-the-thickness distribution, while A = A1, A2, A3 denotes the approach employed for the porosity modelling, characterized by the distribution identified with the symbol D, according to the nomenclature reported in Table 1.

The Voigt's rule of mixture is thus adopted to determine the effective material properties of the $k$-th lamina of the structure, namely the density $\overline{\rho}^{(k)}(\zeta)$, the elastic modulus $\overline{E}^{(k)}(\zeta)$ and the Poisson's coefficient $\overline{\nu}^{(k)}(\zeta)$. For the sake of simplicity, the condensed symbol $\overline{P}^{(k)}(\zeta) = \overline{\rho}^{(k)}, \overline{E}^{(k)}, \overline{\nu}^{(k)}$ is used:

$$\overline{P}^{(k)}(\zeta) = P_C^{(k)} V_C^{(k)}(\zeta) + P_M^{(k)} V_M(\zeta) \tag{18}$$

being $P_C^{(k)} = \rho_C^{(k)}, E_C^{(k)}, \nu_C^{(k)}$ and $P_M^{(k)} = \rho_M^{(k)}, E_M^{(k)}, \nu_M^{(k)}$ the corresponding property of the ceramic and metal constituent of the FGM layer, respectively. In the case of a porous medium, three different approaches are considered:

$$\begin{aligned}&\text{Approach1(A1)} \rightarrow P^{(k)}(\zeta) = \overline{P}^{(k)}(\zeta)\left(1-\beta^{(k)}(\zeta)\right)\\ &\text{Approach2(A2)} \rightarrow P^{(k)}(\zeta) = \overline{P}^{(k)}(\zeta) - \frac{P_M^{(k)}+P_C^{(k)}}{2}\beta^{(k)}(\zeta)\\ &\text{Approach3(A3)} \rightarrow P^{(k)}(\zeta) = \overline{P}^{(k)}(\zeta) - \min\left(P_M^{(k)}, P_C^{(k)}\right)\beta^{(k)}(\zeta)\end{aligned} \tag{19}$$

The Approach 1 (A1) is based on Eq. (18) for the case of dense materials, and considers a reduction of the FGM homogenized material coming from the presence of porosity. Following Approach 2 (A2), the porosity parameter $\beta^{(k)}(\zeta)$ is equally distributed between the ceramic and the metal phase of the FGM layer. On the other hand, the general relation for porous FGMs reported in Eq. (17) leads to the Approach 3 (A3) for the computation of the homogenized properties of the $k$-th layer. All relations reported in Eq. (19) converge to the same distribution in the case of porous homogeneous material. On the other hand, the A2 methodology can be adopted only if the FGM and porosity parameters provide positive values for the equivalent elastic modulus and density.

In the present work, various through-the-thickness expressions have been provided for the porosity parameter $\beta^{(k)}(\zeta)$, accounting for both symmetric and unsymmetric distributions (Fig. 1). Referring to symmetric dispersions, some expressions provide a porosity concentration at the core level of the $k$-th layer, whereas others consider a densification of voids at the external sides of the layer. Furthermore, unsymmetric distributions concentrate the porosity at the external and internal sides of the lamina. For each case, a scaling parameter $\beta_0^{(k)}$ is required, defining the maximum porosity value along the thickness of the considered layer. In Table 1, the expressions employed in this context have been reported, accounting for linear, trigonometric and hyperbolic functions. They have been expressed in terms of dimensionless coordinate $\xi_k = z_k/2$, defined from the through-the-thickness quantity $z_k$ already introduced in Eq. (8).

The three-dimensional constitutive relationship of Eq. (15) is now embedded in the higher order ESL model taking into account the kinematic relations of Eq. (13) expressed in terms of generalized strain resultants vector $\boldsymbol{\varepsilon}^{(\tau)\alpha_i}$. The following condensed relation is obtained for each $k = 1,.,l$:

$$\boldsymbol{\sigma}^{(k)} = \overline{\mathbf{E}}^{(k)}\boldsymbol{\varepsilon}^{(k)} = \sum_{\eta=0}^{N+1}\sum_{j=1}^{3}\overline{\mathbf{E}}^{(k)}\mathbf{Z}^{(k\eta)\alpha_j}\boldsymbol{\varepsilon}^{(\eta)\alpha_j} \tag{20}$$

The computation of the virtual variation $\delta\Phi$ of the elastic strain energy allows the definition of the generalized stress resultants vector $\mathbf{S}^{(\tau)\alpha_i} = [N_1^{(\tau)\alpha_i}\ N_2^{(\tau)\alpha_i}\ N_{12}^{(\tau)\alpha_i}\ N_{21}^{(\tau)\alpha_i}\ T_1^{(\tau)\alpha_i}\ T_2^{(\tau)\alpha_i}\ P_1^{(\tau)\alpha_i}\ P_2^{(\tau)\alpha_i}\ S_3^{(\tau)\alpha_i}]^T$ for each $\tau$-th order of the kinematic expansion, accounting for the entire lamination scheme, as well as the axiomatic through-the-thickness assumptions for the higher order model in Eq. (7). A higher order ESL constitutive relationship is assessed in terms of $\mathbf{S}^{(\tau)\alpha_i}$ and $\boldsymbol{\varepsilon}^{(\tau)\alpha_i}$, and the generalized matrix $\mathbf{A}^{(\tau\eta)\alpha_i\alpha_j}$ is introduced for each $\tau, \eta = 0, .N+1$ and $i,j = 1,2,3$:

$$\mathbf{S}^{(\tau)\alpha_i} = \sum_{\eta=0}^{N+1}\sum_{j=1}^{3}\mathbf{A}^{(\tau\eta)\alpha_i\alpha_j}\boldsymbol{\varepsilon}^{(\eta)\alpha_j} \tag{21}$$

The generalized constitutive operator is computed for each $\tau, \eta$-th kinematic expansion order according to the following expression:

$$\mathbf{A}^{(\tau\eta)\alpha_i\alpha_j} = \sum_{k=1}^{l}\int_{\zeta_k}^{\zeta_{k+1}}\left(\mathbf{Z}^{(k\tau)\alpha_i}\right)^T\overline{\mathbf{E}}^{(k)}\mathbf{Z}^{(k\eta)\alpha_j}H_1H_2d\zeta \tag{22}$$

where the arbitrary terms of this matrix are computed as:

$$A_{nm\ (pq)}^{(\tau\eta)[fg]\alpha_i\alpha_j} = \sum_{k=1}^{l}\int_{\zeta_k}^{\zeta_{k+1}}\overline{B}_{nm}^{(k)}\frac{\partial^f F^{(k\eta)\alpha_j}}{\partial\zeta^f}\frac{\partial^g F^{(k\tau)\alpha_i}}{\partial\zeta^g}\frac{H_1H_2}{H_1^pH_2^q}d\zeta \quad \begin{array}{l}\tau,\eta=0,.,N+1,\\ n,m=1,.,6,\\ \text{for } p,q=0,1,2,\\ \alpha_i,\alpha_j=\alpha_1,\alpha_2,\alpha_3,\\ f,g=0,1\end{array} \tag{23}$$

being $\partial^0 F^{(k\tau)\alpha_i}/\partial\zeta^0 = F^{(k\tau)\alpha_i}$ and $\partial^0 F^{(k\eta)\alpha_j}/\partial\zeta^0 = F^{(k\eta)\alpha_j}$. The quantities $\overline{B}_{nm}^{(k)}$ are equal to the three-dimensional elastic constants of Eq. (15) for $n,m = 1,2,3,6$, while for $n,m = 4,5$ they are multiplied by means of the so-called shear correction factor $\kappa(\zeta) = 5/6$ in the case of a linear

distribution of in-plane displacement field components, namely $\overline{B}^{(k)}_{nm} = \kappa \overline{E}^{(k)}_{nm}$.

Once the constitutive model for doubly-curved shells is introduced within the higher order ESL theory, we consider a general set of linear elastic springs distributed alongside the four edges of the structure for both in-plane and out-of-plane directions. In particular, the boundary stresses $\overline{\sigma}^{(k)}_1, \overline{\tau}^{(k)}_{12}, \overline{\tau}^{(k)}_{13}$ are enforced at the physical domain edges located at $\alpha_1 = \alpha^m_1$, with $m = 0, 1$ by means of a set of linear elastic springs of stiffnesses $k^{(k)\alpha^m_1}_{1f}, k^{(k)\alpha^m_1}_{2f}, k^{(k)\alpha^m_1}_{3f}$:

$$\begin{aligned}
\overline{\sigma}^{(k)}_1(\alpha^m_1, \alpha_2, \zeta, t) &= -k^{(k)\alpha^m_1}_{1f}\widehat{\beta}(\alpha^m_1, \alpha_2)U^{(k)}_1(\alpha^m_1, \alpha_2, \zeta, t) \\
\overline{\tau}^{(k)}_{12}(\alpha^m_1, \alpha_2, \zeta, t) &= -k^{(k)\alpha^m_1}_{2f}\widehat{\beta}(\alpha^m_1, \alpha_2)U^{(k)}_2(\alpha^m_1, \alpha_2, \zeta, t) \quad \text{for } m = 0, 1 \\
\overline{\tau}^{(k)}_{13}(\alpha^m_1, \alpha_2, \zeta, t) &= -k^{(k)\alpha^m_1}_{3f}\widehat{\beta}(\alpha^m_1, \alpha_2)U^{(k)}_3(\alpha^m_1, \alpha_2, \zeta, t)
\end{aligned} \tag{24}$$

In the same way, the stresses $\overline{\tau}^{(k)}_{12}, \overline{\sigma}^{(k)}_2, \overline{\tau}^{(k)}_{23}$ are enforced at $\alpha_2 = \alpha^m_2$ for $m = 0, 1$:

$$\begin{aligned}
\overline{\tau}^{(k)}_{12}(\alpha_1, \alpha^m_2, \zeta, t) &= -k^{(k)\alpha^m_2}_{1f}\widehat{\beta}(\alpha_1, \alpha^m_2)U^{(k)}_1(\alpha_1, \alpha^m_2, \zeta, t) \\
\overline{\sigma}^{(k)}_2(\alpha_1, \alpha^m_2, \zeta, t) &= -k^{(k)\alpha^m_2}_{2f}\widehat{\beta}(\alpha_1, \alpha^m_2)U^{(k)}_2(\alpha_1, \alpha^m_2, \zeta, t) \quad \text{for } m = 0, 1 \\
\overline{\tau}^{(k)}_{23}(\alpha_1, \alpha^m_2, \zeta, t) &= -k^{(k)\alpha^m_2}_{3f}\widehat{\beta}(\alpha_1, \alpha^m_2)U^{(k)}_3(\alpha_1, \alpha^m_2, \zeta, t)
\end{aligned} \tag{25}$$

where $k^{(k)\alpha^m_2}_{1f}, k^{(k)\alpha^m_2}_{2f}, k^{(k)\alpha^m_2}_{3f}$ are the stiffnesses of the linear elastic springs at issue. Furthermore, in Eqs. (24)-(25) the terms $\widehat{\beta}(\alpha^m_1, \alpha_2)$ and $\widehat{\beta}(\alpha_1, \alpha^m_2)$ account for the in-plane component of the linear springs distribution along the edge of the structure. Such dispersion is conveniently assessed taking into account the relations $\widehat{\beta}(\alpha^m_1, \alpha_2) = \widehat{\beta}_m(\alpha_2)$ and $\widehat{\beta}(\alpha_1, \alpha^m_2) = \widehat{\beta}_m(\alpha_1)$. Such distributions are provided in terms of dimensionless coordinate $\overline{\alpha}_i$, for $i = 1, 2$, already introduced in Eq. (2) employing the combination $\widehat{\beta}_m(\alpha_i) = \widehat{\beta}_m((\alpha^1_i - \alpha^0_i)\overline{\alpha}_i) = \widehat{\beta}_m(\overline{\alpha}_i)$, being $\alpha^0_i, \alpha^1_i$ with $i = 1, 2$, the extremes of the physical domain in the curvilinear principal reference system. A uniform in-plane distribution of linear springs is obtained setting $\widehat{\beta}_m(\overline{\alpha}_i) = 1$. The Super Elliptic (S) distribution is expressed according to the following relation, being $\widetilde{\xi}_m, \widetilde{\xi}_m \in [0, 1]$ the governing parameters and $p$ a power exponent:

$$\widehat{\beta}_m(\overline{\alpha}_i) = e^{-\left|\frac{\overline{\alpha}_i - \widetilde{\xi}_m}{\widetilde{\xi}_m}\right|^p} \tag{26}$$

On the other hand, the Double Weibull (D) distribution reads as:

$$\widehat{\beta}_m(\overline{\alpha}_i) = 1 - \left(e^{-\left(\frac{\overline{\alpha}_i}{\widetilde{\xi}_m}\right)^p} + e^{-\left(\frac{\overline{\alpha}_i}{\widetilde{\xi}_m}\right)^p}\right) \tag{27}$$

The contribution of the above discussed linear springs can be embedded in the present higher order ESL model substituting the generalized displacement field assumption of Eq. (7) in Eqs. (24)-(25). In this way, a set of generalized stress resultants is obtained for each shell edge. In particular, the quantities $\overline{N}^{(\tau)\alpha_1}_1, \overline{N}^{(\tau)\alpha_2}_{12}, \overline{T}^{(\tau)\alpha_3}_1$ should be computed at $\alpha_1 = \alpha^m_1$ with $m = 0, 1$, for each $\tau = 0, ., N+1$:

$$\begin{bmatrix} \overline{N}^{(\tau)\alpha_1}_1 \\ \overline{N}^{(\tau)\alpha_2}_{12} \\ \overline{T}^{(\tau)\alpha_3}_1 \end{bmatrix} = -\sum_{\eta=0}^{N+1} \begin{bmatrix} L^{(\tau\eta)\alpha_1}_{f1(2)\alpha^m_1} & 0 & 0 \\ 0 & L^{(\tau\eta)\alpha_2}_{f2(2)\alpha^m_1} & 0 \\ 0 & 0 & L^{(\tau\eta)\alpha_3}_{f3(2)\alpha^m_1} \end{bmatrix} \begin{bmatrix} u^{(\eta)}_1 \\ u^{(\eta)}_2 \\ u^{(\eta)}_3 \end{bmatrix} \quad \text{for } m = 0, 1 \tag{28}$$

In the same way, the generalized stress resultants $\overline{N}^{(\tau)\alpha_1}_{21}, \overline{N}^{(\tau)\alpha_2}_2, \overline{T}^{(\tau)\alpha_3}_2$ with $\tau = 0, ., N+1$ are enforced at $\alpha_2 = \alpha^m_2$ according to the following expression:

$$\begin{bmatrix} \overline{N}^{(\tau)\alpha_1}_{21} \\ \overline{N}^{(\tau)\alpha_2}_2 \\ \overline{T}^{(\tau)\alpha_3}_2 \end{bmatrix} = -\sum_{\eta=0}^{N+1} \begin{bmatrix} L^{(\tau\eta)\alpha_1}_{f1(1)\alpha^m_2} & 0 & 0 \\ 0 & L^{(\tau\eta)\alpha_2}_{f2(1)\alpha^m_2} & 0 \\ 0 & 0 & L^{(\tau\eta)\alpha_3}_{f3(1)\alpha^m_2} \end{bmatrix} \begin{bmatrix} u^{(\eta)}_1 \\ u^{(\eta)}_2 \\ u^{(\eta)}_3 \end{bmatrix} \quad \text{for } m = 0, 1 \tag{29}$$

In Eqs. (28)-(29), the generalized stress resultants are related to the higher order displacement field vector from the quantities $L^{(\tau\eta)\alpha_i}_{fi(p)\alpha^m_n}$, with $m = 0, 1$, $n, p = 1, 2$ and $i = 1, 2, 3$:

$$L^{(\tau\eta)\alpha_i}_{fi(p)\alpha^m_n} = \sum_{k=1}^{l} \int_{\zeta_k}^{\zeta_{k+1}} k^{(k)\alpha^m_n}_{if}\widehat{\beta}\,\overline{\lambda}F^{(k\eta)\alpha_i}F^{(k\tau)\alpha_i}H_p d\zeta \quad \text{for} \quad \begin{matrix} i = 1, 2, 3, \\ m = 0, 1, \\ n, p = 1, 2 \end{matrix} \tag{30}$$

The previous relation embeds in itself the out-of-plane distribution of the linear elastic springs at issue by means of the term $\overline{\lambda} = \overline{\lambda}(\zeta)$. As a consequence, a constant ($\overline{\lambda} = 1$), linear ($\overline{\lambda} = 2\zeta/h$) and parabolic ($\overline{\lambda} = 1 - (2\zeta/h)^2$) springs profile can be easily modelled.

We now derive the fundamental relations for laminated doubly-curved shell structures, accounting for the generally anisotropic elastic constitutive behavior outlined in Eq. (15) and a unified formulation for the through-the-thickness axiomatic assumption of the displacement field variable, as stated in Eq. (7). A procedure based on the Hamiltonian Principle is followed, accounting for the kinetic energy, the elastic strain energy and the contribution coming from the action of linear elastic springs distributed along the edges of the physical domain. The equilibrium relations are easily obtained for each $\tau$-th kinematic expansion order, setting $\ddot{\mathbf{u}}^{(\eta)} = [\ddot{u}^{(\eta)}_1 \;\; \ddot{u}^{(\eta)}_2 \;\; \ddot{u}^{(\eta)}_3]^T$, with $\ddot{u}^{(\eta)}_i = \partial^2 u^{(\eta)}_i / \partial t^2$ for $i = 1, 2, 3$ the second order time derivative of the generalized displacement field vector introduced in Eq. (7):

$$\sum_{i=1}^{3} \mathbf{D}^{*\alpha_i}_{\Omega}\mathbf{S}^{(\tau)\alpha_i} - \sum_{\eta=0}^{N+1} \mathbf{M}^{(\tau\eta)}\ddot{\mathbf{u}}^{(\eta)} = \mathbf{0} \quad \text{for} \tau = 0, ., N+1 \tag{31}$$

where $\mathbf{D}^{*\alpha_i}_{\Omega} = \mathbf{D}^{*\alpha_1}_{\Omega}, \mathbf{D}^{*\alpha_2}_{\Omega}, \mathbf{D}^{*\alpha_3}_{\Omega}$ are the equilibrium operators, which are reported in compact matrix notation as:

$$\mathbf{D}^{*\alpha_1}_{\Omega} = \begin{bmatrix} \overline{\mathbf{D}}^{*\alpha_1}_{\Omega} \\ \mathbf{0} \\ \mathbf{0} \end{bmatrix}, \quad \mathbf{D}^{*\alpha_2}_{\Omega} = \begin{bmatrix} \mathbf{0} \\ \overline{\mathbf{D}}^{*\alpha_2}_{\Omega} \\ \mathbf{0} \end{bmatrix}, \quad \mathbf{D}^{*\alpha_3}_{\Omega} = \begin{bmatrix} \mathbf{0} \\ \mathbf{0} \\ \overline{\mathbf{D}}^{*\alpha_3}_{\Omega} \end{bmatrix} \tag{32}$$

The definition of quantities $\overline{\mathbf{D}}^{*\alpha_i}_{\Omega} = \overline{\mathbf{D}}^{*\alpha_1}_{\Omega}, \overline{\mathbf{D}}^{*\alpha_2}_{\Omega}, \overline{\mathbf{D}}^{*\alpha_3}_{\Omega}$ introduced in the previous equation reads as:

$$\begin{aligned}
\overline{\mathbf{D}}^{*\alpha_1}_{\Omega} &= \left[\frac{1}{A_1}\frac{\partial}{\partial\alpha_1} + \frac{1}{A_1A_2}\frac{\partial A_2}{\partial\alpha_1} \quad -\frac{1}{A_1A_2}\frac{\partial A_2}{\partial\alpha_1} \quad \frac{1}{A_1A_2}\frac{\partial A_1}{\partial\alpha_2} \quad \frac{1}{A_2}\frac{\partial}{\partial\alpha_2} + \frac{1}{A_1A_2}\frac{\partial A_1}{\partial\alpha_2} \quad \frac{1}{R_1} \quad 0 \quad -1 \quad 0 \quad 0\right] \\
\overline{\mathbf{D}}^{*\alpha_2}_{\Omega} &= \left[-\frac{1}{A_1A_2}\frac{\partial A_1}{\partial\alpha_2} \quad \frac{1}{A_2}\frac{\partial}{\partial\alpha_2} + \frac{1}{A_1A_2}\frac{\partial A_1}{\partial\alpha_2} \quad \frac{1}{A_1}\frac{\partial}{\partial\alpha_1} + \frac{1}{A_1A_2}\frac{\partial A_2}{\partial\alpha_1} \quad \frac{1}{A_1A_2}\frac{\partial A_2}{\partial\alpha_1} \quad 0 \quad \frac{1}{R_2} \quad 0 \quad -1 \quad 0\right] \\
\overline{\mathbf{D}}^{*\alpha_3}_{\Omega} &= \left[-\frac{1}{R_1} \quad -\frac{1}{R_2} \quad 0 \quad 0 \quad \frac{1}{A_1}\frac{\partial}{\partial\alpha_1} + \frac{1}{A_1A_2}\frac{\partial A_2}{\partial\alpha_1} \quad \frac{1}{A_2}\frac{\partial}{\partial\alpha_2} + \frac{1}{A_1A_2}\frac{\partial A_1}{\partial\alpha_2} \quad 0 \quad 0 \quad -1\right]
\end{aligned} \tag{33}$$

The generalized mass matrix $\mathbf{M}^{(\tau\eta)}$ occurring in Eq. (31) assumes the following extended form for each $\tau,\eta = 0,.,N+1$:

$$\mathbf{M}^{(\tau\eta)} = \begin{bmatrix} I_0^{(\tau\eta)\alpha_1\alpha_1} & 0 & 0 \\ 0 & I_0^{(\tau\eta)\alpha_2\alpha_2} & 0 \\ 0 & 0 & I_0^{(\tau\eta)\alpha_3\alpha_3} \end{bmatrix} \quad \text{for} \quad \tau,\eta = 0,.,N+1 \tag{34}$$

where the terms $I_0^{(\tau\eta)\alpha_i\alpha_i}$ are computed as follows:

$$I_0^{(\tau\eta)\alpha_i\alpha_i} = \sum_{k=1}^{l} \int_{\zeta_k}^{\zeta_{k+1}} \rho^{(k)} F^{(k\tau)\alpha_i} F^{(k\eta)\alpha_i} H_1 H_2 d\zeta \tag{35}$$

for $i = 1,2,3$ and $\tau,\eta = 0,.,N+1$. Introducing the unified expression for the displacement field assessed in Eq. (7) in the higher order indefinite equilibrium relations of Eq. (31), the integration by parts rule leads to the final form of the fundamental governing equation, in which the generalized displacement field vector $\mathbf{u}^{(\eta)}$ has the role of unknown variable:

$$\sum_{\eta=0}^{N+1} \mathbf{L}^{(\tau\eta)}\mathbf{u}^{(\eta)} = \sum_{\eta=0}^{N+1} \mathbf{M}^{(\tau\eta)}\ddot{\mathbf{u}}^{(\eta)} \qquad \text{for} \quad \tau = 0,.,N+1 \tag{36}$$

In the previous relation, the $3\times 3$ fundamental matrix $\mathbf{L}^{(\tau\eta)}$ is assessed for each $\tau,\eta = 0,.,N+1$ kinematic expansion order. Starting from Eq. (36) which is valid for an arbitrary $\tau = 0,.,N+1$, the fundamental relations are expanded so that all kinematic expansion orders are taken into account. From the Hamiltonian principle, the natural boundary conditions are enforced at the four edges of the rectangular physical domain $[\alpha_1^0, \alpha_1^1]\times[\alpha_2^0, \alpha_2^1]$. More specifically, the following relations are obtained, for each $\tau$-th expansion order, for the edges located at $\alpha_1 = \alpha_1^0$ or $\alpha_1 = \alpha_1^1$:

$$\begin{aligned} &N_1^{(\tau)\alpha_1} = \overline{N}_1^{(\tau)\alpha_1} \quad \text{or} \quad u_1^{(\tau)} = \overline{u}_1^{(\tau)} \\ &N_{12}^{(\tau)\alpha_2} = \overline{N}_{12}^{(\tau)\alpha_2} \quad \text{or} \quad u_2^{(\tau)} = \overline{u}_2^{(\tau)} \\ &T_1^{(\tau)\alpha_3} = \overline{T}_1^{(\tau)\alpha_3} \quad \text{or} \quad u_3^{(\tau)} = \overline{u}_3^{(\tau)} \end{aligned} \tag{37}$$

In the same way, when $\alpha_2 = \alpha_2^0$ or $\alpha_1 = \alpha_1^1$, it gives:

$$\begin{aligned} &N_{21}^{(\tau)\alpha_1} = \overline{N}_{21}^{(\tau)\alpha_1} \quad \text{or} \quad u_1^{(\tau)} = \overline{u}_1^{(\tau)} \\ &N_2^{(\tau)\alpha_2} = \overline{N}_2^{(\tau)\alpha_2} \quad \text{or} \quad u_2^{(\tau)} = \overline{u}_2^{(\tau)} \\ &T_2^{(\tau)\alpha_3} = \overline{T}_2^{(\tau)\alpha_3} \quad \text{or} \quad u_3^{(\tau)} = \overline{u}_3^{(\tau)} \end{aligned} \tag{38}$$

being $\overline{N}_1^{(\tau)\alpha_1}, \overline{N}_2^{(\tau)\alpha_2}, \overline{N}_{12}^{(\tau)\alpha_2}, \overline{N}_{21}^{(\tau)\alpha_1}, \overline{T}_1^{(\tau)\alpha_3}, \overline{T}_2^{(\tau)\alpha_3}$ and $\overline{u}_1^{(\tau)}, \overline{u}_2^{(\tau)}, \overline{u}_3^{(\tau)}$ the prescribed values of generalized stress resultants or displacement field components, respectively. Starting from Eqs. (37)-(38), the kinematic and static relations are derived, for each $\tau = 0,.,N+1$, for the clamped, free and simply-supported boundary conditions:

$$\begin{aligned} &\text{Clamped (C)} \quad u_1^{(\tau)} = u_2^{(\tau)} = u_3^{(\tau)} = 0 \quad \text{at} \quad \alpha_1 = \alpha_1^0 \ \text{or} \ \alpha_1 = \alpha_1^1 \\ &\qquad\qquad u_1^{(\tau)} = u_2^{(\tau)} = u_3^{(\tau)} = 0 \quad \text{at} \quad \alpha_2 = \alpha_2^0 \ \text{or} \ \alpha_2 = \alpha_2^1 \\ &\text{Free (F)} \quad N_1^{(\tau)\alpha_1} = N_{12}^{(\tau)\alpha_2} = T_1^{(\tau)\alpha_3} = 0 \ \text{at} \ \alpha_1 = \alpha_1^0 \ \text{or} \ \alpha_1 = \alpha_1^1 \\ &\qquad\qquad N_{21}^{(\tau)\alpha_1} = N_2^{(\tau)\alpha_2} = T_2^{(\tau)\alpha_3} = 0 \ \text{at} \ \alpha_2 = \alpha_2^0 \ \text{or} \ \alpha_2 = \alpha_2^1 \\ &\text{SimplySupported (S)} \quad N_1^{(\tau)\alpha_1} = 0, \ u_2^{(\tau)} = u_3^{(\tau)} = 0 \quad \text{at} \quad \alpha_1 = \alpha_1^0 \ \text{or} \ \alpha_1 = \alpha_1^1 \\ &\qquad\qquad N_2^{(\tau)\alpha_2} = 0, \ u_1^{(\tau)} = u_3^{(\tau)} = 0 \quad \text{at} \quad \alpha_2 = \alpha_2^0 \ \text{or} \ \alpha_2 = \alpha_2^1 \end{aligned} \tag{39}$$

When arbitrarily-shaped shells are considered, it is possible to extend the present formulation, based on curvilinear principal coordinates, by means of a coordinate transformation that allows to obtain a rectangular parent element when the shell parametrization in principal coordinates is not available. To this end, a set of natural coordinates $\xi_1, \xi_2 \in [-1,1]$ is introduced starting from the curved edges of the structure. The distortion of the physical domain is performed by means of the following generalizesssd blending functions:

$$\begin{aligned} \alpha_1(\xi_1,\xi_2) &= \frac{1}{2}\Big((1-\xi_2)\overline{\alpha}_{1(1)}(\xi_1) + (1+\xi_1)\overline{\alpha}_{1(2)}(\xi_2) + (1+\xi_2)\overline{\alpha}_{1(3)}(\xi_1) + (1-\xi_1)\overline{\alpha}_{1(4)}(\xi_2)\Big) + \\ &\quad -\frac{1}{4}\Big((1-\xi_1)(1-\xi_2)\alpha_{1(1)} + (1+\xi_1)(1-\xi_2)\alpha_{1(2)} + (1+\xi_1)(1+\xi_2)\alpha_{1(3)} + (1-\xi_1)(1+\xi_2)\alpha_{1(4)}\Big) \\ \alpha_2(\xi_1,\xi_2) &= \frac{1}{2}\Big((1-\xi_2)\overline{\alpha}_{2(1)}(\xi_1) + (1+\xi_1)\overline{\alpha}_{2(2)}(\xi_2) + (1+\xi_2)\overline{\alpha}_{2(3)}(\xi_1) + (1-\xi_1)\overline{\alpha}_{2(4)}(\xi_2)\Big) + \\ &\quad -\frac{1}{4}\Big((1-\xi_1)(1-\xi_2)\alpha_{2(1)} + (1+\xi_1)(1-\xi_2)\alpha_{2(2)} + (1+\xi_1)(1+\xi_2)\alpha_{2(3)} + (1-\xi_1)(1+\xi_2)\alpha_{2(4)}\Big) \end{aligned} \tag{40}$$

For the sake of completeness, in Eq. (40) the four corners of the mapped structure have been denoted by $(\alpha_{1(p)}, \alpha_{2(p)})$ with $p = 1,.,4$. Furthermore, $(\overline{\alpha}_{1(q)}, \overline{\alpha}_{2(q)})$ for $q = 1,.,4$ refers to edges of an arbitrarily-shaped structure in terms of $\alpha_1, \alpha_2$. Accordingly, they are efficiently parametrized employing the well-known NURBS curves. If $u$ is the curvilinear abscissa of the edge at issue identified with $\mathbf{C}(u)$, it gives:

$$\mathbf{C}(u) = \frac{\sum_{i=0}^{n} N_{i,p}(u) w_i \mathbf{P}_i}{\sum_{i=0}^{n} N_{i,p}(u) w_i} \tag{41}$$

where $w_i$ for $i = 0,.,n$ are some proper weighting coefficients, and $N_{i,p}$ are the corresponding Spline basis functions of order $p$, which are computed from a recursive formulation [22] in terms of a knot vector $\mathbf{\Omega}$ of multiplicity $p+1$ and $m$ breakpoints. Accordingly, $\mathbf{P}_i$ for $i = 0,.,n$ collects the control points of the curve.

The fundamental governing equations derived in the previous section can be, now, adjusted for the case of arbitrarily shaped domains starting from the relations reported in Eq. (40). It is useful to calculate, in each point of the physical domain, the determinant of the Jacobian matrix $\mathbf{J}$ of the transformations in hand.

The first order partial derivatives with respect to the principal directions $\alpha_1, \alpha_2$ are computed in terms of natural coordinates $\xi_1, \xi_2$:

$$\begin{bmatrix} \frac{\partial}{\partial\alpha_1} \\ \frac{\partial}{\partial\alpha_2} \end{bmatrix} = \begin{bmatrix} \frac{\partial\xi_1}{\partial\alpha_1} & \frac{\partial\xi_2}{\partial\alpha_1} \\ \frac{\partial\xi_1}{\partial\alpha_2} & \frac{\partial\xi_2}{\partial\alpha_2} \end{bmatrix} \begin{bmatrix} \frac{\partial}{\partial\xi_1} \\ \frac{\partial}{\partial\xi_2} \end{bmatrix} = \begin{bmatrix} \xi_{1,\alpha_1} & \xi_{2,\alpha_1} \\ \xi_{1,\alpha_2} & \xi_{2,\alpha_2} \end{bmatrix} \begin{bmatrix} \frac{\partial}{\partial\xi_1} \\ \frac{\partial}{\partial\xi_2} \end{bmatrix} \tag{42}$$

Following a similar procedure, second order partial derivatives in the physical domain can be expressed in terms of the natural coordinates.

When an arbitrarily-shaped domain is considered, kinematic and static boundary conditions are assessed with respect to the tangential $\mathbf{n}_s$,

normal $\mathbf{n}_\zeta = \mathbf{n}$ and bi-normal $\mathbf{n}_n$ unit vectors of an arbitrary curve lying on the reference surface. These local vectors are conveniently referred to the principal coordinates of the shell under consideration by means of their corresponding cosine directors, namely $\mathbf{n}_n = [n_{n1} \quad n_{n2} \quad 0]^T$, $\mathbf{n}_s = [n_{s1} \quad n_{s2} \quad 0]^T$ and $\mathbf{n}_\zeta = [0 \quad 0 \quad 1]^T$. In this way, the generalized displacement field components $u_n^{(\tau)}, u_s^{(\tau)}, u_\zeta^{(\tau)}$ with respect to $\mathbf{n}_s, \mathbf{n}_\zeta, \mathbf{n}_n$ can be expressed in terms of those of Eq. (7) referred to $\alpha_1, \alpha_2, \zeta$ as follows:

$$\begin{bmatrix} u_n^{(\tau)} \\ u_s^{(\tau)} \\ u_\zeta^{(\tau)} \end{bmatrix} = \begin{bmatrix} n_{n1} & n_{n2} & 0 \\ n_{s1} & n_{s2} & 0 \\ 0 & 0 & 1 \end{bmatrix} \begin{bmatrix} u_1^{(\tau)} \\ u_2^{(\tau)} \\ u_3^{(\tau)} \end{bmatrix} \qquad \text{for} \qquad \tau = 0, ., N+1 \tag{43}$$

In the same way, the generalized stress resultants $N_n^{(\tau)\alpha_1}$, $N_{ns}^{(\tau)\alpha_2}$ and $T_\zeta^{(\tau)\alpha_3}$ are conveniently evaluated from the following relation:

$$\begin{bmatrix} N_n^{(\tau)\alpha_1} \\ N_{ns}^{(\tau)\alpha_2} \\ T_\zeta^{(\tau)\alpha_3} \end{bmatrix} = \begin{bmatrix} n_{n1}^2 & n_{n2}^2 & n_{n1}n_{n2} & n_{n1}n_{n2} & 0 & 0 \\ n_{n1}n_{s1} & n_{n2}n_{s2} & n_{n1}n_{s2} & n_{n2}n_{s1} & 0 & 0 \\ 0 & 0 & 0 & 0 & n_{n1} & n_{n2} \end{bmatrix} \begin{bmatrix} N_1^{(\tau)\alpha_1} \\ N_2^{(\tau)\alpha_1} \\ N_{12}^{(\tau)\alpha_1} \\ N_{21}^{(\tau)\alpha_1} \\ T_1^{(\tau)\alpha_3} \\ T_2^{(\tau)\alpha_3} \end{bmatrix} \tag{44}$$

In this way, the natural boundary conditions outlined in Eqs. (37)-(38), for each $\tau = 0, ., N+1$, turn into:

$$\begin{aligned} N_n^{(\tau)\alpha_1} &= \overline{N}_n^{(\tau)\alpha_1} \quad \text{or} \quad u_n^{(\tau)} = \overline{u}_n^{(\tau)} \\ N_{ns}^{(\tau)\alpha_2} &= \overline{N}_{ns}^{(\tau)\alpha_2} \quad \text{or} \quad u_s^{(\tau)} = \overline{u}_s^{(\tau)} \quad \text{for} \quad \tau = 0, ., N+1 \\ T_\zeta^{(\tau)\alpha_3} &= \overline{T}_\zeta^{(\tau)\alpha_3} \quad \text{or} \quad u_\zeta^{(\tau)} = \overline{u}_\zeta^{(\tau)} \end{aligned} \tag{45}$$

being $\overline{N}_n^{(\tau)\alpha_1}, \overline{N}_{ns}^{(\tau)\alpha_2}, \overline{T}_\zeta^{(\tau)\alpha_3}$ and $\overline{u}_n^{(\tau)}, \overline{u}_s^{(\tau)}, \overline{u}_\zeta^{(\tau)}$ the prescribed values of the generalized displacement field and stress resultant vectors, respectively, acting along the edges of the mapped structure.

## 3. Generalized differential quadrature method

The fundamental governing equations outlined in Eq. (36) is now tackled numerically employing the GDQ method. In this context, a discrete set of points is extracted from the physical domain and a two-dimensional computational grid is defined. More specifically, a discrete set of sampling points is adopted, following the symmetric non-uniform Chebyshev-Gauss-Lobatto (CGL) harmonic dispersion. The arbitrary element $\overline{x}_i$ of the CGL one-dimensional computational grid is selected from the interval $[-1, 1]$ according to the following expression:

$$\overline{x}_i = -\cos\left(\frac{i-1}{I_Q - 1}\pi\right), \qquad i = 1, ., I_Q, \qquad for \quad x_i \in [-1, 1] \tag{46}$$

being $I_Q$ the total number of sampling points. Referring to an arbitrary univariate smooth function $f = f(x)$ defined in a closed interval $[a, b]$, its $n$-th order derivative evaluated at the discrete point $x_i$ with $i = 1, ., I_Q$ is computed as a weighted sum of values $f(x_j)$ for $j = 1, ., I_Q$ assumed by the function itself in the computational grid:

$$f^{(n)}(x_i) = \left.\frac{\partial^n f(x)}{\partial x^n}\right|_{x=x_i} \cong \sum_{j=1}^{I_Q} \varsigma_{ij}^{(n)} f(x_j) \qquad i = 1, 2, ., I_Q \tag{47}$$

$\varsigma_{ij}^{(n)}$ being the GDQ weighting coefficients. These coefficients are evaluated from the first order derivative $\mathscr{L}^{(1)}(x_i), \mathscr{L}^{(1)}(x_j)$ of the Lagrange Polynomials defined from the points $x_i, x_j$ of the computational grid:

$$\begin{aligned} \varsigma_{ij}^{(1)} &= \frac{\mathscr{L}^{(1)}(x_i)}{(x_i - x_j)\mathscr{L}^{(1)}(x_j)}, \qquad \varsigma_{ij}^{(n)} = n\left(\varsigma_{ij}^{(1)}\varsigma_{ii}^{(n-1)} - \frac{\varsigma_{ij}^{(n-1)}}{x_i - x_j}\right) \qquad i \neq j \\ \varsigma_{ii}^{(n)} &= -\sum_{j=1 j\neq i}^{I_N} \varsigma_{ij}^{(n)} \qquad i = j \end{aligned} \tag{48}$$

Note that in the previous equation the definition $\varsigma_{ij}^{(0)} = \delta_{ij}$ with $i, j = 1, ., I_Q$ must be introduced. Moving from Eq. (47), it is also possible to assess the GIQ method for the numerical computation of integrals. If $f = f(x)$ is a univariate smooth function defined in an interval discretized with $I_Q$ points, its integral restricted to the interval $[x_i, x_j]$ can be computed as:

$$\int_{x_i}^{x_j} f(x)dx = \sum_{k=1}^{I_Q} \widetilde{w}_k^{ij} f(x_k) = \sum_{k=1}^{I_Q} (w_{jk} - w_{ik}) f(x_k) \tag{49}$$

Unlike classical integration methods, the procedure outlined in the previous equation does not require any restriction on the discrete grid distribution. It can be shown that the GIQ coefficients $w_{ik}, w_{jk}$ are the elements of the inverse matrix $\mathbf{W} = (\bar{\boldsymbol{\varsigma}}^{(1)})^{-1}$ of the GDQ shifted coefficients of the first order derivative. More details on the topic can be found in Ref. [64].

## 4. Numerical examples

We now present some examples of investigation where the proposed model has been applied, accounting for structures with different curvatures, material properties and boundary conditions. Since a unified formulation has been adopted, the sensitivity of the selection of the thickness function is also checked. Our numerical results are validated with respect to more demanding formulations. Furthermore, some experimental results presented in Ref. [51] have been replicated with success. As will be seen, it can be said that the present ESL model is accurately capable of predicting both the experimental results and numerical predictions of three-dimensional models with a reduced computational cost.

Another aspect that is shown in the examples is that the present formulation provides very accurate results also when the physical domain is distorted through blending functions (40). More specifically, it will be shown that the proposed generalized method employing NURBS curves can be adopted for deforming both curved and straight edges. As far as the boundary conditions implementation is concerned, we adopt a useful nomenclature to define edges in the physical domain, namely:

$$\begin{aligned} &\text{West edge (W)} \quad \rightarrow \quad \xi_2 = -1 \quad \rightarrow \quad (\alpha_1, \alpha_2) = \left(\overline{\alpha}_{1(1)}(\xi_1), \overline{\alpha}_{2(1)}(\xi_1)\right) \\ &\text{South edge (S)} \quad \rightarrow \quad \xi_1 = 1 \quad \rightarrow \quad (\alpha_1, \alpha_2) = \left(\overline{\alpha}_{1(2)}(\xi_2), \overline{\alpha}_{2(2)}(\xi_2)\right) \\ &\text{East edge (E)} \quad \rightarrow \quad \xi_2 = 1 \quad \rightarrow \quad (\alpha_1, \alpha_2) = \left(\overline{\alpha}_{1(3)}(\xi_1), \overline{\alpha}_{2(3)}(\xi_1)\right) \\ &\text{North edge (N)} \quad \rightarrow \quad \xi_1 = -1 \quad \rightarrow \quad (\alpha_1, \alpha_2) = \left(\overline{\alpha}_{1(4)}(\xi_2), \overline{\alpha}_{2(4)}(\xi_2)\right) \end{aligned} \tag{50}$$

where $\overline{\alpha}_{i(q)}(\xi_j)$ for $i, j = 1, 2$ and $q = 1, ., 4$ account for the geometric description of the shell edges according to Eq. (40).

The materials applied in our simulations can be classified in three main groups, namely generally anisotropic, orthotropic and isotropic. The generally anisotropic medium is the triclinic material ($\rho^{(k)} = 7750$ kg/m$^3$), whose three-dimensional stiffness matrix with coefficients $C_{nm}^{(k)} = E_{nm}^{(k)}$ for $n, m = 1, ., 6$ is expressed with respect to the previously discussed material reference system, reading as:

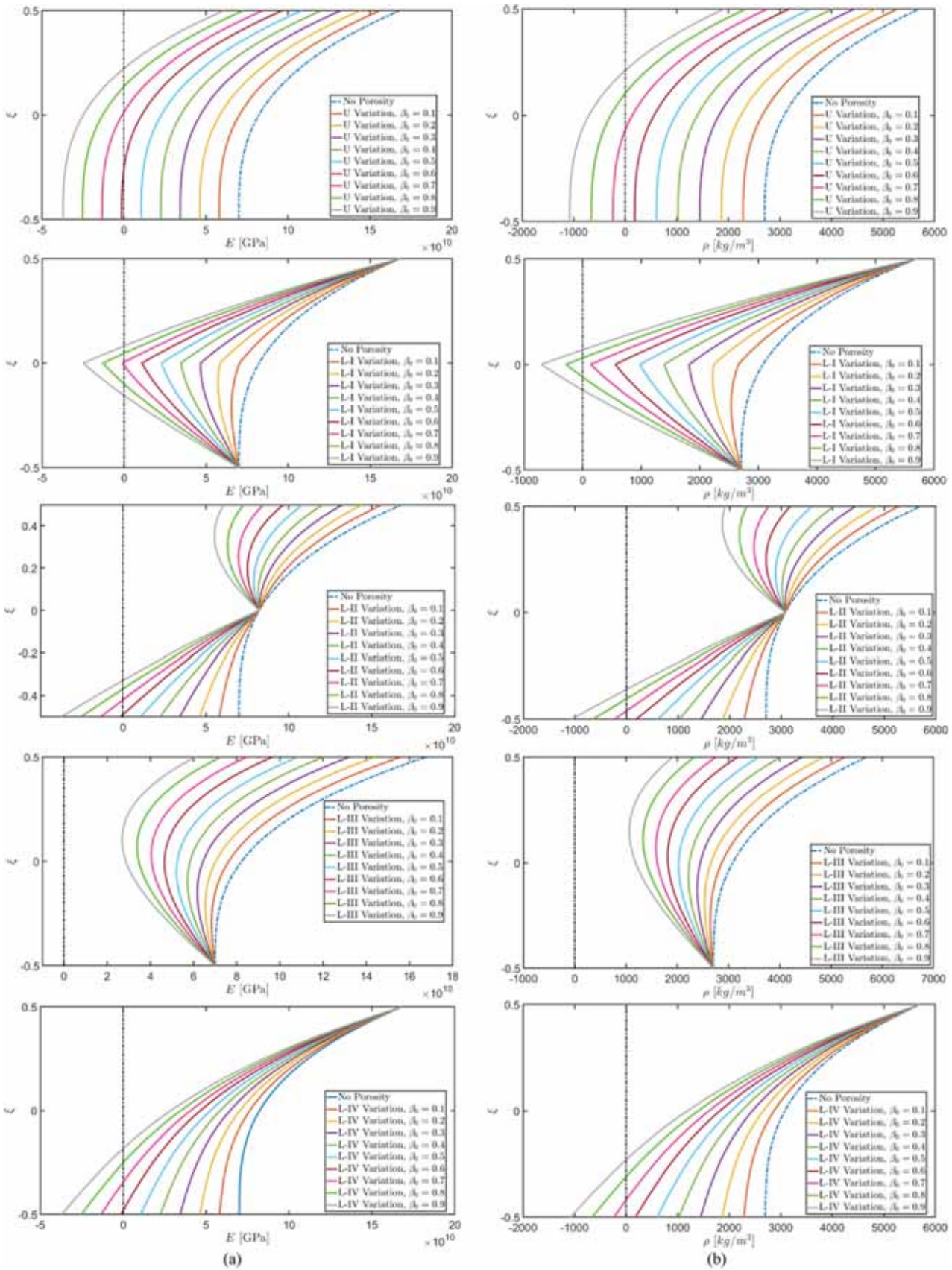


**Fig. 2.** Through-the-thickness distributions of the elastic modulus $E$ and the density $\rho$ of a porous FGM medium with $p = 3$, $a = c = d = 1$ and $b = 0$ collected in (a) and (b), respectively. Different kinds of linear dispersions of porosity have been adopted, and the methodology A2 has been adopted for the computation of the equivalent elastic properties of the material.

**Table 2**
First mode frequency of a laminated simply-supported (SSSS) squared plate mate of two external isotropic layers and a central 3D printed FGM porous core. The simulations have been performed employing higher order theories and have been validated with the outcomes of the experimental work of Ref. [51].

| Mode $f_1$ [Hz] | | Njim et al. [51] | | 2D GDQ Solution | | | | | | | | |
|---|---|---|---|---|---|---|---|---|---|---|---|---|
| | | | | $L-III^{\beta_0^{(2)}}$ | | | $UC-II^{\beta_0^{(2)}}$ | | | $UC-III^{\beta_0^{(2)}}$ | | |
| $h_2$ [m] | $\beta_0$ | Hammer Test | CPT Analytical | CPT | FSDT | EDZ4 | CPT | FSDT | EDZ4 | CPT | FSDT | EDZ4 |
| 0.005 | 0.1 | 253.89 | 285.07 | 284.86 | 284.13 | 281.25 | 286.25 | 285.51 | 282.58 | 283.50 | 282.77 | 279.95 |
| 0.010 | | 398.44 | 427.56 | 426.70 | 423.05 | 415.45 | 429.04 | 425.36 | 417.62 | 424.41 | 420.78 | 413.33 |
| 0.015 | | 488.42 | 544.4 | 542.40 | 533.05 | 520.38 | 545.43 | 536.02 | 523.09 | 539.43 | 530.15 | 517.72 |
| 0.020 | | 592.58 | 648.77 | 645.02 | 627.02 | 609.41 | 648.61 | 630.47 | 612.49 | 641.52 | 623.64 | 606.39 |
| 0.025 | | 682.66 | 745.74 | 739.56 | 709.89 | 687.72 | 743.61 | 713.71 | 691.07 | 735.61 | 706.15 | 684.44 |
| 0.005 | 0.5 | 269.73 | 307.44 | 307.00 | 306.21 | 302.29 | 316.23 | 315.40 | 310.99 | 298.59 | 297.82 | 294.30 |
| 0.010 | | 395.42 | 465.76 | 464.08 | 460.03 | 449.46 | 480.63 | 476.40 | 464.29 | 449.30 | 445.42 | 435.98 |
| 0.015 | | 524.77 | 594.02 | 590.30 | 579.93 | 562.11 | 612.42 | 601.51 | 580.95 | 570.75 | 560.83 | 545.01 |
| 0.020 | | 667.89 | 707.32 | 700.70 | 680.74 | 655.85 | 727.32 | 706.29 | 677.40 | 677.30 | 658.26 | 636.25 |
| 0.025 | | 751.11 | 811.59 | 801.17 | 768.39 | 736.98 | 831.58 | 796.99 | 760.36 | 774.54 | 743.29 | 715.60 |

Geometric Inputs: $(\alpha_1,\alpha_2)\in[\alpha_1^0,\alpha_1^1]\times[\alpha_2^0,\alpha_2^1]$, $\alpha_1^0=\alpha_2^0=0$, $\alpha_1^1=L_x$, $\alpha_2^1=L_y$, $L_x=0.3$ m, $L_y=0.3$ m, $h_1=h_3=0.0005$ m
**Material Properties:** 1st layer: AA6061-T6, 2nd layer: PLA, 3rd layer: AA6061-T6
**Computational Issues:** CGL two-dimensional grid with $I_N$=$I_M$=31

$$\mathbf{E}^{(k)}=\begin{bmatrix} C_{11}^{(k)} & C_{12}^{(k)} & C_{16}^{(k)} & C_{14}^{(k)} & C_{15}^{(k)} & C_{13}^{(k)} \\ C_{12}^{(k)} & C_{22}^{(k)} & C_{26}^{(k)} & C_{24}^{(k)} & C_{25}^{(k)} & C_{23}^{(k)} \\ C_{16}^{(k)} & C_{26}^{(k)} & C_{66}^{(k)} & C_{46}^{(k)} & C_{56}^{(k)} & C_{36}^{(k)} \\ C_{14}^{(k)} & C_{24}^{(k)} & C_{46}^{(k)} & C_{44}^{(k)} & C_{45}^{(k)} & C_{34}^{(k)} \\ C_{15}^{(k)} & C_{25}^{(k)} & C_{56}^{(k)} & C_{45}^{(k)} & C_{55}^{(k)} & C_{35}^{(k)} \\ C_{13}^{(k)} & C_{23}^{(k)} & C_{36}^{(k)} & C_{34}^{(k)} & C_{35}^{(k)} & C_{33}^{(k)} \end{bmatrix} = \begin{bmatrix} 98.84 & 53.92 & 0.03 & 1.05 & -0.1 & 50.78 \\ 53.92 & 99.19 & 0.03 & 0.55 & -0.18 & 50.87 \\ 0.03 & 0.03 & 22.55 & -0.04 & 0.25 & 0.02 \\ 1.05 & 0.55 & -0.04 & 21.1 & 0.07 & 1.03 \\ -0.1 & -0.18 & 0.25 & 0.07 & 21.14 & -0.18 \\ 50.78 & 50.87 & 0.02 & 1.03 & -0.18 & 87.23 \end{bmatrix} \text{ GPa} \tag{51}$$

A graphite-epoxy of density $\rho^{(k)}=1450$ kg/m$^3$ has been considered for the orthotropic material class. Its homogenized material properties have been expressed in terms of the nine elastic engineering constants:

$$\begin{aligned} &E_1^{(k)}=137.90\ \text{GPa} \qquad G_{23}^{(k)}=6.21\ \text{GPa} \qquad \nu_{23}^{(k)}=0.49 \\ &E_2^{(k)}=E_3^{(k)}=8.96\ \text{GPa} \quad G_{12}^{(k)}=G_{13}^{(k)}=7.10\ \text{GPa} \quad \nu_{12}^{(k)}=\nu_{13}^{(k)}=0.30 \end{aligned} \tag{52}$$

being $E_1^{(k)},E_2^{(k)},E_3^{(k)}$ and $G_{12}^{(k)},G_{13}^{(k)},G_{23}^{(k)}$ the elastic tensile and shear moduli, respectively, whereas $\nu_{12}^{(k)},\nu_{13}^{(k)},\nu_{23}^{(k)}$ denote the Poisson's coefficients. For the derivation of the generalized Hooke's law for orthotropic materials starting from engineering constants, the interested reader should refer to Ref. [22].

Most numerical investigations account for the presence of a FGM layer obtained from ceramic and metal. In this manuscript, two isotropic constituent materials have been considered. The metal phase is made of aluminum, whereas the ceramic one consists of zirconia. In the following, the material properties of such constituents have been reported:

$$\begin{aligned} &\text{Aluminium(M)} \rightarrow E^{(k)}=70.00\ \text{GPa}, \quad \nu^{(k)}=0.3, \quad \rho^{(k)}=2707\ \text{kg/m}^3 \\ &\text{Zirconia(C)} \rightarrow E^{(k)}=168.00\ \text{GPa}, \quad \nu^{(k)}=0.3, \quad \rho^{(k)}=5700\ \text{kg/m}^3 \end{aligned} \tag{53}$$

As can be seen, the ceramic material has a higher elastic modulus and density than those ones associated to metal. As a consequence, the presence of aluminum leads to a soft lightweight FGM medium.

A preliminary check has been performed in Fig. 2 for the selection of the governing parameters of the porous FGM layers made of aluminum (M) and zirconia (C), accounting for the various through-the-thickness distributions, as outlined in Fig. 1, setting by $a^{(k)}=c^{(k)}=d^{(k)}=1$ and $b^{(k)}=0$. The A2 approach has been followed for the computation of the elastic modulus (a) and density (b) of the porous FGM layer, accounting for different values of $\beta_0^{(k)}$. As can be seen from Fig. 2, when $p^{(k)}=3$ only the employment of the $L-III^{\beta_0}$ variation provides positive values regardless the selection of the porosity scaling parameter, whereas for the other configurations the A2 methodology cannot be adopted when $\beta_0^{(k)}$ gets higher, for the selected C and M materials. Similar investigations can be made for FGM materials with $p^{(k)}=0.5$. In this case, the A2 approach can be always adopted for both the $L-I^{\beta_0}$ and $L-III^{\beta_0}$ porosity distributions, whereas for the $L-II^{\beta_0}$ and $L-IV^{\beta_0}$ expressions the methodology is suitable only for lower values of $\beta_0^{(k)}$.

### 4.1. Validation of the model from experimental dynamic test

The formulation proposed in the manuscript for the dynamic analysis of doubly-curved shell structures made of porous FGM material is now adopted to replicate the results of the experimental dynamic tests held on some 3D printed plates reported in Ref. [51]. In the research work at issue, the first mode frequency of simply-supported squared plates made of a central porous isotropic material has been measured with a hammer dynamic test for various geometric slenderness ratios, and the results have been compared to those obtained from closed-form analytical solutions, based on CPT.

We now focus on the numerical implementation of the CPT structural problem with the GDQ method of Eq. (47). Furthermore, some simulations have been performed on the same structure employing the higher order theories. The results have been reported in Table 2.

For the sake of completeness, we recall that a rectangular plate can be geometrically described according to Eq. (1) employing for the reference surface $\mathbf{r}(\alpha_1,\alpha_2)$ the following expression:

$$\mathbf{r}(\alpha_1,\alpha_2)=\alpha_1\,\mathbf{e}_1+\alpha_2\,\mathbf{e}_2 \tag{54}$$

where $\alpha_1\in[\alpha_1^0,\alpha_1^1]=[0,L_x]$ and $\alpha_2\in[\alpha_2^0,\alpha_2^1]=[0,L_y]$. According to Ref. [51], some squared specimens have been prepared, characterized by $L_x=L_y=0.3$ m. They consist of two external isotropic layers of constant thickness $h_1=h_3=0.0005$ m, and they are made of AA6061-T6 material of density $\rho^{(1)}=\rho^{(3)}=2702$ kg/m$^3$ and elastic constants equal to $E^{(1)}=E^{(3)}=70$ GPa and $\nu^{(1)}=\nu^{(3)}=0.3$. The central core is made of porous Polylactic Acid (PLA), accounting for a linear distribution of porosity along the thickness of the plate. The elastic modulus of the dense PLA material, set equal to $E^{(2)}=2.40$ GPa, was already determined in some experimental tests, whereas a Poisson' s

**Table 3**
Mode frequencies of an isotropic fully clamped (CCCC) rectangular plate characterized by different through-the-thickness distributions of porosity of the constituent material.

| $\beta_0$ | 0.00 | | 0.10 | 0.15 | 0.20 | 0.25 | 0.30 | 0.40 | 0.50 | 0.60 | 0.70 | 0.80 | 0.90 |
|---|---|---|---|---|---|---|---|---|---|---|---|---|---|
| Mode$f$ [Hz] | 3D FEM | ED4 | ED4 | | | | | | | | | | |
| $U^{\beta_0}$ | | | | | | | | | | | | | |
| 1 | 291.17 | 291.13 | 288.59 | 287.45 | 286.40 | 285.43 | 284.54 | 282.99 | 281.73 | 280.75 | 280.03 | 279.57 | 279.37 |
| 2 | 414.72 | 414.67 | 411.21 | 409.66 | 408.23 | 406.91 | 405.70 | 403.60 | 401.90 | 400.58 | 399.64 | 399.06 | 398.83 |
| 3 | 623.62 | 623.57 | 618.65 | 616.46 | 614.43 | 612.57 | 610.86 | 607.91 | 605.54 | 603.74 | 602.48 | 601.75 | 601.55 |
| $L-I^{\beta_0}$ | | | | | | | | | | | | | |
| 1 | 291.17 | 291.13 | 293.96 | 295.51 | 297.15 | 298.89 | 300.73 | 304.74 | 309.23 | 314.25 | 319.84 | 326.02 | 332.75 |
| 2 | 414.72 | 414.67 | 418.65 | 420.81 | 423.11 | 425.53 | 428.10 | 433.66 | 439.87 | 446.76 | 454.39 | 462.74 | 471.68 |
| 3 | 623.62 | 623.57 | 629.38 | 632.54 | 635.88 | 639.40 | 643.11 | 651.13 | 660.01 | 669.79 | 680.48 | 691.97 | 703.90 |
| $L-II^{\beta_0}$ | | | | | | | | | | | | | |
| 1 | 291.17 | 291.13 | 285.66 | 282.86 | 279.99 | 277.05 | 274.01 | 267.56 | 260.48 | 252.51 | 243.32 | 232.40 | 219.00 |
| 2 | 414.72 | 414.67 | 407.10 | 403.21 | 399.23 | 395.13 | 390.90 | 381.91 | 372.00 | 360.82 | 347.89 | 332.50 | 313.56 |
| 3 | 623.62 | 623.57 | 612.63 | 606.99 | 601.22 | 595.27 | 589.11 | 576.00 | 561.49 | 545.08 | 526.01 | 503.23 | 475.06 |
| $L-III^{\beta_0}$ | | | | | | | | | | | | | |
| 1 | 291.17 | 291.13 | 289.71 | 288.94 | 288.11 | 287.21 | 286.22 | 283.88 | 280.85 | 276.82 | 271.27 | 263.39 | 251.80 |
| 2 | 414.72 | 414.67 | 412.73 | 411.67 | 410.54 | 409.30 | 407.93 | 404.69 | 400.49 | 394.86 | 387.10 | 376.05 | 359.76 |
| 3 | 623.62 | 623.57 | 620.80 | 619.30 | 617.67 | 615.89 | 613.92 | 609.24 | 603.14 | 594.95 | 583.59 | 567.37 | 543.36 |
| $L-IV^{\beta_0}$ | | | | | | | | | | | | | |
| 1 | 291.17 | 291.13 | 289.71 | 288.94 | 288.11 | 287.21 | 286.22 | 283.88 | 280.85 | 276.82 | 271.27 | 263.39 | 251.80 |
| 2 | 414.72 | 414.67 | 412.73 | 411.67 | 410.54 | 409.30 | 407.93 | 404.69 | 400.49 | 394.86 | 387.10 | 376.05 | 359.76 |
| 3 | 623.62 | 623.57 | 620.80 | 619.30 | 617.67 | 615.89 | 613.92 | 609.24 | 603.14 | 594.95 | 583.59 | 567.37 | 543.36 |
| $SC-I^{\beta_0}$ | | | | | | | | | | | | | |
| 1 | 291.17 | 291.13 | 285.65 | 282.86 | 280.02 | 277.13 | 274.17 | 268.00 | 261.41 | 254.29 | 246.47 | 237.74 | 227.82 |
| 2 | 414.72 | 414.67 | 407.07 | 403.19 | 399.24 | 395.21 | 391.08 | 382.46 | 373.25 | 363.26 | 352.26 | 339.96 | 325.96 |
| 3 | 623.62 | 623.57 | 612.56 | 606.93 | 601.19 | 595.32 | 589.30 | 576.72 | 563.22 | 548.54 | 532.33 | 514.14 | 493.38 |
| $SC-II^{\beta_0}$ | | | | | | | | | | | | | |
| 1 | 291.17 | 291.13 | 294.08 | 295.76 | 297.58 | 299.57 | 301.72 | 306.59 | 312.31 | 319.03 | 326.88 | 335.94 | 345.78 |
| 2 | 414.72 | 414.67 | 418.82 | 421.18 | 423.73 | 426.50 | 429.51 | 436.27 | 444.18 | 453.40 | 464.08 | 476.17 | 488.81 |
| 3 | 623.62 | 623.57 | 629.66 | 633.11 | 636.84 | 640.87 | 645.22 | 654.98 | 666.30 | 679.35 | 694.20 | 710.49 | 726.27 |
| $UC-I^{\beta_0}$ | | | | | | | | | | | | | |
| 1 | 291.17 | 291.13 | 289.13 | 288.04 | 286.88 | 285.62 | 284.27 | 281.18 | 277.47 | 272.93 | 267.30 | 260.17 | 250.99 |
| 2 | 414.72 | 414.67 | 411.92 | 410.41 | 408.80 | 407.06 | 405.18 | 400.89 | 395.72 | 389.39 | 381.49 | 371.50 | 358.60 |
| 3 | 623.62 | 623.57 | 619.61 | 617.44 | 615.11 | 612.60 | 609.87 | 603.65 | 596.12 | 586.87 | 575.31 | 560.62 | 541.61 |
| $UC-II^{\beta_0}$ | | | | | | | | | | | | | |
| 1 | 291.17 | 291.13 | 290.28 | 289.83 | 289.34 | 288.79 | 288.15 | 286.48 | 283.96 | 279.94 | 273.31 | 261.87 | 240.74 |
| 2 | 414.72 | 414.67 | 413.54 | 412.93 | 412.27 | 411.52 | 410.65 | 408.35 | 404.84 | 399.24 | 389.96 | 373.88 | 344.13 |
| 3 | 623.62 | 623.57 | 622.00 | 621.15 | 620.22 | 619.16 | 617.92 | 614.61 | 609.52 | 601.34 | 587.72 | 564.07 | 520.11 |
| $UC-III^{\beta_0}$ | | | | | | | | | | | | | |
| 1 | 291.17 | 291.13 | 289.13 | 288.04 | 286.88 | 285.62 | 284.27 | 281.18 | 277.47 | 272.93 | 267.30 | 260.17 | 250.99 |
| 2 | 414.72 | 414.67 | 411.92 | 410.41 | 408.80 | 407.06 | 405.18 | 400.89 | 395.72 | 389.39 | 381.49 | 371.50 | 358.60 |
| 3 | 623.62 | 623.57 | 619.61 | 617.44 | 615.11 | 612.60 | 609.87 | 603.65 | 596.12 | 586.87 | 575.31 | 560.62 | 541.61 |
| $UC-IV^{\beta_0}$ | | | | | | | | | | | | | |
| 1 | 291.17 | 291.13 | 290.28 | 289.83 | 289.34 | 288.79 | 288.15 | 286.48 | 283.96 | 279.94 | 273.31 | 261.87 | 240.74 |
| 2 | 414.72 | 414.67 | 413.54 | 412.93 | 412.27 | 411.52 | 410.65 | 408.35 | 404.84 | 399.24 | 389.96 | 373.88 | 344.13 |
| 3 | 623.62 | 623.57 | 622.00 | 621.15 | 620.22 | 619.16 | 617.92 | 614.61 | 609.52 | 601.34 | 587.72 | 564.07 | 520.11 |
| $HS-I^{\beta_0}$ | | | | | | | | | | | | | |
| 1 | 291.17 | 291.13 | 293.34 | 294.70 | 296.25 | 298.00 | 299.98 | 304.72 | 310.70 | 318.27 | 327.87 | 340.01 | 354.25 |
| 2 | 414.72 | 414.67 | 417.81 | 419.73 | 421.91 | 424.37 | 427.15 | 433.76 | 442.07 | 452.51 | 465.63 | 481.92 | 500.12 |
| 3 | 623.62 | 623.57 | 628.22 | 631.06 | 634.26 | 637.87 | 641.93 | 651.53 | 663.51 | 678.41 | 696.85 | 719.02 | 741.47 |
| $HS-II^{\beta_0}$ | | | | | | | | | | | | | |
| 1 | 291.17 | 291.13 | 286.50 | 284.16 | 281.81 | 279.44 | 277.03 | 272.13 | 267.05 | 261.75 | 256.18 | 250.26 | 243.94 |
| 2 | 414.72 | 414.67 | 408.23 | 404.98 | 401.70 | 398.39 | 395.04 | 388.19 | 381.09 | 373.66 | 365.84 | 357.53 | 348.63 |
| 3 | 623.62 | 623.57 | 614.22 | 609.50 | 604.73 | 599.91 | 595.02 | 585.01 | 574.61 | 563.72 | 552.23 | 539.98 | 526.83 |
| $HT-I^{\beta_0}$ | | | | | | | | | | | | | |
| 1 | 291.17 | 291.13 | 293.64 | 295.15 | 296.83 | 298.72 | 300.82 | 305.75 | 311.84 | 319.37 | 328.68 | 340.07 | 352.91 |
| 2 | 414.72 | 414.67 | 418.23 | 420.35 | 422.72 | 425.36 | 428.29 | 435.17 | 443.61 | 453.98 | 466.67 | 481.90 | 498.20 |
| 3 | 623.62 | 623.57 | 628.82 | 631.94 | 635.41 | 639.27 | 643.55 | 653.51 | 665.65 | 680.40 | 698.14 | 718.73 | 738.56 |
| $HT-II^{\beta_0}$ | | | | | | | | | | | | | |
| 1 | 291.17 | 291.13 | 286.17 | 283.66 | 281.13 | 278.56 | 275.96 | 270.62 | 265.05 | 259.18 | 252.94 | 246.25 | 238.98 |
| 2 | 414.72 | 414.67 | 407.78 | 404.29 | 400.76 | 397.19 | 393.56 | 386.10 | 378.30 | 370.07 | 361.32 | 351.90 | 341.66 |
| 3 | 623.62 | 623.57 | 613.57 | 608.50 | 603.36 | 598.16 | 592.87 | 581.97 | 570.55 | 558.48 | 545.59 | 531.70 | 516.55 |

Geometric Inputs: $(\alpha_1, \alpha_2) \in [\alpha^0_1, \alpha^1_1] \times [\alpha^0_2, \alpha^1_2]$, $\alpha^0_1 = \alpha^0_2 = 0$, $\alpha^1_1 = L_x$, $\alpha^1_2 = L_y$, $L_x = 2.5$ m, $L_y = 1.5$ m
**Material Properties:** zirconia, $h_1 = 0.10$ m

coefficient equal to $\nu^{(2)} = 0.3$ is considered. Finally, the density of the PLA adopted in the simulations is $\rho^{(2)} = 1360$ kg/m$^3$.

Five different central core thicknesses have been assigned to the model. For each specimen, a linear distribution of porosity has been assigned along the thickness of the structure. Accordingly, a low and a high porosity parameter $\beta^{(2)} = 0.1$ and $\beta^{(2)} = 0.5$ have been considered. The results show that the numerical GDQ technique combined to a higher order theory does not provide any improvement of accuracy of the formulation with respect to experimental results, especially for the case of low porosity thin plates. Generally speaking, when the thickness

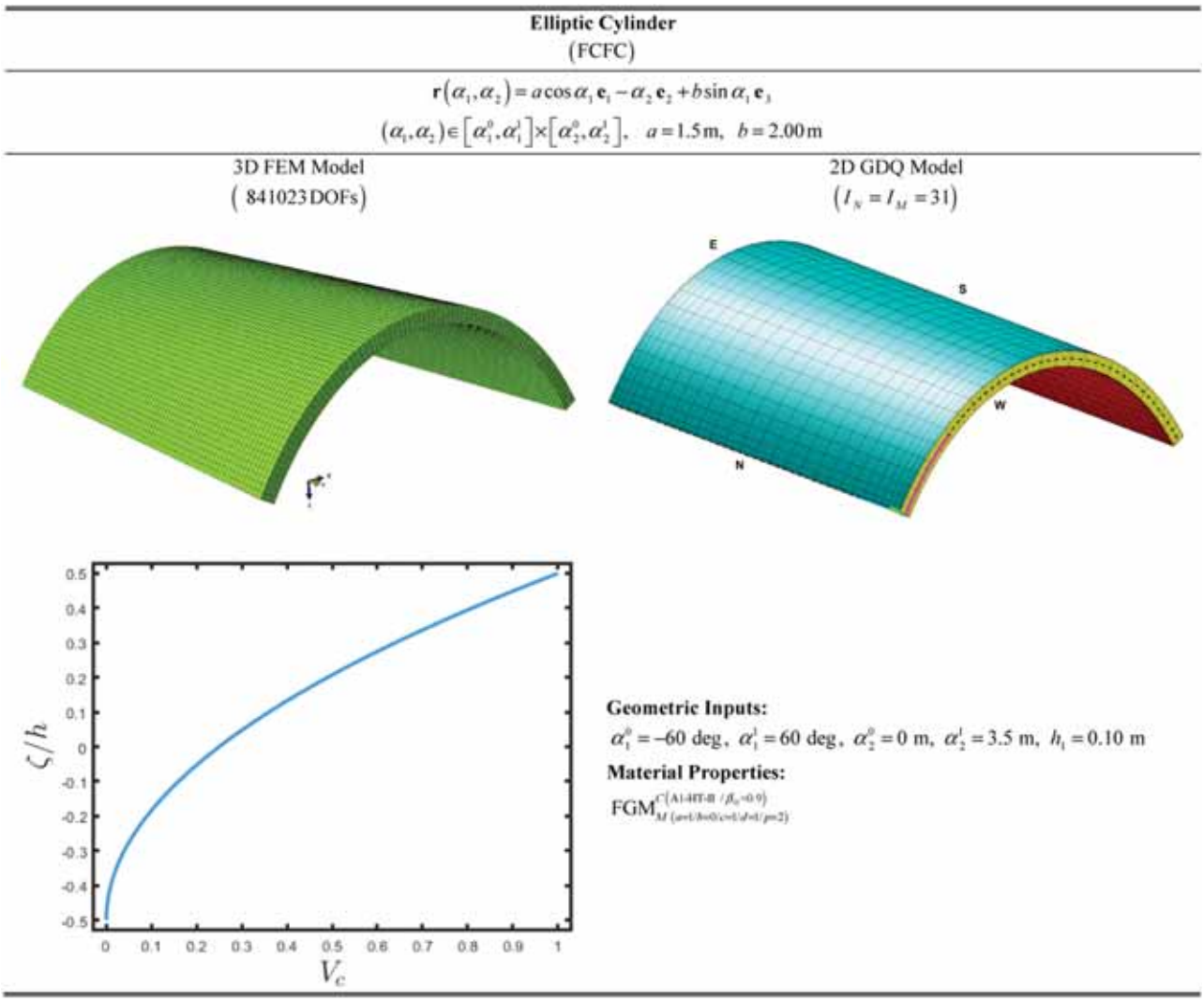


**Fig. 3.** Geometric and mechanical properties of an elliptic cylinder characterized by an FGM core with different kinds of porosity through-the-thickness distribution. The physical domain has been described employing a curvilinear set of principal coordinates.

of the specimen gets higher, a better agreement between the experimental outcomes and those coming from numerical simulations is seen. Above all, an excellent alignment with respect to the CPT analytical predictions can be seen. As visible in Table 2, when non-linear through-the-thickness porosity distributions are adopted in the model, the experimental results are well predicted for both lower and higher core thicknesses, especially for highly porous plates. This means that a discrepancy exists between the theoretical linear distribution assigned to the structure and the actual one obtained from the manufacturing 3D printing process. For this reason, only a computational model accounting for non-linear dispersions can be suitable for well predicting the actual dynamic behavior of porous plates.

### 4.2. Examples of investigation

In the present section, the proposed formulation is adopted for a sensitivity analysis performed on structures with different materials and curvatures, taking into account the influence of FGM porous layers on the dynamic response of laminated structures. Three panels are now presented of zero, single and double curvature, respectively. For the first case, a single layer of isotropic porous material is considered, whereas the second structure accounts for a porous FGM layer. The third panel is a generally anisotropic laminated structure, characterized by a central core made of a porous FGM layer. Furthermore, a thickness variation is considered alongside the physical domain.

The first example is performed on a fully clamped (CCCC) rectangular plate made of a single zirconia layer (53). The first three mode frequencies are computed employing the ED4 higher order theory. In Table 3 the results for the dense layer are reported, and they are compared with success to those ones obtained from a refined three-dimensional FEM simulation. Then, the influence of the porosity parameter $\beta_0$ is outlined with uniform, symmetric and non-symmetric through-the-thickness distributions (Table 1). As can be seen, when a uniform distribution is adopted, a slight decrease of each frequency is seen with respect to the corresponding simulation with dense material. On the other hand, an increase of the vibration frequencies is seen when a $\mathrm{L}-\mathrm{I}^{\beta_0}$ distribution is adopted. A similar behavior is found with the $\mathrm{SC}-\mathrm{II}^{\beta_0}$, the $\mathrm{HS}-\mathrm{I}^{\beta_0}$ and the $\mathrm{HT}-\mathrm{II}^{\beta_0}$ porosity since all of them concentrate the porosity in the middle thickness of the layer. When symmetric porosity dispersions are adopted within the model which allocate voids at the extrados and the intrados of the structure (Fig. 1), namely $\mathrm{L}-\mathrm{II}^{\beta_0}$, $\mathrm{SC}-\mathrm{I}^{\beta_0}$, $\mathrm{HS}-\mathrm{II}^{\beta_0}$ and $\mathrm{HT}-\mathrm{I}^{\beta_0}$, a significative reduction of the frequency is obtained.

A similar parametric analysis is conducted on an elliptic cylinder clamped along its straight edges (FCFC), consisting in a single layer of FGM material with porosity. The geometric representation of the structure, as well as a graphic representation of a three-dimensional

**Table 4**
Mode frequencies of an FGM elliptic cylinder (FCFC) characterized by different through-the-thickness distributions of porosity of the constituent material. The material porosity has been embedded in the free vibration analysis considering different approaches for the homogenization.

| Mode $f$ [Hz] | | 1 | 2 | 3 | 4 | 5 | 6 | 7 | 8 | 9 | 10 |
|---|---|---|---|---|---|---|---|---|---|---|---|
| $\beta_0 = 0$ | | $p = 0$ | | | | | | | | | |
| 3D FEM | | 145.74 | 238.32 | 299.07 | 302.10 | 399.94 | 425.40 | 504.85 | 528.30 | 545.64 | 556.52 |
| FSDT | | 145.32 | 238.07 | 298.15 | 301.22 | 399.95 | 425.01 | 504.44 | 526.38 | 545.62 | 554.89 |
| ED4 | | 145.69 | 238.30 | 298.97 | 302.01 | 399.92 | 425.33 | 504.80 | 528.12 | 545.62 | 556.36 |
| $\beta_0 = 0$ | | $p = 2$ | | | | | | | | | |
| ED4 | | 139.44 | 229.62 | 286.01 | 289.00 | 385.95 | 408.67 | 486.62 | 505.07 | 525.74 | 532.86 |
| $U^{\beta_0}$ | | | | | | | | | | | |
| $\beta_0 = 0.5$ | A1 | 135.20 | 234.00 | 278.32 | 285.10 | 385.66 | 406.00 | 491.78 | 499.54 | 522.28 | 524.76 |
| | A2 | 113.17 | 215.13 | 234.65 | 241.98 | 356.76 | 359.38 | 414.11 | 443.56 | 471.93 | 488.11 |
| | A3 | 132.72 | 234.48 | 273.69 | 280.82 | 387.85 | 402.83 | 483.40 | 504.34 | 514.70 | 526.79 |
| $\beta_0 = 0.9$ | A1 | 134.01 | 239.57 | 276.25 | 285.06 | 387.38 | 407.75 | 488.50 | 510.58 | 522.28 | 524.80 |
| | A2 | 330.07 | 761.56 | 778.30 | 1010.20 | 1040.77 | 1572.03 | 1667.76 | 1667.76 | 1898.64 | 2110.02 |
| | A3 | 115.04 | 233.28 | 239.45 | 248.95 | 373.71 | 382.01 | 422.94 | 457.29 | 504.95 | 518.02 |
| $L - I^{\beta_0}$ | | | | | | | | | | | |
| $\beta_0 = 0.5$ | A1 | 147.32 | 238.87 | 300.67 | 303.77 | 395.78 | 427.70 | 498.11 | 530.80 | 540.33 | 560.04 |
| | A2 | 146.86 | 237.72 | 299.24 | 302.17 | 393.83 | 425.54 | 494.73 | 527.62 | 537.49 | 556.61 |
| | A3 | 144.31 | 237.36 | 295.31 | 298.93 | 394.54 | 422.38 | 499.34 | 521.49 | 538.17 | 550.80 |
| $\beta_0 = 0.9$ | A1 | 157.51 | 248.88 | 318.40 | 320.56 | 407.30 | 448.99 | 507.46 | 556.50 | 560.36 | 570.34 |
| | A2 | 152.06 | 242.09 | 303.18 | 305.12 | 396.72 | 428.84 | 493.50 | 524.34 | 539.62 | 553.18 |
| | A3 | 149.87 | 244.97 | 305.63 | 309.39 | 403.76 | 436.49 | 510.71 | 539.17 | 550.91 | 569.96 |
| $L - III^{\beta_0}$ | | | | | | | | | | | |
| $\beta_0 = 0.5$ | A1 | 139.42 | 233.31 | 286.42 | 291.15 | 384.08 | 408.52 | 494.12 | 506.06 | 519.91 | 535.08 |
| | A2 | 142.31 | 235.73 | 291.71 | 296.11 | 386.78 | 414.52 | 495.72 | 515.30 | 523.58 | 544.57 |
| | A3 | 141.50 | 236.61 | 290.39 | 295.03 | 388.93 | 414.23 | 499.83 | 512.94 | 526.29 | 542.41 |
| $\beta_0 = 0.9$ | A1 | 129.88 | 227.30 | 268.43 | 274.84 | 372.78 | 387.24 | 474.20 | 489.61 | 501.82 | 503.19 |
| | A2 | 144.95 | 239.99 | 296.82 | 302.18 | 387.03 | 419.22 | 501.40 | 520.80 | 524.48 | 555.02 |
| | A3 | 144.72 | 243.77 | 296.91 | 302.65 | 393.62 | 422.15 | 512.58 | 524.70 | 529.21 | 555.87 |
| $SC - I^{\beta_0}$ | | | | | | | | | | | |
| $\beta_0 = 0.5$ | A1 | 125.98 | 222.14 | 260.48 | 266.44 | 374.14 | 382.60 | 460.03 | 483.08 | 488.17 | 508.71 |
| | A2 | 119.71 | 217.09 | 248.07 | 254.13 | 366.71 | 368.34 | 438.08 | 465.77 | 476.13 | 497.98 |
| | A3 | 128.84 | 225.30 | 266.01 | 271.87 | 378.24 | 389.27 | 469.71 | 487.29 | 498.22 | 513.90 |
| $\beta_0 = 0.9$ | A1 | 110.04 | 211.25 | 229.14 | 236.24 | 349.15 | 358.15 | 404.67 | 432.90 | 467.45 | 486.96 |
| | A2 | 91.10 | 190.62 | 196.02 | 196.51 | 304.25 | 329.10 | 336.74 | 363.96 | 421.92 | 438.61 |
| | A3 | 118.83 | 220.43 | 246.58 | 253.77 | 369.03 | 369.65 | 435.42 | 464.65 | 482.47 | 500.30 |
| $SC - II^{\beta_0}$ | | | | | | | | | | | |
| $\beta_0 = 0.5$ | A1 | 148.74 | 240.92 | 303.32 | 306.62 | 397.78 | 431.45 | 500.97 | 535.54 | 543.04 | 565.40 |
| | A2 | 147.02 | 238.46 | 299.29 | 302.46 | 393.99 | 426.12 | 495.60 | 527.37 | 537.49 | 556.80 |
| | A3 | 144.64 | 238.88 | 296.02 | 300.02 | 396.07 | 424.19 | 502.58 | 522.75 | 540.09 | 552.68 |
| $\beta_0 = 0.9$ | A1 | 163.37 | 254.96 | 327.87 | 329.47 | 414.09 | 460.50 | 513.18 | 565.72 | 573.53 | 575.19 |
| | A2 | 185.32 | 265.18 | 365.90 | 399.62 | 403.19 | 408.99 | 420.07 | 437.76 | 462.43 | 522.02 |
| | A3 | 151.38 | 248.68 | 308.45 | 312.71 | 408.04 | 441.51 | 517.78 | 543.81 | 556.35 | 575.64 |
| $UC - IV^{\beta_0}$ | | | | | | | | | | | |
| $\beta_0 = 0.5$ | A1 | 141.85 | 236.11 | 291.06 | 295.87 | 386.58 | 414.06 | 497.64 | 514.31 | 523.08 | 543.94 |
| | A2 | 145.44 | 238.92 | 297.47 | 301.78 | 389.56 | 421.21 | 498.93 | 525.44 | 527.20 | 555.37 |
| | A3 | 143.21 | 239.24 | 293.69 | 298.52 | 391.54 | 418.67 | 504.08 | 518.81 | 529.62 | 548.91 |
| $\beta_0 = 0.9$ | A1 | 128.14 | 226.74 | 265.08 | 272.10 | 370.52 | 383.41 | 468.12 | 489.19 | 497.29 | 498.11 |
| | A2 | 155.49 | 248.94 | 315.51 | 320.00 | 395.25 | 439.58 | 507.88 | 531.64 | 556.77 | 565.89 |
| | A3 | 149.67 | 250.45 | 306.35 | 312.30 | 400.71 | 434.08 | 522.97 | 538.22 | 541.48 | 573.94 |
| $HT - II^{\beta_0}$ | | | | | | | | | | | |
| $\beta_0 = 0.5$ | A1 | 127.53 | 222.65 | 263.44 | 268.96 | 375.37 | 385.34 | 465.19 | 482.99 | 492.91 | 510.70 |
| | A2 | 122.84 | 218.90 | 254.20 | 259.83 | 369.90 | 374.70 | 448.86 | 476.25 | 478.27 | 502.69 |
| | A3 | 130.11 | 225.38 | 268.41 | 273.84 | 378.84 | 391.26 | 473.90 | 486.37 | 501.94 | 515.13 |
| $\beta_0 = 0.9$ | A1 | 115.13 | 214.07 | 239.20 | 245.76 | 359.33 | 363.18 | 422.36 | 450.16 | 472.98 | 493.75 |
| | A2 | 103.48 | 204.84 | 215.78 | 221.86 | 331.56 | 347.12 | 381.11 | 408.02 | 450.69 | 471.06 |
| | A3 | 121.94 | 221.16 | 252.63 | 259.24 | 371.76 | 374.69 | 446.02 | 474.71 | 483.09 | 503.73 |

FEM mesh, is reported in Fig. 3. In the following, the parametrization of the structure in principal coordinates according to Eq. (1) can be found, setting $a = 1.50$ m and $b = 2.00$ m:

$$\mathbf{r}(\alpha_1, \alpha_2) = a \cos \alpha_1 \, \mathbf{e}_1 - \alpha_2 \, \mathbf{e}_2 + b \sin \alpha_1 \, \mathbf{e}_3 \tag{55}$$

The material FGM distribution is selected so that at the lower and upper side, there is a pure isotropic metal and ceramic, respectively. A three-dimensional FEM model with the 20-nodes mesh reported in Fig. 3 is adopted as a reference simulation, accounting for a dense isotropic material ($\beta_0 = 0$ and $p = 0$). The unified formulation of Eq. (7) is employed for the derivation of the first ten natural frequencies of the structure through the classical FSDT approach and the ED4 theory, and the accuracy of the two-dimensional higher order model is outlined for both lower and higher modes, as can be seen from Table 4. Furthermore, the ED4 kinematic assumption is adopted for the dynamic analysis of the same structure made of FGM material with various porosity distributions, accounting for low and high values of $\beta_0$. For each case, the influence of the approach for the homogenization of the porous FGM material is investigated. It is shown that the three methodologies at issue affect the numerical results for both lower and higher modes. In addition, for the high porosity case, the variation of results coming from the three different approaches becomes more evident.

Next, we perform some numerical investigations for a spherical panel of variable thickness. All the geometric and mechanical information, as well as a three-dimensional representation of the models, have been reported in Fig. 4. The equation of the reference surface at issue reads as:

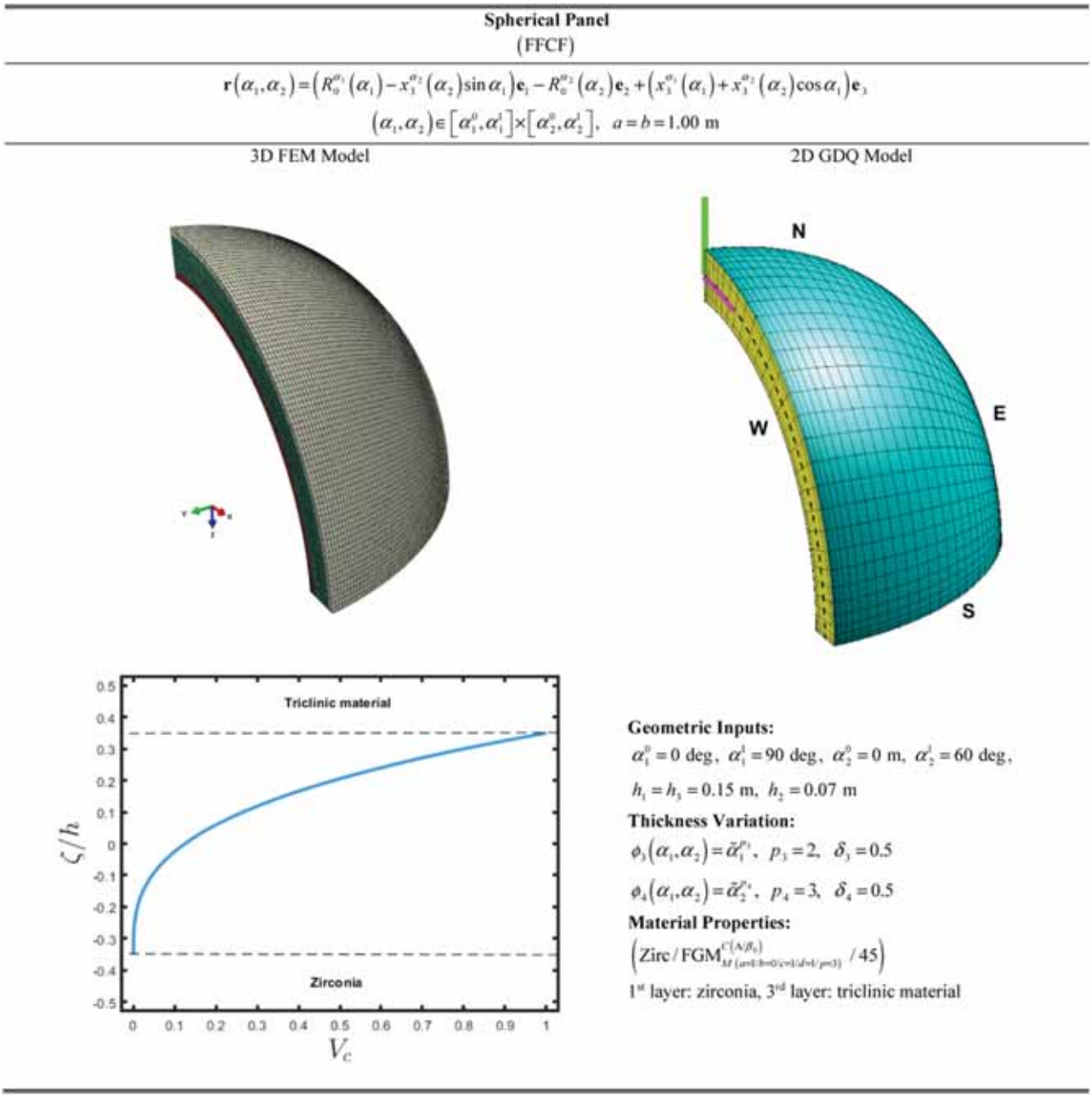


**Fig. 4.** Geometric and mechanical properties of a spherical panel characterized by an FGM core with different kinds of porosity through-the-thickness distribution. The physical domain has been described employing a curvilinear set of principal coordinates.

$$\mathbf{r}(\alpha_1,\alpha_2)=(R_0^{\alpha_1}(\alpha_1)-x_3^{\alpha_2}(\alpha_2)\sin\alpha_1)\,\mathbf{e}_1-R_0^{\alpha_2}(\alpha_2)\,\mathbf{e}_2+(x_3^{\alpha_1}(\alpha_1)+x_3^{\alpha_2}(\alpha_2)\cos\alpha_1)\,\mathbf{e}_3 \tag{56}$$

Quantities $R_0^{\alpha_1}, x_3^{\alpha_1}$ and $R_0^{\alpha_2}, x_3^{\alpha_2}$ occurring in Eq. (56) read as:

$$\begin{aligned} R_0^{\alpha_1}(\alpha_1)&=a\cos\alpha_1, \quad & x_3^{\alpha_1}(\alpha_1)&=b\sin\alpha_1 \\ R_0^{\alpha_2}(\alpha_2)&=-a\sin\alpha_2, \quad & x_3^{\alpha_2}(\alpha_2)&=b\cos\alpha_2 \end{aligned} \tag{57}$$

being $a=b=1$ m. In this case, the structure is obtained from the superimposition of three layers. In the lower side of the structure, an isotropic sheet of zirconia (53) is applied, whereas the third layer consists of a triclinic material (51). The central thick core is made of FGM, with a volume fraction distribution of the ceramic phase reported in Fig. 4.

Following all procedures presented in Eq. (19) for homogenization purposes of the central porous layer, the dynamic response of the structure is checked for a wide range of porosity parameters, accounting for all dispersions summarized in Table 1. The results for the first eight modes are presented in Figs. 5–8, whereas some numerical results are summarized in Table 5.

In particular, two preliminary validation simulations are considered, accounting for the same structure made of a single dense isotropic constituent in the second layer. The results are compared with success to the outcomes of a refined three-dimensional FEM model, thus validating the higher order model with the zigzag function of Eq. (8). For this reason, all the numerical results presented in Table 5 are referred to the EDZ4 theory.

Referring to the A1 approach (Fig. 5), for all considered modes, the introduction of porosity provides for the structure at issue an increment of its vibration frequencies for both low and high values of $\beta_0^{(2)}$, with a maximum variation, for the case of uniform through-the-thickness

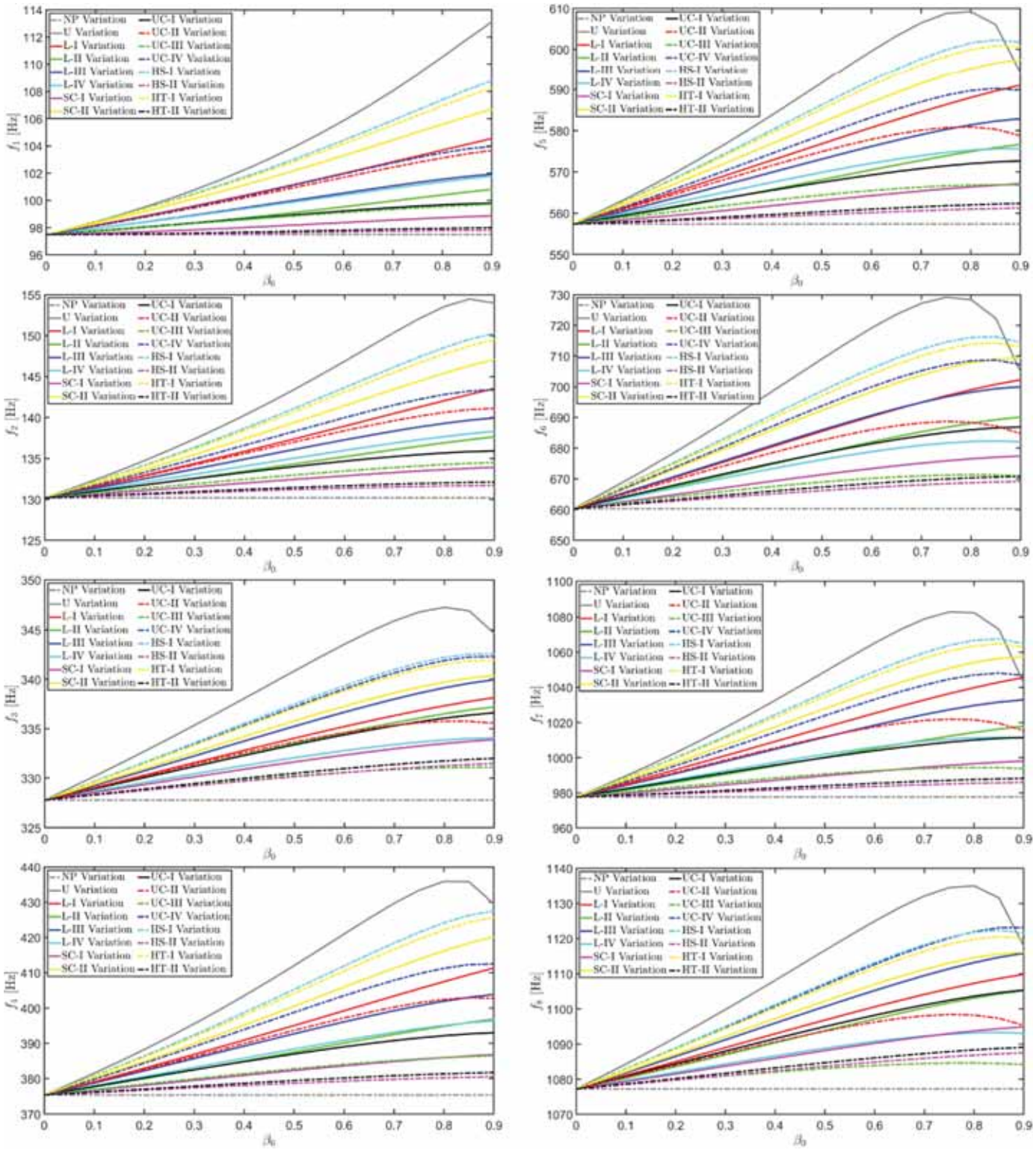


**Fig. 5.** Free vibration analysis of a laminated spherical panel of variable thickness made of isotropic, FGM and generally anisotropic layers characterized by different through-the-thickness distributions of the material porosity. The A1 methodology has been adopted for the computation of the equivalent elastic properties of the porous FGM core.

distribution ($U^{\beta_0^{(2)}}$). All other configurations lead to intermediate results. Generally speaking, in the case of higher modes, a decrease of the curves is observed for higher values of the porosity parameter for some distributions. The Approach 2 (A2) is adopted for plots in Fig. 6. The mode frequencies of the same laminated FGM porous spherical panel are computed with all the through-the-thickness dispersion of Table 1. As stated previously, some distributions may provide negative values of the elastic modulus and material density in some parts of the FGM layer. For this reason, the parametric investigation of Fig. 6 is performed up to $\beta_0^{(2)} = 0.6$. Generally speaking, also in this case the porosity turns into an

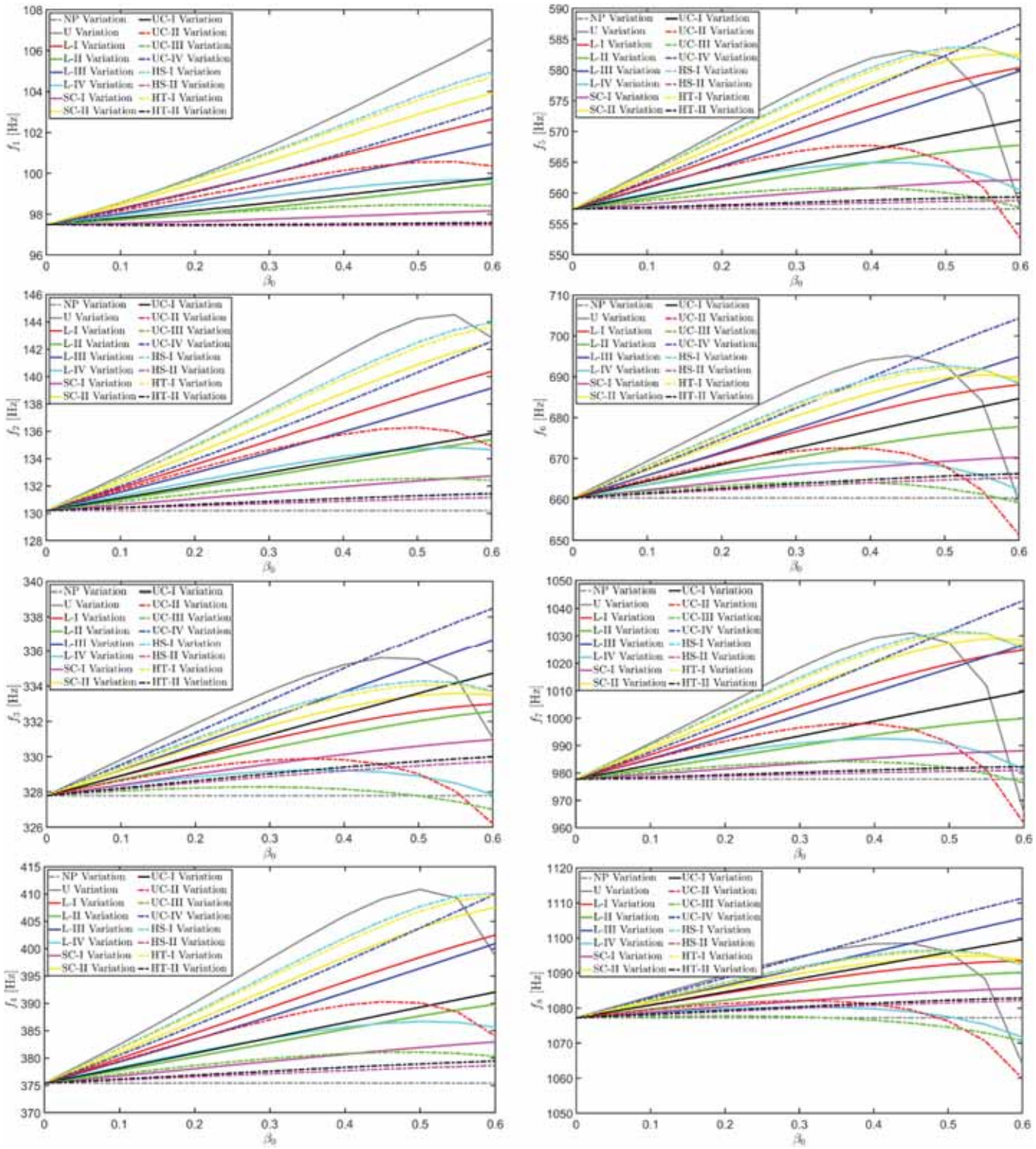


**Fig. 6.** Free vibration analysis of a laminated spherical panel of variable thickness made of isotropic, FGM and generally anisotropic layers characterized by different through-the-thickness distributions of the material porosity. The A2 methodology has been adopted for the computation of the equivalent elastic properties of the porous FGM core.

increment of the natural frequencies of the structure. For lower values of the porosity parameter, a uniform distribution provides the highest frequencies. On the other hand, as $\beta_0^{(2)}$ increases, the maximum values of frequencies are obtained with the UC $-$ IV$^{\beta_0^{(2)}}$ dispersion, accounting for the concentration of voids in the lower part of the layer (Fig. 1). Furthermore, from $\beta_0^{(2)} = 0.5$ on, high frequencies are lower than those ones for dense structures. In Fig. 7 the same parametric investigation by means of the A2 approach is performed for the entire porosity range up to $\beta_0^{(2)} = 0.9$ only for the through-the-thickness distributions accounting for positive homogenized material properties. As can be seen, the

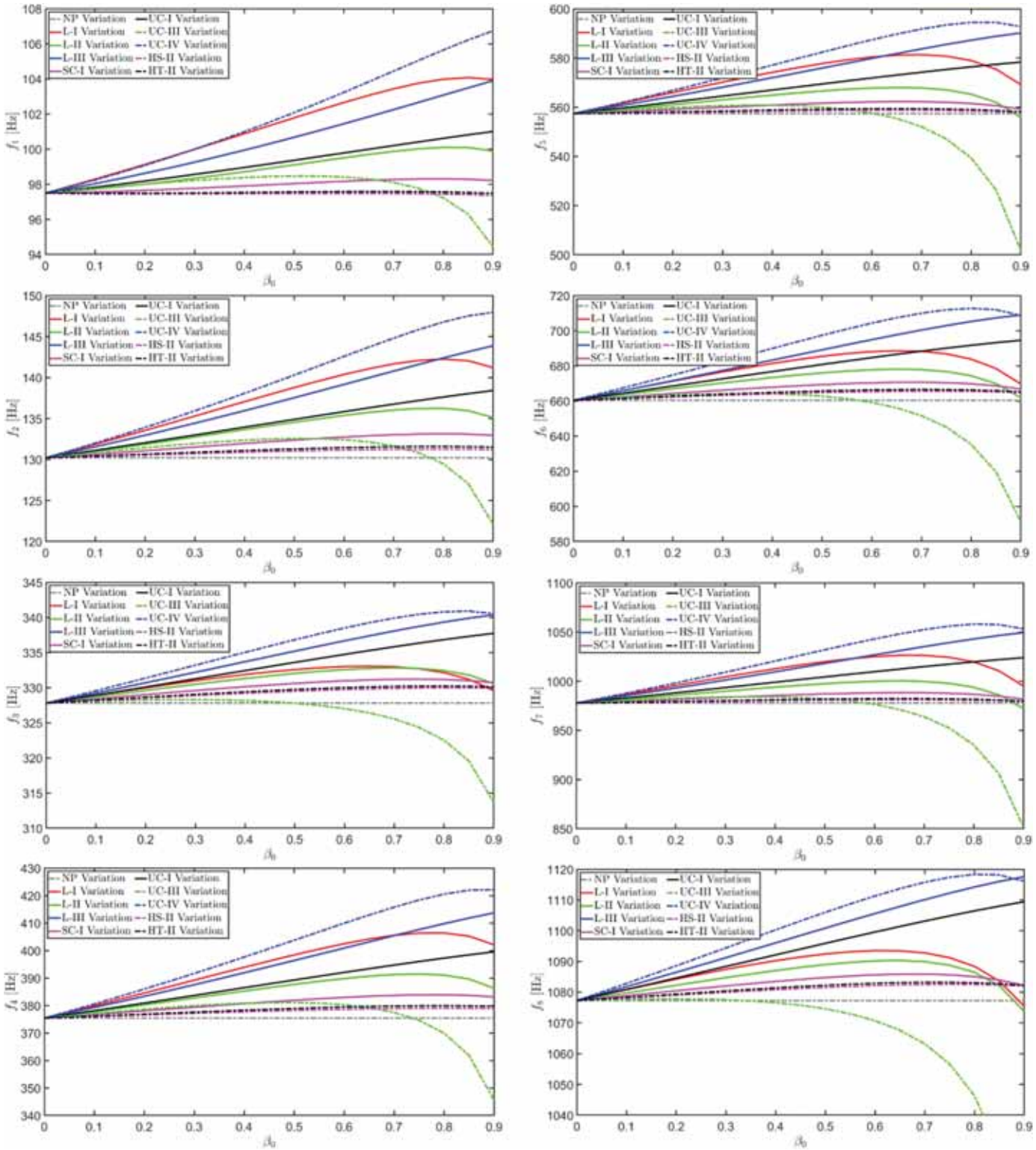


**Fig. 7.** Free vibration analysis of a laminated spherical panel of variable thickness made of isotropic, FGM and generally anisotropic layers characterized by different through-the-thickness distributions of the material porosity. The A2 methodology has been adopted for the computation of the equivalent elastic properties of the porous FGM core.

$UC-III^{\beta_0^{(2)}}$ variation accounts for a reduction of the vibration frequencies as the presence of porosity is significative within the structure.

The approach A3 is adopted to obtain the results provided in Fig. 8 and Table 5. Also, for this case, the results from the sensitivity analysis tell that the uniform porosity distribution leads to the maximum increment of all the first eight natural frequencies of the structure proportional to the value assumed by $\beta_0^{(2)}$. Furthermore, for modes 5–7, the curves assume a maximum value for the eigenvalue near $\beta_0^{(2)} = 0.8$.

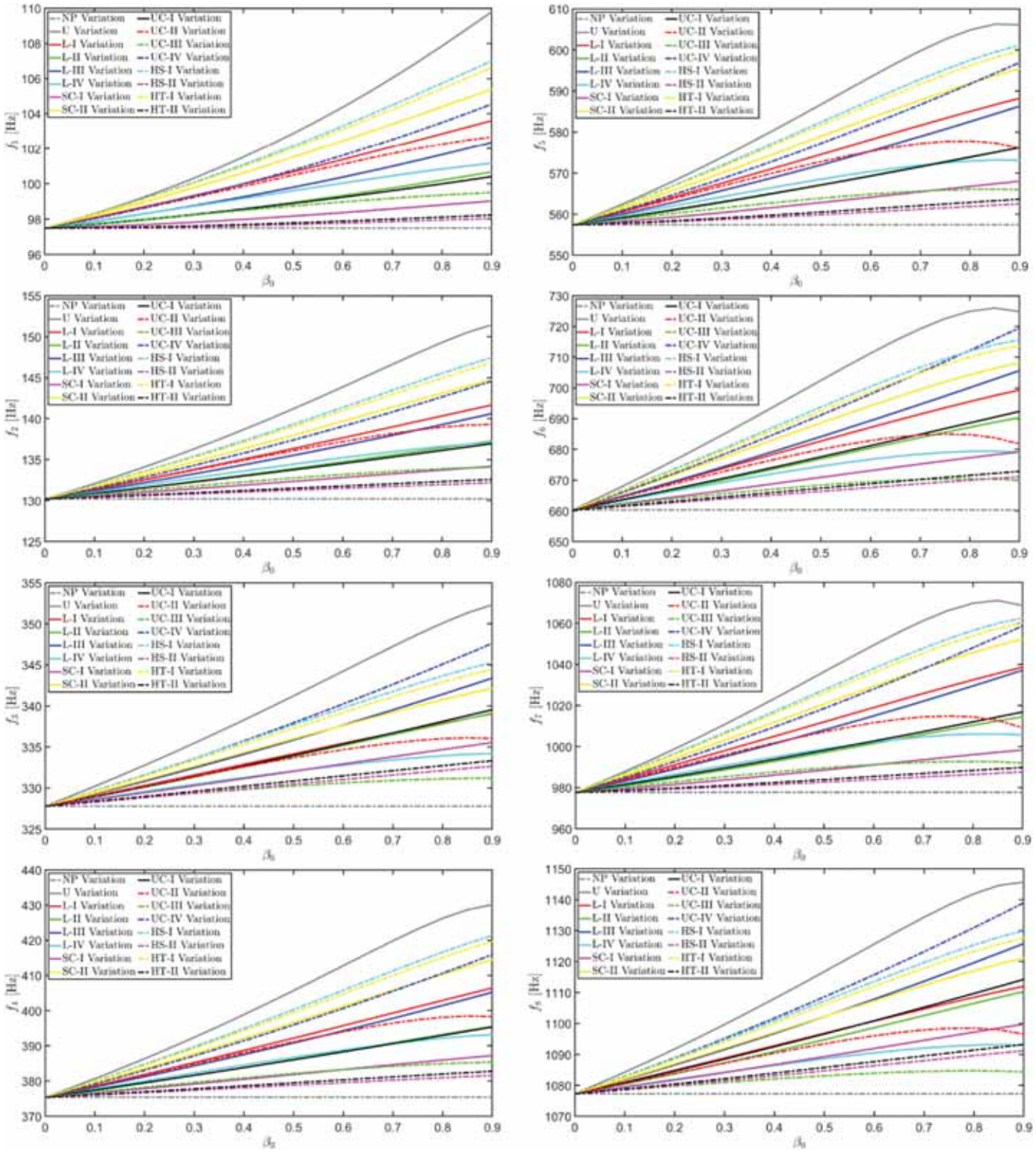


**Fig. 8.** Free vibration analysis of a laminated spherical panel of variable thickness made of isotropic, FGM and generally anisotropic layers characterized by different through-the-thickness distributions of the material porosity. The A3 methodology has been adopted for the computation of the equivalent elastic properties of the porous FGM core.

### *4.3. Arbitrarily-shaped shells with general boundary conditions*

In the present section, the mode frequencies are calculated for laminated doubly-curved shell structures of arbitrary shape, enforced with non-conventional boundary conditions. Different kinds of materials are considered accounting for generally anisotropic layers and orthotropic sheets. Furthermore, the influence of the through-the-thickness porosity distribution in the FGM layers is investigated. A parametric investigation is performed on a revolution hyperbolic hyperboloid, whose geometric features are collected in Fig. 9. The reference surface equation expressed in principal coordinates reads as:

**Table 5**
First ten mode frequencies of a spherical panel (FFCF) made of generally anisotropic and isotropic outer layers, whereas the central core is made of FGM. The sensitivity of the porosity scale parameter, as well as the adopted through-the-thickness distributions, has been checked.

| Mode $f$ [Hz] | | 1 | 2 | 3 | 4 | 5 | 6 | 7 | 8 | 9 | 10 |
|---|---|---|---|---|---|---|---|---|---|---|---|
| $\beta_0 = 0$ | | $p = 0$ | | | | | | | | | |
| 3D FEM | 1838538 DOFs | 94.87 | 122.51 | 329.61 | 352.49 | 538.20 | 637.91 | 932.01 | 1078.30 | 1270.98 | 1285.14 |
| FSDT | 5046 DOFs | 94.72 | 122.98 | 329.86 | 355.30 | 541.41 | 639.52 | 941.96 | 1083.59 | 1276.03 | 1292.71 |
| TSDT | 10092 DOFs | 94.87 | 122.67 | 329.15 | 352.70 | 537.70 | 637.72 | 932.42 | 1077.19 | 1272.68 | 1287.91 |
| EDZ4 | 15138 DOFs | 94.31 | 121.71 | 329.59 | 352.26 | 538.62 | 637.68 | 933.20 | 1078.38 | 1271.43 | 1285.69 |
| $\beta_0 = 0$ | | $p = +\infty$ | | | | | | | | | |
| 3D FEM | 1838538 DOFs | 98.91 | 133.18 | 326.72 | 381.33 | 559.81 | 666.26 | 985.84 | 1074.27 | 1254.03 | 1297.89 |
| FSDT | 5046 DOFs | 102.01 | 138.23 | 332.84 | 390.70 | 570.87 | 685.62 | 999.97 | 1084.32 | 1263.92 | 1327.34 |
| TSDT | 10092 DOFs | 99.64 | 134.15 | 327.57 | 382.56 | 561.56 | 668.48 | 988.32 | 1072.12 | 1254.09 | 1304.29 |
| EDZ4 | 15138 DOFs | 98.51 | 132.67 | 328.15 | 381.50 | 561.53 | 667.87 | 986.05 | 1074.04 | 1253.13 | 1298.84 |
| $\beta_0 = 0$ | | $p = 3$ | | | | | | | | | |
| FSDT | 5046 DOFs | 98.95 | 132.99 | 329.49 | 382.66 | 566.73 | 670.17 | 1001.45 | 1090.56 | 1274.96 | 1317.83 |
| TSDT | 10092 DOFs | 98.69 | 131.92 | 327.78 | 376.73 | 557.39 | 662.51 | 978.80 | 1077.18 | 1264.32 | 1302.89 |
| EDZ4 | 15138 DOFs | 97.49 | 130.20 | 327.79 | 375.41 | 557.40 | 660.33 | 977.73 | 1077.27 | 1261.99 | 1297.05 |
| A3, $\beta_0$ | | Uniform Porosity | | | | | | | | | |
| 0.10 | | 97.88 | 131.11 | 328.98 | 377.98 | 559.85 | 664.08 | 982.68 | 1080.70 | 1265.03 | 1300.88 |
| 0.20 | | 99.24 | 134.08 | 332.76 | 386.31 | 567.89 | 676.05 | 998.88 | 1091.72 | 1274.96 | 1313.54 |
| 0.30 | | 100.30 | 136.28 | 335.46 | 392.39 | 573.81 | 684.57 | 1010.74 | 1099.66 | 1282.24 | 1322.85 |
| 0.40 | | 101.51 | 138.64 | 338.28 | 398.86 | 580.12 | 693.43 | 1023.30 | 1108.03 | 1290.00 | 1332.70 |
| 0.50 | | 102.86 | 141.18 | 341.22 | 405.70 | 586.73 | 702.44 | 1036.34 | 1116.74 | 1298.19 | 1342.82 |
| 0.60 | | 104.37 | 143.86 | 344.23 | 412.79 | 593.43 | 711.27 | 1049.37 | 1125.64 | 1306.68 | 1352.70 |
| 0.70 | | 106.03 | 146.62 | 347.25 | 419.85 | 599.80 | 719.25 | 1061.32 | 1134.34 | 1315.16 | 1361.29 |
| 0.80 | | 107.86 | 149.30 | 350.09 | 426.23 | 604.86 | 724.94 | 1069.80 | 1141.91 | 1322.89 | 1366.41 |
| 0.90 | | 109.80 | 151.46 | 352.31 | 430.11 | 606.09 | 724.82 | 1068.59 | 1145.70 | 1327.68 | 1363.04 |
| $\beta_0$ | | Symmetric Cosine II Porosity | | | | | | | | | |
| 0.10 | | 97.84 | 130.91 | 328.57 | 377.37 | 559.42 | 663.06 | 981.78 | 1079.63 | 1264.25 | 1300.38 |
| 0.20 | | 98.96 | 133.13 | 330.99 | 383.48 | 565.69 | 671.45 | 994.34 | 1086.93 | 1271.33 | 1310.79 |
| 0.30 | | 99.77 | 134.69 | 332.64 | 387.74 | 570.02 | 677.15 | 1002.99 | 1091.96 | 1276.27 | 1318.02 |
| 0.40 | | 100.62 | 136.30 | 334.30 | 392.13 | 574.46 | 682.89 | 1011.81 | 1097.09 | 1281.34 | 1325.39 |
| 0.50 | | 101.51 | 137.96 | 335.97 | 396.63 | 578.94 | 688.61 | 1020.68 | 1102.25 | 1286.50 | 1332.79 |
| 0.60 | | 102.44 | 139.67 | 337.63 | 401.20 | 583.42 | 694.19 | 1029.47 | 1107.37 | 1291.67 | 1340.05 |
| 0.70 | | 103.40 | 141.39 | 339.24 | 405.79 | 587.78 | 699.50 | 1037.95 | 1112.36 | 1296.76 | 1346.93 |
| 0.80 | | 104.40 | 143.11 | 340.76 | 410.29 | 591.88 | 704.28 | 1045.76 | 1117.05 | 1301.63 | 1353.05 |
| 0.90 | | 105.40 | 144.77 | 342.13 | 414.54 | 595.45 | 708.18 | 1052.29 | 1121.17 | 1306.02 | 1357.82 |
| $\beta_0$ | | Unsymmetric Cosine IV Porosity | | | | | | | | | |
| 0.10 | | 97.75 | 130.83 | 328.70 | 377.25 | 559.13 | 663.14 | 981.33 | 1080.06 | 1264.14 | 1299.29 |
| 0.20 | | 98.62 | 132.84 | 331.58 | 383.05 | 564.65 | 671.95 | 992.76 | 1088.88 | 1271.14 | 1306.84 |
| 0.30 | | 99.28 | 134.28 | 333.61 | 387.15 | 568.62 | 678.13 | 1000.92 | 1095.14 | 1276.29 | 1312.57 |
| 0.40 | | 99.99 | 135.79 | 335.73 | 391.45 | 572.81 | 684.53 | 1009.52 | 1101.71 | 1281.83 | 1318.87 |
| 0.50 | | 100.77 | 137.38 | 337.94 | 395.95 | 577.22 | 691.17 | 1018.55 | 1108.57 | 1287.76 | 1325.74 |
| 0.60 | | 101.61 | 139.05 | 340.24 | 400.65 | 581.85 | 698.01 | 1028.01 | 1115.74 | 1294.11 | 1333.18 |
| 0.70 | | 102.52 | 140.81 | 342.62 | 405.54 | 586.69 | 705.04 | 1037.89 | 1123.21 | 1300.86 | 1341.17 |
| 0.80 | | 103.49 | 142.65 | 345.08 | 410.64 | 591.73 | 712.22 | 1048.16 | 1130.97 | 1308.03 | 1349.71 |
| 0.90 | | 104.55 | 144.58 | 347.61 | 415.91 | 596.94 | 719.50 | 1058.76 | 1139.00 | 1315.63 | 1358.73 |
| $\beta_0$ | | Hyperbolic Sine I Porosity | | | | | | | | | |
| 0.10 | | 97.88 | 131.01 | 328.72 | 377.66 | 559.68 | 663.49 | 982.32 | 1080.04 | 1264.60 | 1300.78 |
| 0.20 | | 99.15 | 133.57 | 331.61 | 384.74 | 566.85 | 673.30 | 996.71 | 1088.70 | 1272.88 | 1312.60 |
| 0.30 | | 100.08 | 135.39 | 333.60 | 389.73 | 571.89 | 680.05 | 1006.77 | 1094.74 | 1278.74 | 1320.93 |
| 0.40 | | 101.08 | 137.30 | 335.64 | 394.93 | 577.09 | 686.90 | 1017.11 | 1100.95 | 1284.81 | 1329.49 |
| 0.50 | | 102.15 | 139.30 | 337.70 | 400.30 | 582.39 | 693.74 | 1027.60 | 1107.26 | 1291.05 | 1338.14 |
| 0.60 | | 103.29 | 141.35 | 339.76 | 405.79 | 587.70 | 700.41 | 1037.98 | 1113.57 | 1297.36 | 1346.60 |
| 0.70 | | 104.49 | 143.45 | 341.77 | 411.30 | 592.84 | 706.65 | 1047.87 | 1119.70 | 1303.60 | 1354.46 |
| 0.80 | | 105.74 | 145.52 | 343.65 | 416.61 | 597.50 | 712.00 | 1056.53 | 1125.37 | 1309.49 | 1361.00 |
| 0.90 | | 107.00 | 147.46 | 345.30 | 421.35 | 601.12 | 715.66 | 1062.63 | 1130.02 | 1314.57 | 1364.98 |
| $\beta_0$ | | Hyperbolic Tangent I Porosity | | | | | | | | | |
| 0.10 | | 97.93 | 131.12 | 328.69 | 377.97 | 559.94 | 663.81 | 982.96 | 1080.02 | 1264.46 | 1301.11 |
| 0.20 | | 99.37 | 134.06 | 331.45 | 386.08 | 567.96 | 674.66 | 999.44 | 1088.52 | 1272.24 | 1314.03 |
| 0.30 | | 100.44 | 136.16 | 333.33 | 391.85 | 573.60 | 682.12 | 1011.01 | 1094.37 | 1277.67 | 1323.16 |
| 0.40 | | 101.59 | 138.39 | 335.21 | 397.89 | 579.40 | 689.67 | 1022.89 | 1100.26 | 1283.20 | 1332.53 |
| 0.50 | | 102.83 | 140.72 | 337.06 | 404.14 | 585.26 | 697.10 | 1034.84 | 1106.07 | 1288.75 | 1341.86 |
| 0.60 | | 104.15 | 143.12 | 338.80 | 410.49 | 590.97 | 704.10 | 1046.37 | 1111.60 | 1294.13 | 1350.64 |
| 0.70 | | 105.54 | 145.52 | 340.36 | 416.69 | 596.13 | 710.07 | 1056.56 | 1116.45 | 1299.00 | 1357.91 |
| 0.80 | | 106.95 | 147.77 | 341.53 | 422.18 | 599.94 | 713.86 | 1063.53 | 1119.85 | 1302.68 | 1361.84 |
| 0.90 | | 108.27 | 149.48 | 341.94 | 425.69 | 600.59 | 713.02 | 1062.99 | 1120.03 | 1303.59 | 1358.60 |

$$\mathbf{r}(\alpha_1, \alpha_2) = a \cosh \alpha_1 \cos \alpha_2 \, \mathbf{e}_1 - a \cosh \alpha_1 \sin \alpha_2 \, \mathbf{e}_2 + c \sinh \alpha_1 \, \mathbf{e}_3 \tag{58}$$

with $a = 1.00$ m and $a = 1.50$ m. In this case, a shell structure with negative curvature is selected, enforced with non-conventional boundary conditions modelled with the Double Weibull distribution of Eq. (27). In this way, the panel is fixed at the four corners of the physical domain. The lamination scheme accounts for a central triclinic layer with general orientation and two external parts made of functionally graded porous material. The volume fractions distribution is selected for both layers so that a pure ceramic material is present at the interface level. Furthermore, a generalized isogeometric mapping is applied to the structure, according to the distortion outlined in Eq. 13. The edges of the structure are described in an efficient way by means of NURBS curves

**Revolution Hyperbolic Hyperboloid**

$$\mathbf{r}(\alpha_1,\alpha_2) = a\cosh\alpha_1\cos\alpha_2\,\mathbf{e}_1 - a\cosh\alpha_1\sin\alpha_2\,\mathbf{e}_2 + c\sinh\alpha_1\,\mathbf{e}_3$$

$a = 1.00\,\text{m},\quad c = 1.50\,\text{m}$

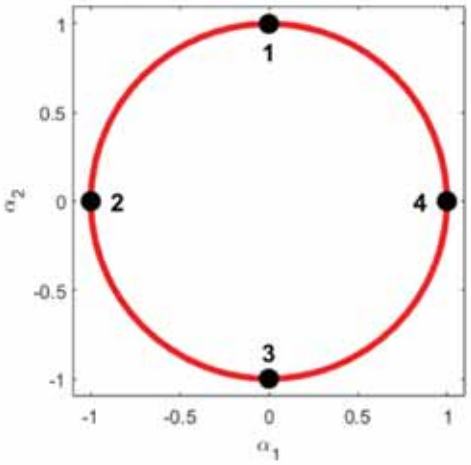


**3D FEM Model**

**2D GDQ Model**

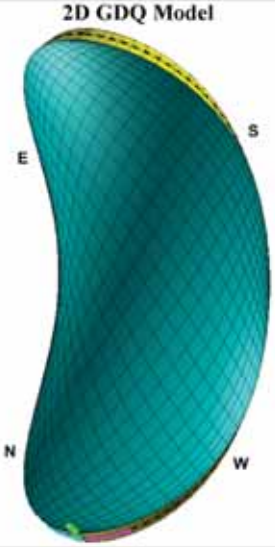


**Edge 1-2**

knots → 0.0, 0.0, 0.0, 0.0, 0.2, 0.4, 0.6, 0.8, 1.0, 1.0, 1.0, 1.0

weigths → 1.0,1.0,1.0,1.0,1.0,1.0,1.0,1.0,1.0

control points → (0.000000, 0.999553),(-0.104756, 0.999553), (-0.314269, 0.967222),(-0.597024, 0.821733), (-0.822768, 0.597776),(-0.966005, 0.313874), (-1.000000, 0.104625),(-1.000000, 0.000000)

**Edge 2-3**

knots → 0.0, 0.0, 0.0, 0.0, 0.2, 0.4, 0.6, 0.8, 1.0, 1.0, 1.0, 1.0

weigths → 1.0,1.0,1.0,1.0,1.0,1.0,1.0,1.0,1.0

control points → (-1.000000, 0.000000),(-1.000000, -0.104625), (-0.966005, -0.313874),(-0.822768, -0.597776), (-0.597024, -0.821733),(-0.314269, -0.967222), (-0.104756, -0.999553),(-0.000000, -0.999553)

**Edge 3-4**

knots → 0.0, 0.0, 0.0, 0.0, 0.2, 0.4, 0.6, 0.8, 1.0, 1.0, 1.0, 1.0

weigths → 1.0,1.0,1.0,1.0,1.0,1.0,1.0,1.0,1.0

control points → (-0.000000, -0.999553),(0.104756, -0.999553), (0.314269, -0.967222),(0.597024, -0.821733), (0.822768, -0.597776),(0.966005, -0.313874), (1.000000, -0.104625),(1.000000, 0.000000)

**Edge 4-1**

knots → 0.0, 0.0, 0.0, 0.0, 0.2, 0.4, 0.6, 0.8, 1.0, 1.0, 1.0, 1.0

weigths → 1.0,1.0,1.0,1.0,1.0,1.0,1.0,1.0,1.0

control points → (1.000000, 0.000000),(1.000000, 0.104625), (0.966005, 0.313874),(0.822768, 0.597776), (0.597024, 0.821733),(0.314269, 0.967222), (0.104756, 0.999553),(0.000000, 0.999553)

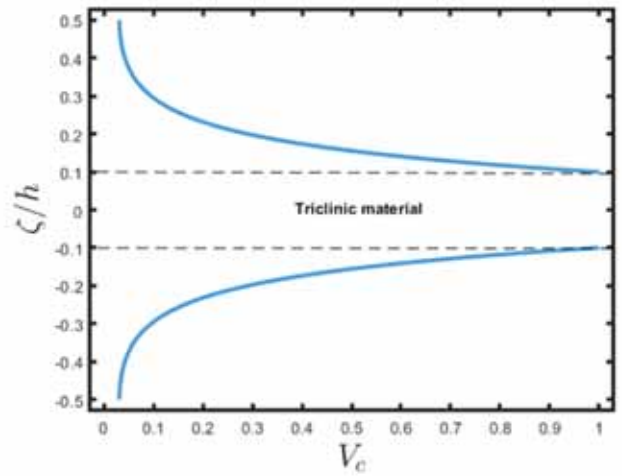


**Geometric Inputs:** $h_1 = h_3 = 0.06$ m, $h_2 = 0.03$ m

**Lamination Scheme:**

$$\left(\text{FGM}^{C\{\text{A24-IV}\,/\,\beta_c\}}_{M\,(a=1/b=0.5/c=2/d=1/p=5)}\;/\,30\,/\,\text{FGM}^{M\{\text{A24-III}\,/\,\beta_c\}}_{C\,(a=1/b=0.5/c=2/d=1/p=5)}\right)$$

2nd layer: triclinic material

**Fig. 9.** Geometric and mechanical properties of a revolution hyperbolic hyperboloid of arbitrary shape characterized by two outer FGM layers and a central core of triclinic material.

**Table 6**
First ten mode frequencies of a revolution hyperbolic hyperboloid of arbitrary shape ($B^{K}_{DDD}B^{K}_{DDD}B^{K}_{DDD}B^{K}_{DDD}$) made of two outer porous FGM layers and a central triclinic core enforced with general boundary conditions. The sensitivity of the porosity parameter on the dynamic structural response has been checked employing higher order theories.

| Mode $f$ [Hz] | 1 | 2 | 3 | 4 | 5 | 6 | 7 | 8 | 9 | 10 |
|---|---|---|---|---|---|---|---|---|---|---|
| $\beta_0 = 0.00$ | 86.15 | 114.37 | 118.73 | 173.50 | 203.35 | 264.04 | 282.63 | 287.54 | 336.66 | 338.99 |
| $\beta_0 = 0.05$ | 85.04 | 113.52 | 117.49 | 172.29 | 200.87 | 259.84 | 280.29 | 284.28 | 333.74 | 337.49 |
| $\beta_0 = 0.10$ | 83.86 | 112.52 | 116.15 | 170.86 | 198.21 | 255.40 | 277.56 | 280.78 | 330.47 | 335.63 |
| $\beta_0 = 0.15$ | 82.58 | 111.40 | 114.71 | 169.24 | 195.35 | 250.70 | 274.51 | 277.03 | 326.89 | 333.46 |
| $\beta_0 = 0.20$ | 81.21 | 110.16 | 113.15 | 167.44 | 192.28 | 245.72 | 271.14 | 272.98 | 323.00 | 330.99 |
| $\beta_0 = 0.25$ | 79.72 | 108.80 | 111.45 | 165.44 | 188.95 | 240.40 | 267.45 | 268.62 | 318.81 | 328.23 |
| $\beta_0 = 0.30$ | 78.10 | 107.31 | 109.61 | 163.24 | 185.35 | 234.73 | 263.43 | 263.89 | 314.29 | 325.15 |
| $\beta_0 = 0.35$ | 76.34 | 105.67 | 107.61 | 160.80 | 181.43 | 228.63 | 258.75 | 259.04 | 309.42 | 321.74 |
| $\beta_0 = 0.40$ | 74.41 | 103.87 | 105.42 | 158.10 | 177.13 | 222.05 | 253.15 | 254.24 | 304.16 | 317.94 |
| $\beta_0 = 0.45$ | 72.28 | 101.88 | 103.01 | 155.09 | 172.41 | 214.91 | 247.00 | 248.97 | 298.46 | 313.71 |
| $\beta_0 = 0.50$ | 69.92 | 99.66 | 100.35 | 151.70 | 167.16 | 207.12 | 240.23 | 243.16 | 292.25 | 308.95 |
| $\beta_0 = 0.55$ | 67.30 | 97.18 | 97.39 | 147.86 | 161.30 | 198.55 | 232.74 | 236.69 | 285.44 | 303.58 |
| $\beta_0 = 0.60$ | 64.35 | 94.08 | 94.36 | 143.44 | 154.69 | 189.04 | 224.38 | 229.46 | 277.88 | 297.46 |
| $\beta_0 = 0.65$ | 61.00 | 90.34 | 91.10 | 138.25 | 147.12 | 178.36 | 214.96 | 221.26 | 269.34 | 290.36 |
| $\beta_0 = 0.70$ | 57.24 | 85.14 | 86.78 | 132.34 | 139.09 | 166.83 | 207.36 | 212.94 | 258.71 | 282.61 |
| $\beta_0 = 0.75$ | 53.95 | 85.49 | 95.88 | 124.73 | 156.67 | 170.40 | 170.40 | 196.34 | 202.37 | 253.63 |
| $\beta_0 = 0.80$ | 47.31 | 75.28 | 77.23 | 115.12 | 116.02 | 135.87 | 177.69 | 188.81 | 234.54 | 260.40 |
| $\beta_0 = 0.85$ | 40.48 | 67.75 | 69.28 | 100.22 | 101.98 | 115.21 | 159.85 | 172.37 | 214.92 | 233.44 |
| $\beta_0 = 0.90$ | 30.81 | 55.81 | 56.97 | 78.54 | 82.11 | 87.30 | 135.44 | 145.29 | 184.49 | 192.20 |

Lamination Scheme: $(\mathrm{FGM}_{M\ (a=1/b=0.5/c=2/d=1/p=5)}^{C\ (\mathrm{A2-L-IV}\ /\beta_0)}\ /30/\mathrm{FGM}_{C\ (a=1/b=0.5/c=2/d=1/p=5)}^{M\ (\mathrm{A2-L-III}\ /\beta_0)})$
2nd layer: triclinic material
$h_1 = h_3 = 0.06$ m, $h_2 = 0.03$ m
**Boundary Springs**: Double - Weibull distribution ($\bar{\xi}_m = 0.0025$, $\widetilde{\xi}_m = 0.0025$, $p = 20$), $\bar{\lambda} = 1$
$k_{1f}^{(k)\xi^0{}_1} = k_{1f}^{(k)\xi^1{}_1} = k_{1f}^{(k)\xi^0{}_2} = k_{1f}^{(k)\xi^1{}_2} = 1 \times 10^{21}$ N/m$^3$, $k_{2f}^{(k)\xi^0{}_1} = k_{2f}^{(k)\xi^1{}_1} = k_{2f}^{(k)\xi^0{}_2} = k_{2f}^{(k)\xi^1{}_2} = 1 \times 10^{21}$ N/m$^3$, $k_{3f}^{(k)\xi^0{}_1} = k_{3f}^{(k)\xi^1{}_1} = k_{3f}^{(k)\xi^0{}_2} = k_{3f}^{(k)\xi^1{}_2} = 1 \times 10^{21}$ N/m$^3$

(41) starting from a pre-determined set of knots, weights and control points. Following the A2 relation of Eq. (19), the first ten mode frequencies are calculated employing the EDZ4 displacement field assumption within Eq. (7) for different values of the porosity scale factors $\beta_0^{(1)}$ and $\beta_0^{(3)}$. In particular, it is shown that the introduction of porosity within the model, provides a meaningful reduction of the natural frequencies of the structure for all considered modes, as can be seen from results in Table 6. Moreover, in Fig. 10 we check for the sensitivity of the panel at issue with respect to porosity, also for the mode shapes. Even though the first mode deflection seems to be unaffected by porosity, for other vibrations the structural deflection changes its configuration since new waves are observed for increased value of parameters $\beta_0^{(1)}$ and $\beta_0^{(3)}$.

The same boundary conditions are applied to another doubly-curved structure. In Fig. 11 a helicoid of arbitrary shape is presented, accounting for a distortion of the physical domain characterized by two straight edges and two curved sides. The reference surface equation of the panel is reported in the following, setting $a = 0.60$ m:

$$\mathbf{r}(\alpha_1,\alpha_2) = -a\cos(\alpha_1+\alpha_2)\sinh(\alpha_1-\alpha_2)\mathbf{e}_1 - a\sin(\alpha_1+\alpha_2)\sinh(\alpha_1-\alpha_2)\,\mathbf{e}_2 + a(\alpha_1-\alpha_2)\,\mathbf{e}_3 \tag{59}$$

The lamination scheme is inverted with respect to the previous example, since this time the triclinic material is assigned to the two outer layers, whereas the central part consists of a functionally graded porous material. The numerical investigations on the structure at issue are reported in Table 7. A three-dimensional FEM solution has been calculated with a commercial package in the case of isotropic central core without the presence of any porosity distribution accounting for zirconia and aluminum, respectively. Furthermore, the first ten mode frequencies are calculated with the classical FSDT approach and EDZ4 higher order theory, with a very good agreement between the 3D FEM solution and the EDZ4-based one. In addition, a LW simulation according to the formulation of Ref. [26] for generally anisotropic materials is presented. For the complete explanation of the nomenclature adopted, the interested reader can refer to [26]. After that, the LD4 solution is reported as reference prediction for the same structure, accounting for a FGM material of zirconia and aluminum characterized by various through-the-thickness distributions, setting $\beta_0^{(2)} = 0.5$. In particular, the porosity expressions $\mathrm{SC-I}^{\beta_0^{(2)}}$, $\mathrm{SC-II}^{\beta_0^{(2)}}$, $\mathrm{UC-III}^{\beta_0^{(2)}}$ and $\mathrm{UC-IV}^{\beta_0^{(2)}}$ are considered, taking into account the A2 approach. Then, the formulation presented in the manuscript is adopted for the evaluation of the natural frequencies employing classical FSDT and TSDT approaches, as well as higher order displacement field assumptions. As can be seen, the results from the LD4 theory can be predicted with a good level of accuracy with the present ESL model, if an EDZ4 displacement field assumption is considered. In this way, a reduced number of DOFs are required. The best results are obtained only for higher order theories, since a variation of the material properties along the thickness of the shell, induces some through-the-thickness stretching phenomena in each mode, which cannot be predicted with a constant out-of-plane field variable assumption. In Fig. 12, the first nine mode shapes of the helicoid calculated with the EDZ4 theory are provided, accounting for the presence of a $\mathrm{UC-II}^{\beta_0^{(2)}}$ porosity distribution with $\beta_0^{(2)} = 0.5$. It can be seen that the higher order displacement field assumption allows one to predict not only the pure bending behavior of the structure, but also other deformation effects that cannot be seen when classical theories are adopted.

The last numerical simulation refers to a laminated doubly-curved catenoidal panel, whose reference surface is expressed employing principal coordinates according to the following expression:

$$\mathbf{r}(\alpha_1,\alpha_2) = a\cosh\left(\frac{\alpha_1}{a}\right)\cos\alpha_2\ \mathbf{e}_1 - a\cosh\left(\frac{\alpha_1}{a}\right)\sin\alpha_2\ \mathbf{e}_2 + a\sinh\alpha_1\ \mathbf{e}_3 \tag{60}$$

where $a = 1.50$ m. All information regarding the physical domain mapping can be found in Fig. 13. Accordingly, a distortion is performed characterized by four curved shell edges of alternate curvature, accurately described by means of NURBS curves (41). The first layer consists in a triclinic layer, whereas the second one accounts for an FGM porous

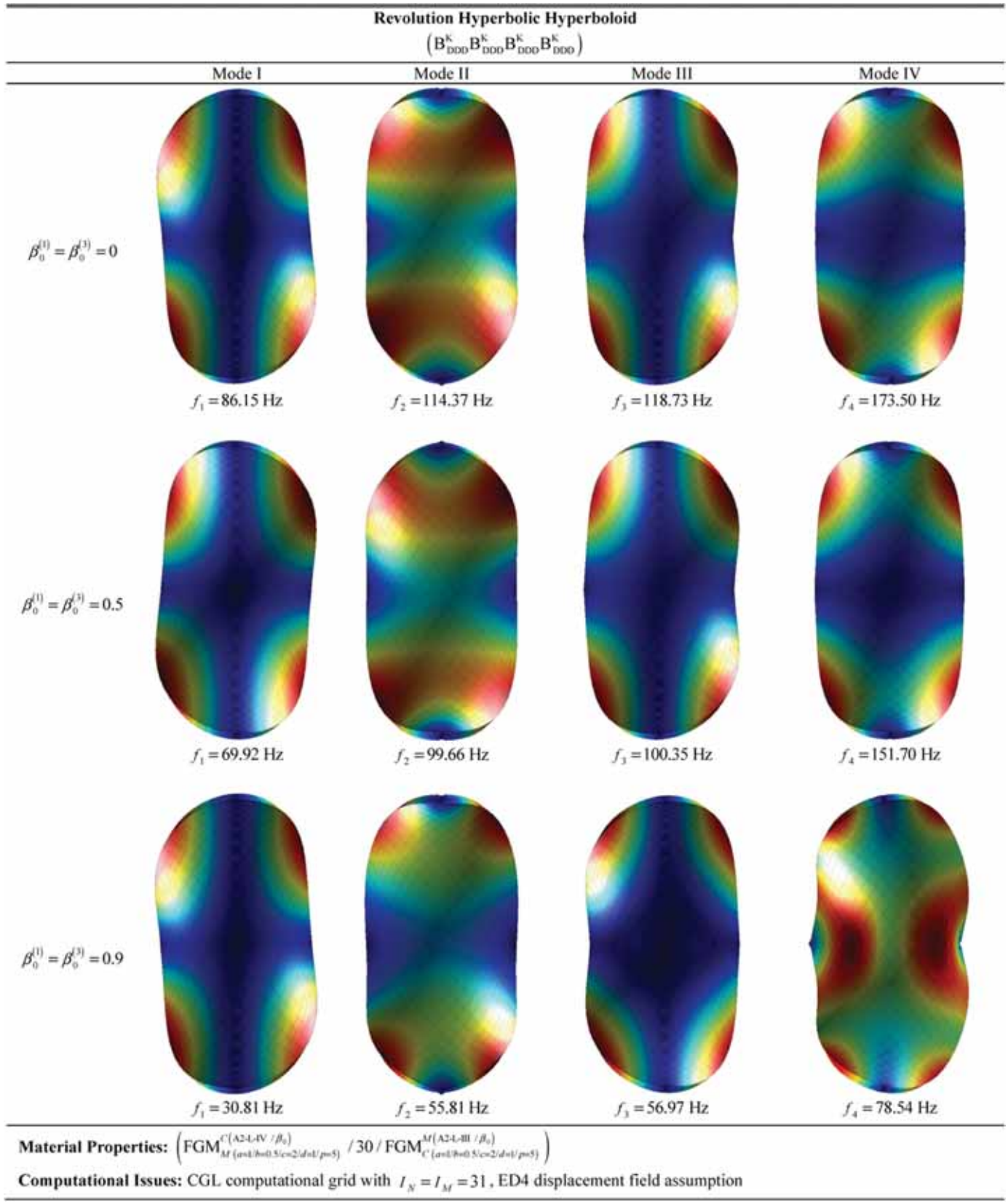


**Fig. 10.** Comparison of the first four mode shapes of a revolution hyperbolic hyperboloid enforced with non-conventional boundary conditions made of FGM with different values of the porosity parameter $\beta_0$.

**Helicoid**

$$\mathbf{r}(\alpha_1,\alpha_2) = -a\cos(\alpha_1+\alpha_2)\sinh(\alpha_1-\alpha_2)\mathbf{e}_1 - a\sin(\alpha_1+\alpha_2)\sinh(\alpha_1-\alpha_2)\mathbf{e}_2 + a(\alpha_1-\alpha_2)\mathbf{e}_3$$

$a = 0.60$ m

3D FEM Model

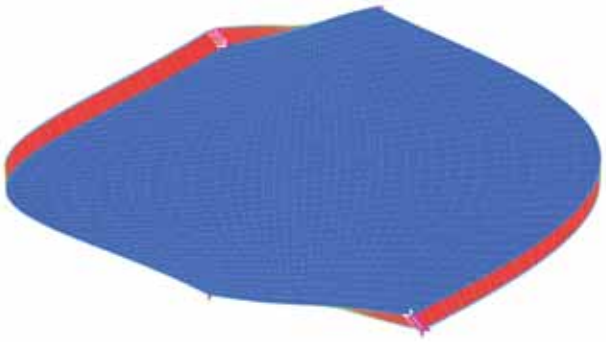

2D GDQ Model

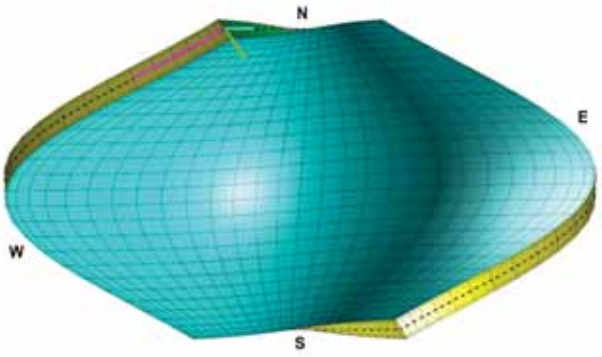


Isogeometric mapping of the physical domain

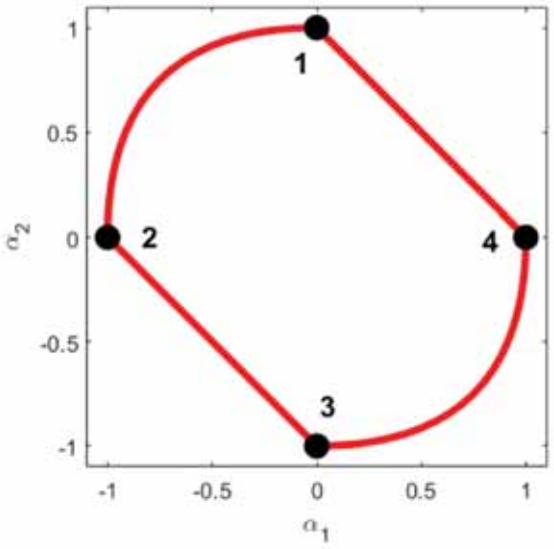


**Edge 1-2**

knots → 0.0,0.0,0.0,1.0,1.0,1.0

weigths → 1.0,1.0,1.0

control points → (0.000000, 1.000000),(-1.000000, 1.000000), (-1.000000, 0.000000)

**Edge 2-3**

knots → 0.0,0.0,1.0,1.0

weigths → 1.0,1.0

control points → (-1.000000, 0.000000),(0.000000, -1.000000)

**Edge 3-4**

knots → 0.0,0.0,0.0,1.0,1.0,1.0

weigths → 1.0,1.0,1.0

control points → (0.000000, -1.000000),(1.000000, -1.000000), (1.000000, 0.000000)

**Edge 4-1**

knots → 0.0,0.0,1.0,1.0

weigths → 1.0,1.0

control points → (1.000000, 0.000000),(0.000000, 1.000000)

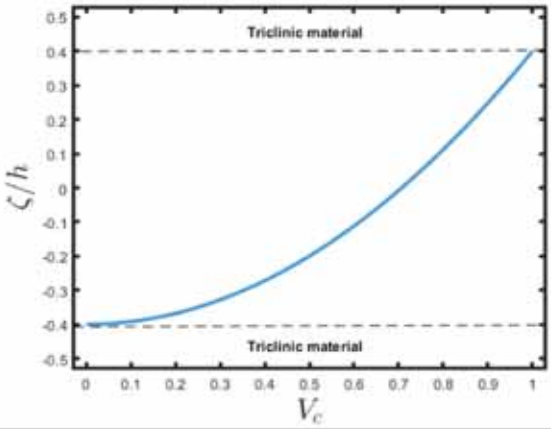


**Geometric Inputs:** $h_1 = h_3 = 0.01$ m, $h_2 = 0.08$ m

**Material Properties:** $\left(30/\mathrm{FGM}^{C(\mathrm{A2}/\beta_0=0.5)}_{M(a=1/h=0/c=1/d=1/p=0.5)}/45\right)$

1st layer: triclinic material, 3rd layer: triclinic material

**Fig. 11.** Geometric and mechanical properties of a helicoid of arbitrary shape characterized by an FGM core and different kinds of porosity through-the-thickness distribution. The physical domain has been described employing a curvilinear set of principal coordinates, whereas a generalized NURBS-based blending functions is adopted for the mapping.

**Table 7**
First ten mode frequencies of a helicoid of arbitrary shape ($B^{K}_{DDD}B^{K}_{DDD}B^{K}_{DDD}B^{K}_{DDD}$) made of two outer triclinic layers and a central FGM porous core made of ceramic and metallic material enforced with general boundary conditions. The sensitivity of the adopted higher order field variable expansion has been checked for different material configurations and porosity distributions.

| **Mode** $f$ [Hz] (30/Zirc/45) | DOFs | 1 | 2 | 3 | 4 | 5 | 6 | 7 | 8 | 9 | 10 |
|---|---|---|---|---|---|---|---|---|---|---|---|
| 3D FEM | 213891 | 48.84 | 89.37 | 192.76 | 193.73 | 273.54 | 308.29 | 356.54 | 362.23 | 374.82 | 481.65 |
| LD4 | 37845 | 51.24 | 91.08 | 192.13 | 194.73 | 275.55 | 310.36 | 363.53 | 366.63 | 376.97 | 471.70 |
| FSDT | 5046 | 50.85 | 90.37 | 190.39 | 193.49 | 274.46 | 309.43 | 361.17 | 362.94 | 373.84 | 465.64 |
| EDZ4 | 15138 | 51.19 | 91.04 | 191.95 | 195.18 | 275.08 | 310.70 | 363.31 | 366.10 | 375.67 | 471.86 |
| (30/Alu/45) | | | | | | | | | | | |
| 3D FEM | 213891 | 46.74 | 82.41 | 178.10 | 184.50 | 248.52 | 291.20 | 316.72 | 340.60 | 350.90 | 427.97 |
| LD4 | 37845 | 48.73 | 83.80 | 177.30 | 185.42 | 250.33 | 293.39 | 323.64 | 344.93 | 351.97 | 418.49 |
| FSDT | 5046 | 48.46 | 83.15 | 175.76 | 184.17 | 249.35 | 292.26 | 321.57 | 341.55 | 349.01 | 413.12 |
| EDZ4 | 15138 | 48.79 | 83.81 | 177.35 | 185.80 | 250.09 | 293.66 | 323.49 | 344.74 | 351.23 | 418.83 |
| $(30/FGM_M^{C\ (A2-SC-I\ /\ \beta_0=0.5)\ (a=1/b=0/c=1/d=1/p=0.5)}/45)$ | | | | | | | | | | | |
| LD4 | 37845 | 48.17 | 85.78 | 178.10 | 181.58 | 262.48 | 285.25 | 344.44 | 346.72 | 357.04 | 446.88 |
| FSDT | 5046 | 47.49 | 85.06 | 177.51 | 179.12 | 259.99 | 284.85 | 338.83 | 344.25 | 350.21 | 442.64 |
| TSDT | 10092 | 47.65 | 85.37 | 178.31 | 179.58 | 260.26 | 285.24 | 341.04 | 344.76 | 351.20 | 442.99 |
| ED1 | 5046 | 47.47 | 84.52 | 177.27 | 178.14 | 257.46 | 284.23 | 338.49 | 340.73 | 349.15 | 437.96 |
| ED2 | 5769 | 47.88 | 85.81 | 180.45 | 180.94 | 261.39 | 288.80 | 341.67 | 346.76 | 352.76 | 449.39 |
| EDZ2 | 10092 | 47.76 | 85.63 | 180.27 | 180.56 | 260.67 | 288.59 | 340.98 | 345.99 | 351.85 | 448.19 |
| ED3 | 10092 | 48.00 | 86.13 | 181.31 | 181.59 | 261.43 | 289.31 | 344.24 | 347.26 | 353.60 | 449.69 |
| EDZ3 | 12615 | 47.96 | 85.99 | 181.06 | 181.44 | 260.82 | 289.08 | 344.04 | 346.46 | 353.17 | 448.46 |
| ED4 | 12615 | 47.91 | 85.91 | 180.29 | 180.99 | 261.25 | 287.73 | 343.22 | 347.17 | 353.08 | 449.14 |
| EDZ4 | 15138 | 47.80 | 85.76 | 180.28 | 180.59 | 260.36 | 287.55 | 342.80 | 346.27 | 352.08 | 447.89 |
| $(30/FGM_M^{C\ (A2-SC-II\ /\ \beta_0=0.5)\ (a=1/b=0/c=1/d=1/p=0.5)}/45)$ | | | | | | | | | | | |
| LD4 | 37845 | 51.86 | 89.53 | 188.92 | 194.65 | 268.04 | 309.16 | 347.99 | 367.40 | 374.57 | 445.92 |
| FSDT | 5046 | 51.80 | 89.11 | 188.29 | 193.77 | 267.91 | 308.64 | 347.28 | 365.72 | 373.84 | 443.60 |
| TSDT | 10092 | 51.84 | 89.24 | 188.41 | 194.09 | 267.91 | 308.58 | 347.27 | 366.54 | 373.95 | 443.38 |
| ED1 | 5046 | 51.78 | 88.73 | 187.64 | 193.60 | 266.25 | 308.06 | 344.80 | 365.43 | 372.95 | 440.31 |
| ED2 | 5769 | 52.14 | 89.84 | 189.86 | 196.13 | 269.53 | 311.75 | 349.50 | 368.00 | 376.22 | 448.87 |
| EDZ2 | 10092 | 52.01 | 89.53 | 189.26 | 195.83 | 268.49 | 311.27 | 348.37 | 366.88 | 374.98 | 447.19 |
| ED3 | 10092 | 52.13 | 89.78 | 189.73 | 196.81 | 268.45 | 311.62 | 348.47 | 369.42 | 375.76 | 446.90 |
| EDZ3 | 12615 | 52.12 | 89.76 | 189.69 | 196.77 | 268.41 | 311.58 | 348.41 | 369.31 | 375.69 | 446.85 |
| ED4 | 12615 | 52.01 | 89.57 | 189.26 | 194.95 | 268.32 | 309.42 | 348.17 | 367.84 | 374.97 | 446.39 |
| EDZ4 | 15138 | 52.04 | 89.58 | 189.28 | 194.86 | 268.46 | 309.36 | 348.14 | 367.83 | 375.14 | 446.24 |
| $(30/FGM_M^{C\ (A2-UC-I\ /\ \beta_0=0.5)\ (a=1/b=0/c=1/d=1/p=0.5)}/45)$ | | | | | | | | | | | |
| LD4 | 37845 | 50.25 | 88.20 | 186.48 | 186.94 | 267.04 | 298.52 | 350.02 | 358.22 | 368.68 | 450.12 |
| FSDT | 5046 | 49.75 | 87.48 | 184.43 | 186.11 | 265.25 | 297.88 | 347.92 | 353.42 | 363.62 | 446.20 |
| TSDT | 10092 | 49.88 | 87.75 | 184.85 | 186.83 | 265.47 | 298.19 | 348.29 | 355.41 | 364.44 | 446.38 |
| ED1 | 5046 | 49.72 | 86.96 | 183.54 | 185.80 | 262.96 | 297.11 | 344.63 | 353.02 | 362.52 | 441.80 |
| ED2 | 5769 | 50.12 | 88.21 | 186.17 | 188.77 | 266.63 | 301.32 | 350.24 | 356.16 | 366.11 | 452.32 |
| EDZ2 | 10092 | 50.00 | 87.99 | 185.71 | 188.54 | 265.87 | 300.99 | 349.38 | 355.36 | 365.14 | 450.99 |
| ED3 | 10092 | 50.21 | 88.44 | 186.51 | 189.73 | 266.47 | 301.68 | 350.35 | 358.47 | 366.65 | 452.02 |
| EDZ3 | 12615 | 50.17 | 88.35 | 186.32 | 189.43 | 266.16 | 301.24 | 349.96 | 358.16 | 366.31 | 451.44 |
| ED4 | 12615 | 50.12 | 88.23 | 186.11 | 188.48 | 266.24 | 300.17 | 350.18 | 357.41 | 366.12 | 451.48 |
| EDZ4 | 15138 | 50.03 | 88.12 | 185.83 | 188.22 | 265.72 | 299.72 | 349.69 | 356.92 | 365.35 | 450.81 |
| $(30/FGM_M^{C\ (A2-UC-II\ /\ \beta_0=\ 0.5)\ (a=1/b=0/c=1/d=1/p=0.5)}/45)$ | | | | | | | | | | | |
| LD4 | 37845 | 48.80 | 86.09 | 181.43 | 182.39 | 260.86 | 291.08 | 343.45 | 348.03 | 358.10 | 441.38 |
| FSDT | 5046 | 48.54 | 85.65 | 180.31 | 181.71 | 259.83 | 290.64 | 342.05 | 345.18 | 355.24 | 438.57 |
| TSDT | 10092 | 48.62 | 85.84 | 180.62 | 182.15 | 259.93 | 290.77 | 342.24 | 346.54 | 355.70 | 438.57 |
| ED1 | 5046 | 48.51 | 85.23 | 179.67 | 181.24 | 258.00 | 289.85 | 339.35 | 344.78 | 354.30 | 434.92 |
| ED2 | 5769 | 48.90 | 86.37 | 182.10 | 184.40 | 261.40 | 294.51 | 344.25 | 347.44 | 357.51 | 444.10 |
| EDZ2 | 10092 | 48.75 | 86.07 | 181.48 | 184.05 | 260.30 | 293.98 | 343.04 | 346.37 | 356.23 | 442.36 |
| ED3 | 10092 | 48.95 | 86.50 | 182.26 | 185.31 | 260.73 | 294.74 | 343.83 | 349.68 | 357.77 | 443.10 |
| EDZ3 | 12615 | 48.93 | 86.45 | 182.18 | 185.25 | 260.59 | 294.66 | 343.65 | 349.59 | 357.65 | 442.84 |
| ED4 | 12615 | 48.81 | 86.21 | 181.64 | 183.34 | 260.49 | 292.21 | 343.57 | 348.00 | 356.88 | 442.37 |
| EDZ4 | 15138 | 48.80 | 86.16 | 181.54 | 183.18 | 260.37 | 292.00 | 343.34 | 347.87 | 356.74 | 441.94 |

Lamination Scheme:
1st layer: triclinic material, 2nd layer: FGM material, 3rd layer: triclinic material, $h_1 = h_3 = 0.01$ m, $h_2 = 0.08$ m
**Boundary Springs**: Double - Weibull distribution ($\overline{\xi}_m = 0.0025$, $\widetilde{\xi}_m = 0.0025$, $p = 20$), $\overline{\lambda} = 1$,
$k_{1f}^{(k)\xi^0{}_1} = k_{1f}^{(k)\xi^1{}_1} = k_{1f}^{(k)\xi^0{}_2} = k_{1f}^{(k)\xi^1{}_2} = 1 \times 10^{21}$ N/m$^3$, $k_{2f}^{(k)\xi^0{}_1} = k_{2f}^{(k)\xi^1{}_1} = k_{2f}^{(k)\xi^0{}_2} = k_{2f}^{(k)\xi^1{}_2} = 1 \times 10^{21}$ N/m$^3$, $k_{3f}^{(k)\xi^0{}_1} = k_{3f}^{(k)\xi^1{}_1} = k_{3f}^{(k)\xi^0{}_2} = k_{3f}^{(k)\xi^1{}_2} = 1 \times 10^{21}$ N/m$^3$

material. At the upper side of the structure, an orthotropic lamina of graphite-epoxy (52) is considered, characterized by a general distribution of the material angle, according to Eq. (16).

The doubly-curved panel is constrained with general boundary conditions, accounting for the Super Elliptic distribution of Eq. (26).

The higher order model is validated in Table 8 with respect to the first ten natural frequencies of the structure, accounting for a dense isotropic zirconia and aluminum (53) in the central core of the structure. A three-dimensional FEM model is developed for the derivation of a reference solution. Furthermore, the results coming from the FSDT, TSDT and EDZ4 theories are provided. For the sake of completeness, the LD4 solution has been calculated. After that, higher order theories is adopted for the evaluation of the vibration modes. A continuous smooth variation with $p^{(2)} = 0.5$ is considered for the volume fraction of the FGM material associated to the central core, and some non-linear

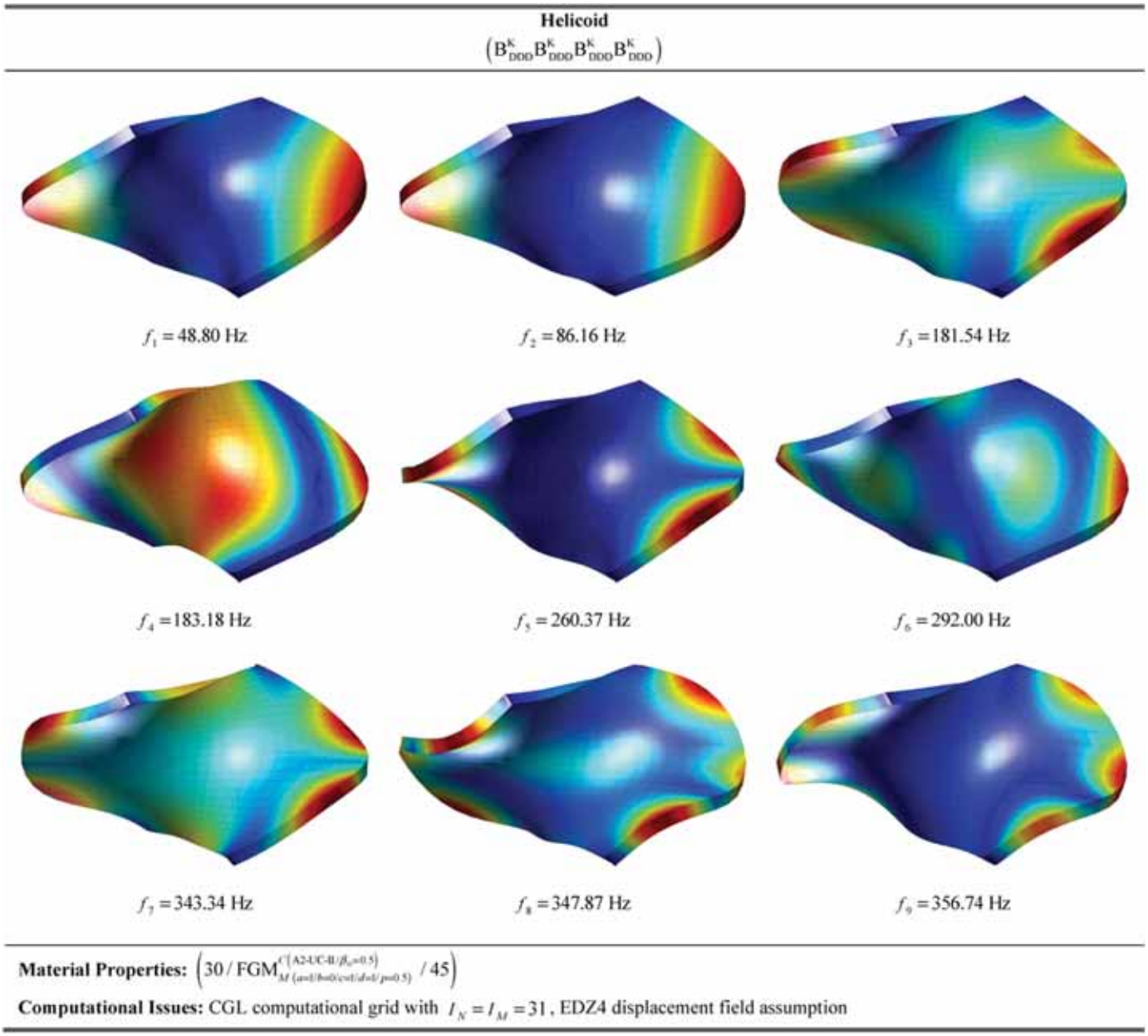


**Fig. 12.** First nine mode shapes of a mapped helicoid made of two external triclinic layers and a central FGM porous core constrained at its four corners. They have been calculated with the EDZ4 higher order theory.

symmetric and unsymmetric porosity through-the-thickness distributions are adopted. For each considered case, the introduction of a zigzag function in Eq. (8) influences the outcomes of the simulations. Furthermore, as the order of the displacement field assumption increases, the solution converges to the LW numerical predictions. It can be seen that the EDZ4 theory, despite its ESL nature, is capable of well predicting the quasi-three-dimensional response of the laminated panel at issue coming from a high computationally demanding LW simulation, thus employing a reduced number of DOFs. In Fig. 14 the first nine mode shapes of the mapped catenoid are represented, accounting for a $\mathrm{HS} - \mathrm{I}^{\beta^{(2)}_0}$ porosity distribution along the thickness of the shell. As can be seen in this figure, the employment of the EDZ4 theory predicts both the bending response and coupling issues occurring at the interlaminar stage.

## 5. Conclusions

In the present manuscript, an efficient two-dimensional formulation based on higher order theories has been presented for the dynamic analysis of laminated doubly-curved shells with porous FGM layers. Following the ESL approach, the unified formulation has been used and a general formulation has been developed employing curvilinear principal coordinates and a numerical solution has been derived through the GDQ algorithm. Furthermore, a generalized isogeometric mapping has been applied to investigate arbitrarily shaped domains. FGM layers have been described with the rule of mixture, and three different approaches have been adopted for the computation of the equivalent elastic properties. Unlike previous papers on this research topic, this work addresses the vibrational response of doubly-curved shell structures with an arbitrary distribution of the material porosity within the FGM layer, along with anisotropic materials with a continuous variation of the material orientation angle. After different validating analyses, we have

**Catenoid**

$$\mathbf{r}(\alpha_1,\alpha_2)=a\cosh\left(\frac{\alpha_1}{a}\right)\cos\alpha_2\ \mathbf{e}_1-a\cosh\left(\frac{\alpha_1}{a}\right)\sin\alpha_2\ \mathbf{e}_2+a\sinh\alpha_1\ \mathbf{e}_3,\quad a=1.50\ \text{m}$$

3D FEM Model | 2D GDQ Model | Isogeometric mapping of the physical domain

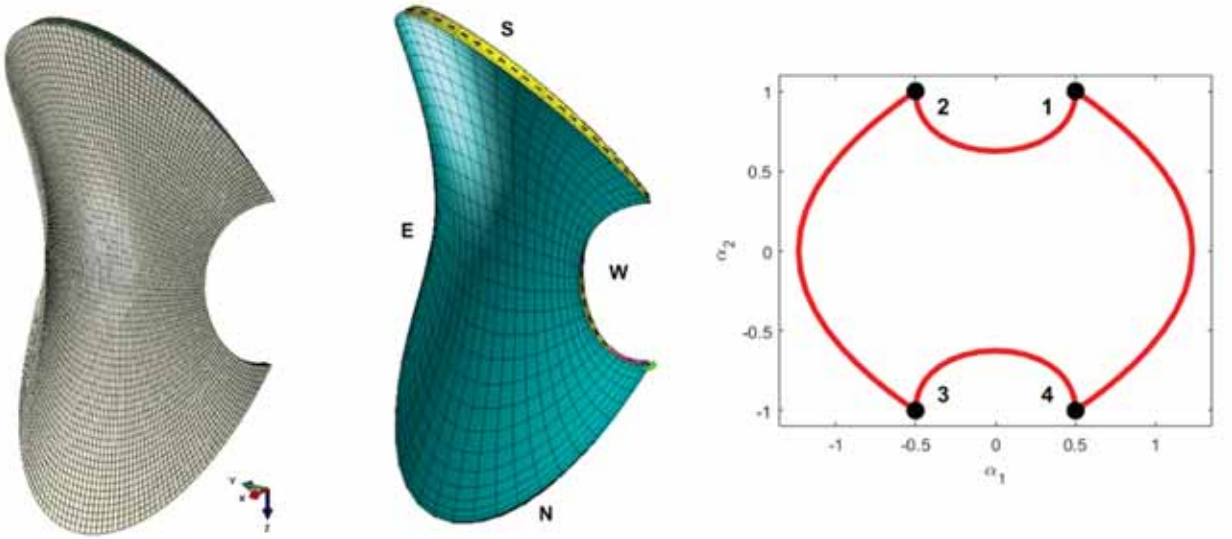


**Edge 1-2**

knots → 0.0,0.0,0.0,0.0,0.0,1.0,1.0,1.0,1.0,1.0

weigths → 1.0,1.0,1.0,1.0,1.0

control points → (0.500000,1.000000),(0.500000,0.500000),(-0.500000,0.500000),(-0.500000,1.000000)

**Edge 2-3**

knots → 0.0,0.0,0.0,0.0,1.0,1.0,1.0,1.0

weigths → 1.0,1.0,1.0,1.0

control points → (-0.500000,1.000000),(-1.963495,0.000000),(-0.500000,-1.000000)

**Edge 3-4**

knots → 0.0,0.0,0.0,0.0,0.0,1.0,1.0,1.0,1.0,1.0

weigths → 1.0,1.0,1.0,1.0,1.0

control points → (-0.500000,-1.000000),(-0.500000,-0.500000),(0.500000,-0.500000),(0.500000,-1.000000)

**Edge 4-1**

knots → 0.0,0.0,0.0,0.0,1.0,1.0,1.0,1.0

weigths → 1.0,1.0,1.0,1.0

control points → (0.500000,-1.000000),(1.963495,0.000000),(0.500000,1.000000)

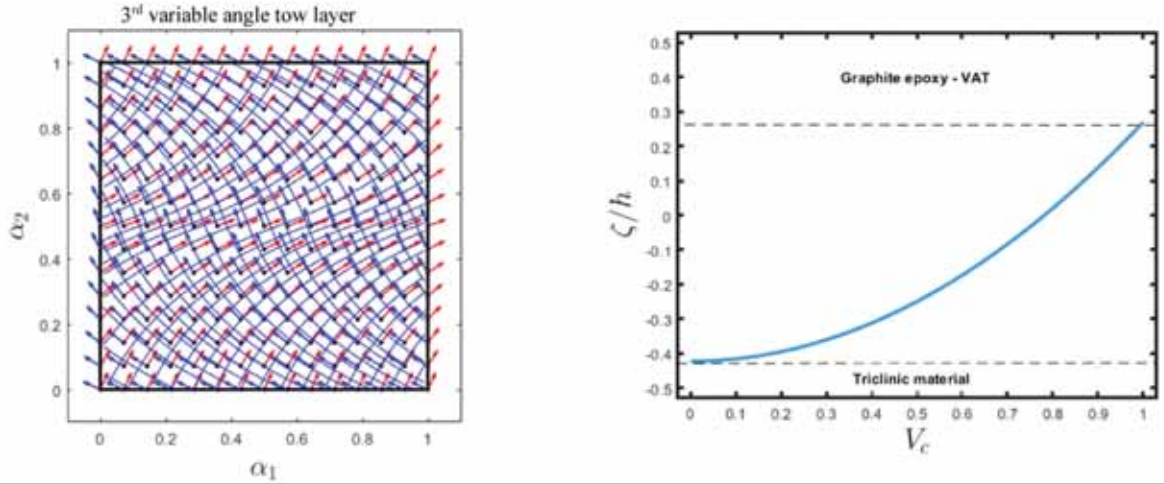


**Geometric Inputs:** $h_1=0.01$ m, $h_2=0.09$ m, $h_3=0.03$ m

**Material Properties:** $\left(30/\text{FGM}^{C[A1/\beta_c=0.5]}_{M\{a=0,b=0,c=1,d=0,p=0.5\}}/20\left\langle(0|45)^1_{\alpha_2}\right\rangle\right)$, 1st layer: triclinic material, 3rd layer: graphite-epoxy

**Fig. 13.** Geometric and mechanical properties of a helicoid of arbitrary shape characterized by an FGM core and different kinds of porosity through-the-thickness distribution. The physical domain has been described employing a curvilinear set of principal coordinates, whereas a generalized NURBS-based blending functions is adopted for the mapping.

**Table 8**
First ten mode frequencies of a catenoid of arbitrary shape ($B^{K}_{SSS}FB^{K}_{SSS}F$) made of a central FGM porous core made of ceramic and metallic material, a triclinic layer and an orthotropic external sheet enforced with general boundary conditions. The sensitivity of the adopted higher order field variable expansion has been checked for different material configurations and porosity distributions.

| Mode $f$ [Hz] | DOFs | 1 | 2 | 3 | 4 | 5 | 6 | 7 | 8 | 9 | 10 |
|---|---|---|---|---|---|---|---|---|---|---|---|
| (30/Zirc/20) | | | | | | | | | | | |
| 3D FEM | 213891 | 35.64 | 41.56 | 87.55 | 98.46 | 138.59 | 138.78 | 202.81 | 205.20 | 221.38 | 227.28 |
| FSDT | 5046 | 33.82 | 42.00 | 86.68 | 98.27 | 134.41 | 141.24 | 198.90 | 204.96 | 212.38 | 229.77 |
| EDZ4 | 15138 | 33.36 | 43.27 | 86.78 | 98.20 | 135.31 | 140.40 | 198.51 | 205.33 | 213.76 | 230.23 |
| LD4 | 37845 | 32.61 | 43.78 | 86.81 | 98.20 | 134.72 | 140.22 | 198.09 | 204.68 | 213.44 | 229.32 |
| (30/Alu/20) | | | | | | | | | | | |
| 3D FEM | 213891 | 34.55 | 40.39 | 81.97 | 93.34 | 134.78 | 136.72 | 199.30 | 200.56 | 211.53 | 216.36 |
| FSDT | 5046 | 32.58 | 41.02 | 81.10 | 93.14 | 131.44 | 137.18 | 193.44 | 199.77 | 203.17 | 219.33 |
| EDZ4 | 15138 | 32.38 | 41.91 | 81.24 | 93.06 | 132.16 | 136.62 | 193.43 | 199.94 | 204.41 | 219.91 |
| LD4 | 37845 | 31.56 | 42.29 | 81.23 | 92.99 | 131.66 | 136.53 | 192.80 | 199.33 | 204.04 | 219.01 |
| $(30/FGM_M^{C\ (A2-HS-I\ /\ \beta_0=0.5)}{}_{(a=1/b=0/c=1/d=1/p=0.5)}\ /20\langle(0|45)^1_{\alpha_2}\rangle)$ | | | | | | | | | | | |
| LD4 | 37845 | 33.34 | 43.39 | 85.42 | 93.50 | 135.52 | 138.79 | 203.89 | 210.30 | 210.30 | 225.79 |
| FSDT | 5046 | 33.84 | 44.01 | 85.46 | 93.43 | 136.52 | 140.53 | 205.15 | 212.43 | 212.43 | 226.87 |
| TSDT | 10092 | 33.82 | 44.54 | 85.45 | 93.44 | 137.59 | 139.25 | 204.84 | 212.77 | 212.77 | 227.12 |
| ED2 | 5769 | 33.99 | 43.98 | 85.96 | 93.87 | 136.68 | 141.60 | 206.18 | 212.95 | 213.68 | 228.41 |
| EDZ2 | 10092 | 33.87 | 43.98 | 85.71 | 93.63 | 136.37 | 140.87 | 205.68 | 212.76 | 212.76 | 227.64 |
| ED3 | 10092 | 34.05 | 43.96 | 85.85 | 93.66 | 136.74 | 141.31 | 206.12 | 213.39 | 213.39 | 228.23 |
| EDZ3 | 12615 | 32.68 | 45.98 | 85.88 | 93.23 | 138.74 | 139.87 | 205.50 | 211.86 | 215.98 | 227.52 |
| ED4 | 12615 | 34.01 | 43.70 | 85.58 | 93.52 | 136.47 | 140.71 | 205.75 | 212.46 | 212.89 | 227.53 |
| EDZ4 | 15138 | 35.27 | 40.54 | 85.47 | 93.68 | 134.56 | 142.02 | 206.59 | 209.36 | 214.70 | 227.77 |
| $(30/FGM_M^{C\ (A2-HS-II\ /\ \beta_0=0.5)}{}_{(a=1/b=0/c=1/d=1/p=0.5)}\ /20\langle(0|45)^1_{\alpha_2}\rangle)$ | | | | | | | | | | | |
| LD4 | 37845 | 31.38 | 41.25 | 83.43 | 92.73 | 130.12 | 134.51 | 196.82 | 201.59 | 205.28 | 221.82 |
| FSDT | 5046 | 26.83 | 47.12 | 81.72 | 91.50 | 129.64 | 131.01 | 192.46 | 199.29 | 202.87 | 220.02 |
| TSDT | 10092 | 27.16 | 46.75 | 81.71 | 91.59 | 129.48 | 130.99 | 192.67 | 199.36 | 202.58 | 220.64 |
| ED2 | 5769 | 31.05 | 41.19 | 82.15 | 91.84 | 128.16 | 132.45 | 194.18 | 198.85 | 203.76 | 220.27 |
| EDZ2 | 10092 | 31.33 | 40.74 | 82.00 | 91.74 | 128.03 | 132.00 | 193.96 | 198.51 | 203.41 | 219.92 |
| ED3 | 10092 | 31.34 | 40.96 | 82.19 | 91.87 | 128.47 | 132.43 | 194.63 | 199.31 | 203.94 | 220.58 |
| EDZ3 | 12615 | 31.46 | 40.68 | 82.05 | 91.78 | 128.29 | 132.08 | 194.33 | 199.05 | 203.56 | 220.26 |
| ED4 | 12615 | 32.71 | 38.84 | 82.06 | 91.83 | 128.74 | 131.63 | 194.44 | 199.01 | 203.51 | 220.64 |
| EDZ4 | 15138 | 31.58 | 40.41 | 81.99 | 91.73 | 128.24 | 131.99 | 194.22 | 198.88 | 203.42 | 220.17 |
| $(30/FGM_M^{C\ (A2-UC-III\ /\ \beta_0=0.5)}{}_{(a=1/b=0/c=1/d=1/p=0.5)}\ /20\langle(0|45)^1_{\alpha_2}\rangle)$ | | | | | | | | | | | |
| LD4 | 37845 | 32.00 | 41.10 | 84.03 | 93.34 | 129.46 | 134.19 | 196.78 | 201.98 | 205.68 | 222.21 |
| FSDT | 5046 | 31.52 | 42.10 | 82.83 | 92.41 | 128.93 | 132.37 | 194.61 | 200.49 | 204.90 | 221.04 |
| TSDT | 10092 | 31.85 | 41.69 | 82.80 | 92.41 | 129.33 | 131.95 | 194.89 | 200.55 | 205.04 | 221.44 |
| ED2 | 5769 | 31.96 | 41.30 | 83.27 | 92.71 | 128.96 | 133.33 | 195.77 | 200.96 | 205.30 | 222.26 |
| EDZ2 | 10092 | 32.35 | 40.53 | 83.02 | 92.52 | 128.68 | 132.58 | 195.35 | 200.41 | 204.59 | 221.63 |
| ED3 | 10092 | 32.32 | 40.92 | 83.31 | 92.72 | 129.24 | 133.26 | 196.15 | 201.37 | 205.47 | 222.57 |
| EDZ3 | 12615 | 32.40 | 40.56 | 83.01 | 92.54 | 128.90 | 132.62 | 195.69 | 200.78 | 204.69 | 221.79 |
| ED4 | 12615 | 34.06 | 37.51 | 83.22 | 92.74 | 129.39 | 132.31 | 195.55 | 201.18 | 204.58 | 222.79 |
| EDZ4 | 15138 | 32.87 | 39.61 | 82.97 | 92.52 | 128.85 | 132.41 | 195.65 | 200.53 | 204.35 | 221.80 |
| $(30/FGM_M^{C\ (A2-UC-IV\ /\ \beta_0=0.5)}{}_{(a=1/b=0/c=1/d=1/p=0.5)}\ /20\langle(0|45)^1_{\alpha_2}\rangle)$ | | | | | | | | | | | |
| LD4 | 37845 | 33.07 | 42.17 | 84.01 | 92.61 | 135.32 | 139.05 | 204.06 | 207.12 | 210.54 | 224.01 |
| FSDT | 5046 | 32.22 | 43.35 | 83.14 | 91.86 | 134.38 | 137.56 | 202.24 | 206.76 | 207.81 | 223.08 |
| TSDT | 10092 | 35.36 | 39.81 | 83.08 | 106.52 | 106.52 | 143.01 | 200.10 | 207.14 | 207.14 | 221.34 |
| ED2 | 5769 | 32.69 | 42.69 | 83.57 | 92.19 | 134.05 | 138.56 | 203.15 | 206.51 | 209.56 | 223.96 |
| EDZ2 | 10092 | 30.97 | 45.08 | 83.39 | 91.83 | 134.57 | 138.03 | 202.02 | 208.25 | 208.25 | 223.70 |
| ED3 | 10092 | 32.68 | 42.91 | 83.55 | 92.12 | 134.27 | 138.45 | 203.39 | 206.97 | 209.69 | 224.03 |
| EDZ3 | 12615 | 32.88 | 42.46 | 83.50 | 92.10 | 134.10 | 138.35 | 203.45 | 206.54 | 209.64 | 223.86 |
| ED4 | 12615 | 32.24 | 43.31 | 83.30 | 91.93 | 134.23 | 138.04 | 203.05 | 206.49 | 208.93 | 223.46 |
| EDZ4 | 15138 | 32.91 | 42.11 | 83.30 | 91.96 | 133.96 | 138.05 | 203.22 | 205.81 | 209.19 | 223.37 |

Lamination Scheme:
1st layer: triclinic material, 2nd layer: FGM material, 3rd layer: graphite-epoxy, $h_1 = 0.01$ m, $h_2 = 0.09$ m, $h_2 = 0.03$ m
**Boundary Springs**: Super Elliptic distribution, West (W) edge: ($\overline{\xi}_m = 0$, $\widetilde{\xi}_m = 0.53$, $p = 1000$), East (E) edge: ($\overline{\xi}_m = 1$, $\widetilde{\xi}_m = 0.47$, $p = 1000$)
$k^{(k)\xi^0{}_2}_{1f} = k^{(k)\xi^1{}_2}_{1f} = 1 \times 10^{21}$ N/m$^3$, $k^{(k)\xi^0{}_2}_{2f} = k^{(k)\xi^1{}_2}_{2f} = 1 \times 10^{21}$ N/m$^3$, $k^{(k)\xi^0{}_2}_{3f} = k^{(k)\xi^1{}_2}_{3f} = 1 \times 10^{21}$ N/m$^3$, $\overline{\lambda} = 1$

checked for the sensitivity of the dynamic response of the structure on the FGM distribution. Furthermore, the presence of generally anisotropic layers in the stacking sequence has been investigated, together with the presence of curvature. The three-dimensional capability of the results is outlined with respect to three-dimensional simulations and experimental evidence.

It is shown that the presence of material porosity can affect the vibrational response of shell structures. When the porosity through-the-thickness distribution accounts for a concentration of voids at the center of the lamina, a reduction of the natural frequency is seen, while an increase is found in the case of porous layers with a minimum presence of voids in the middle thickness. Finally, when a porous FGM lamina is embedded in a more general lamination scheme, an intermediate frequency is obtained between the corresponding ones related to two extreme configurations of the stacking sequence which employs only one constituent, as expected. On the other hand, in the case of a rapid variation of the volume fraction the frequency of the FGM shell may be higher than that of the same structure with isotropic homogeneous layers.

The proposed model has revealed to be an efficient strategy for the structural analysis of structures with double curvature characterized by laminated porous FGM layers, taking into account different kinds of

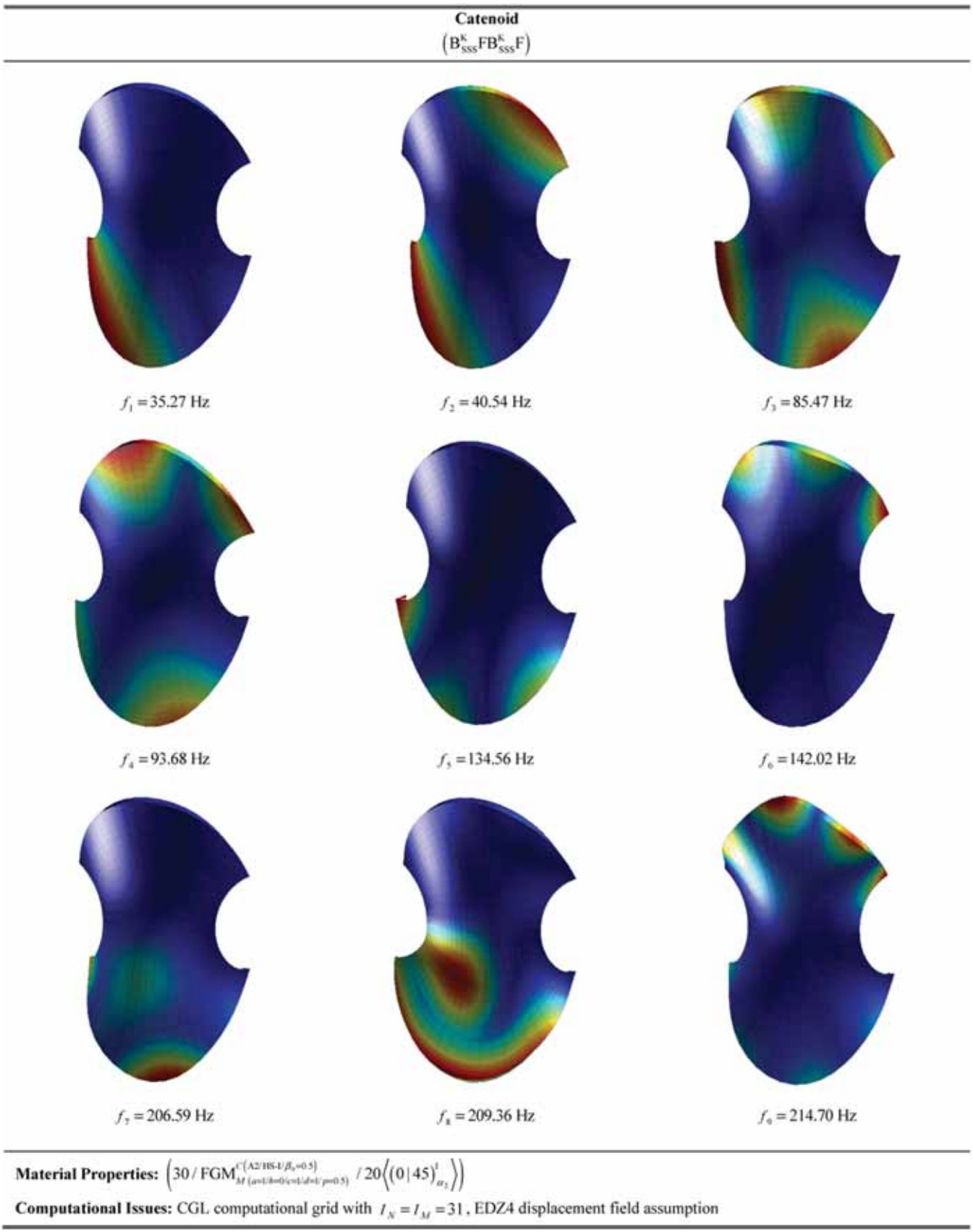


**Fig. 14.** First nine mode shapes of a mapped catenoid made of an external isotropic layer, a central triclinic porous core and an outer orthotropic sheet made of variable angle tow composite. They have been calculated with the EDZ4 higher order theory.

distributions. The same approach has also revealed to be capable of well predicting a series of three-dimensional phenomena with a reduced computational cost.

## CRediT authorship contribution statement

All authors have participated in (a) conception and design, or analysis and interpretation of the data; (b) drafting the article or revising it critically for important intellectual content; and (c) approval of the final version.

## Conflict of interest

This manuscript has not been submitted to, nor is under review at, another journal or other publishing venue.

The authors have no affiliation with any organization with a direct or indirect financial interest in the subject matter discussed in the manuscript.

## Declaration of competing interest

The authors declare that they have no conflict of interest.

## References


[1] Pilato LA, Michno MJ. Advanced Composite Materials. Berlin: Springer Science & Business Media; 1994.
[2] Lipski S, Betiuk M. The integration of a material structure with sensors and effectors-from theory to technology. J Mach Constr Maint-Probl Eksploat 2019;3:39–45.
[3] Sze KY. Three-dimensional continuum finite element models for plate/shell analysis. Prog Struct Eng Mater 2002;4:400–7.
[4] Grigolyuk EI, Kulikov GM. General direction of development of the theory of multilayered shells. Mech Compos Mater 1988;24:231–41.
[5] Ciarlet PG. An introduction to differential geometry with applications to elasticity. J Elast 2005;78:1–215.
[6] Berger M, Gostiaux B. Differential Geometry: Manifolds, Curves, and Surfaces: Manifolds, Curves, and Surfaces. New York: Springer Science & Business Media,; 2012.
[7] Cottrell JA, Reali A, Bazilevs Y, Hughes TJ. Isogeometric analysis of structural vibrations. Comput Methods Appl Mech Eng 2006;195:5257–96.
[8] Piegl L, Tiller W. The NURBS book. Berlin: Springer Science & Business Media; 1996.
[9] Nguyen VP, Anitescu C, Bordas SP, Rabczuk T. Isogeometric analysis: an overview and computer implementation aspects. Math Comput Simul 2015;117:89–116.
[10] Sakiyama T, Huang M. Free vibration analysis of rectangular plates with variable thickness. J Sound Vib 1998;216:379–97.
[11] Wu TY, Liu GR. Free vibration analysis of circular plates with variable thickness by the generalized differential quadrature rule. Int J Solids Struct 2001;38:7967–80.
[12] Levy R, Ganz A. Analysis of optimized plates for buckling. Comput Struct 1991;41:1379–85.
[13] Sokolnikoff IS. Mathematical Theory of Elasticity. 1st ed. New York: McGraw-Hill; 1956.
[14] Ye J, Soldatos KP. Three-dimensional stress analysis of orthotropic and cross-ply laminated hollow cylinders and cylindrical panels. Comput Methods Appl Mech Eng 1994;117:331–51.
[15] Hughes TJ, Liu WK. Nonlinear finite element analysis of shells: Part I. Three-dimensional shells. Comput Methods Appl Mech Eng 1981;26:331–62.
[16] Reddy JN, Robbins Jr DH. Theories and computational models for composite laminates. Appl Mech Rev 1994;47:147–69.
[17] Reddy JN. An evaluation of equivalent-single-layer and layerwise theories of composite laminates. Compos Struct 1993;25:21–35.
[18] Noor AK, Burton WS. Assessment of computational models for multilayered anisotropic plates. Compos Struct 1990;14:233–65.
[19] Liu D, Li X. An overall view of laminate theories based on displacement hypothesis. J Compos Mater 1996;30:1539–61.
[20] Tornabene F, Viscoti M, Dimitri R. Generalized higher order layerwise theory for the dynamic study of anisotropic doubly-curved shells with a mapped geometry. Eng Anal Bound Elem 2022;134:147–83.
[21] Li D. Layerwise theories of laminated composite structures and their applications: a review. Arch Comput Methods Eng 2020:1–24.
[22] Tornabene F., Hygro-Thermo-Magneto-Electro-Elastic Theory of Anisotropic Doubly-Curved Shells, Esculapio, Bologna, 2023.
[23] Kreja I, Sabik A. Equivalent single-layer models in deformation analysis of laminated multilayered plates. Acta Mech 2019;230:2827–51.
[24] Sayyad AS, Ghugal YM. Flexure of cross-ply laminated plates using equivalent single layer trigonometric shear deformation theory. Struct Eng Mech 2014;51:867–91.
[25] Abrate S, Di Sciuva M. Equivalent single layer theories for composite and sandwich structures: A review. Compos Struct 2017;179:482–94.
[26] Hebali H, Tounsi A, Houari MSA, Bessaim A, Bedia EAA. New quasi-3D hyperbolic shear deformation theory for the static and free vibration analysis of functionally graded plates. J Eng Mech 2014;140:374–83.
[27] Gherlone M. On the use of zigzag functions in equivalent single layer theories for laminated composite and sandwich beams: a comparative study and some observations on external weak layers. J Appl Mech 2013;80:061004.
[28] Vidal P, Polit O. A sine finite element using a zig-zag function for the analysis of laminated composite beams. Compos Part B: Eng 2011;42:1671–82.
[29] Basar Y, Ding Y. Interlaminar stress analysis of composites: layer-wise shell finite elements including transverse strains. Compos Eng 1995;5:485–99.
[30] Ramesh SS, Wang CM, Reddy JN, Ang KK. A higher-order plate element for accurate prediction of interlaminar stresses in laminated composite plates. Compos Struct 2009;91:337–57.
[31] Barbero EJ, Reddy J. Modeling of delamination in composite laminates using a layer-wise plate theory. Int J Solids Struct 1991;28:373–88.
[32] Li X, Liu D. Zigzag theory for composite laminates. AIAA J 1995;33:1163–5.
[33] Murakami H. Laminated composite plate theory with improved in-plane responses. ASME J Appl Mech 1986;53:661–6.
[34] Demasi L. Refined multilayered plate elements based on Murakami zig–zag functions. Compos Struct 2005;70:308–16.
[35] Groh RMJ, Weaver PM. On displacement-based and mixed-variational equivalent single layer theories for modelling highly heterogeneous laminated beams. Int J Solids Struct 2015;59:147–70.
[36] Washizu K. Variational Methods in Elasticity and Plasticity. Oxford: Pergamon Press,; 1975.
[37] Reddy JN. A generalization of two-dimensional theories of laminated composite plates. Commun Appl Numer Methods 1987;3:173–80.
[38] Tornabene F, Viscoti M, Dimitri R, Reddy JN. Higher order theories for the vibration study of doubly-curved anisotropic shells with a variable thickness and isogeometric mapped geometry. Compos Struct 2021;267:113829.
[39] Reddy JN, Wang CM. An overview of the relationships between solutions of the classical and shear deformation plate theories. Compos Sci Technol 2000;60:2327–35.
[40] Shahbazi M, Boroomand B, Soghrati S. A mesh-free method using exponential basis functions for laminates modeled by CLPT, FSDT and TSDT–Part I: Formulation. Compos Struct 2011;93:3112–9.
[41] Wang CM, Reddy JN, Lee KH. Shear deformable beams and plates: Relationships with classical solutions. Kidlington: Elsevier,; 2000.
[42] Tornabene F, Viscoti M, Dimitri R. Equivalent single layer higher order theory based on a weak formulation for the dynamic analysis of anisotropic doubly-curved shells with arbitrary geometry and variable thickness. Thin-Walled Struct 2022;174:109119.
[43] Tornabene F, Viscoti M, Dimitri R, Aiello MA. Higher-order modeling of anisogrid composite lattice structures with complex geometries. Eng Struct 2021;244:112686.
[44] Tornabene F, Viscoti M, Dimitri R. Higher Order Formulations for doubly-curved shell structures with a honeycomb core. Thin-Walled Struct 2021;164:107789.
[45] Tornabene F, Reddy JN. FGM and laminated doubly-curved and degenerate shells resting on nonlinear elastic foundations: a GDQ solution for static analysis with a posteriori stress and strain recovery. J Indian Inst Sci 2013;93:635–88.
[46] Naebe M, Shirvanimoghaddam K. Functionally graded materials: A review of fabrication and properties. Appl Mater Today 2016;5:223–45.
[47] Kumar P, Harsha SP. Dynamic analysis of porosity dependent functionally graded sigmoid piezoelectric (FGSP) plate. Structures 2022;46:1737–52.
[48] Dhuria M, Grover N, Goyal K. Influence of porosity distribution on static and buckling responses of porous functionally graded plates. Structures 2021;34:1458–74.
[49] Tornabene F. Free vibration analysis of functionally graded conical, cylindrical shell and annular plate structures with a four-parameter power-law distribution. Comput Methods Appl Mech Eng 2009;198:2911–35.
[50] Kumar V, Singh SJ, Saran VH, Harsha SP. Vibration characteristics of porous FGM plate with variable thickness resting on Pasternak's foundation. Eur J Mech-A/Solids 2021;85:104124.
[51] Njim EK, Bakhy SH, Al-Waily M. Free vibration analysis of imperfect functionally graded sandwich plates: analytical and experimental investigation. Arch Mater Sci Eng 2021;111:49–65.
[52] Rezaiee-Pajand M, Rajabzadeh-Safaei N, Masoodi AR. An efficient curved beam element for thermo-mechanical nonlinear analysis of functionally graded porous beams. Structures 2020;28:1035–49.
[53] Cong PH, Chien TM, Khoa ND, Duc ND. Nonlinear thermomechanical buckling and post-buckling response of porous FGM plates using Reddy's HSDT. Aerosp Sci Technol 2018;77:419–28.
[54] Ramteke PM, et al. Theoretical thermoelastic frequency prediction of multi (uni/bi) directional graded porous panels and experimental verification. Structures 2023;54:618–30.
[55] Karami B, Janghorban M. On the dynamics of porous nanotubes with variable material properties and variable thickness. Int J Eng Sci 2019;136:53–66.
[56] Zhao J, Xie F, Wang A, Shuai C, Tang J, Wang Q. Vibration behavior of the functionally graded porous (FGP) doubly-curved panels and shells of revolution by using a semi-analytical method. Compos Part B: Eng 2019;157:219–38.
[57] Kim J, Żur KK, Reddy JN. Bending, free vibration, and buckling of modified couples stress-based functionally graded porous micro-plates. Compos Struct 2019;209:879–88.

[58] Guan X, Sok K, Wang A, Shuai C, Tang J, Wang Q. A general vibration analysis of functionally graded porous structure elements of revolution with general elastic restraints. Compos Struct 2019;209:277–99.
[59] Lei YL, Gao K, Wang X, Yang J. Dynamic behaviors of single-and multi-span functionally graded porous beams with flexible boundary constraints. Appl Math Model 2020;83:754–76.
[60] Yadav A, Amabili M, Panda SK, Dey T. Nonlinear analysis of cylindrical sandwich shells with porous core and CNT reinforced face-sheets by higher-order thickness and shear deformation theory. Eur J Mech-A/Solids 2021;90:104366.
[61] Zhang C, Liu P, Zhu D, Van Lich L, Bui TQ. Analysis of natural frequency for bioinspired functional gradient plates. Int J Mech Mater Des 2020;16:367–86.
[62] Reddy JN. Exact solutions of moderately thick laminated shells. J Eng Mech 1984; 110:794–809.
[63] Garg A, Belarbi MO, Chalak HD, Chakrabarti A. A review of the analysis of sandwich FGM structures. Compos Struct 2021;258:113427.
[64] Tornabene F.., Generalized Differential and Integral Quadrature, Esculapio, Bologna, 2023.
[65] Shu C, Chen W. On optimal selection of interior points for applying discretized boundary conditions in DQ vibration analysis of beams and plates. J Sound Vib 1999;222:239–57.
[66] Shu C, Chen W, Xue H, Du H. Numerical study of grid distribution effect on accuracy of DQ analysis of beams and plates by error estimation of derivative approximation. Int J Numer Methods Eng 2001;51:159–79.
[67] Shu C, Richards BE. Application of generalized differential quadrature to solve two-dimensional incompressible Navier-Stokes equations. Int J Numer Methods Fluids 1992;15:791–8.
[68] Tornabene F, Viscoti M, Dimitri R. Static analysis of anisotropic doubly-curved shells with arbitrary geometry and variable thickness resting on a Winkler-Pasternak support and subjected to general loads. Eng Anal Bound Elem 2022;140: 618–73.
[69] Tornabene F, Viscoti M, Dimitri R. Higher order theories for the modal analysis of anisotropic doubly-curved shells with a three-dimensional variation of the material properties. Eng Anal Bound Elem 2024;158:486–519.